# Higgs Interference Effects in Gluon-Induced Weak Boson Pair Production at the LHC

Claire O'Brien

Department of Physics
Royal Holloway, University of London

A thesis submitted to the University of London for the
Degree of Doctor of Philosophy

September 6, 2016

# DECLARATION

I confirm that the work presented in this thesis is my own. Where information has been derived from other sources, I confirm that this has been indicated in the document.

Claire O'Brien

## Abstract

This thesis discusses the extension of the parton-level integrator and event generator `gg2VV` to the semi-leptonic decays of the Standard Model Higgs boson and to the leptonic decays of a heavy Higgs boson in the Higgs singlet model, as well as the redesign of the phase space integration in the program to take advantage of the multi-channel method. Interference effects are isolated and studied; such effects in both examples considered are of particular interest because they contain more than one class of interfering backgrounds – tree-level and continuum backgrounds in the semi-leptonic case, and light Higgs and continuum backgrounds in the Higgs singlet case. The investigated effects and developed tools are important for an accurate description of the high-mass signal of the discovered Higgs boson and related constraints as well as searches for additional, heavier Higgs bosons. All developed codes have been made publicly available.

All cross section contributions (i.e signal, background, signal-background interference) are calculated separately. In the Higgs singlet model it is found that it is important to include both types of interference, as they are individually non-negligible but of similar size and opposite sign, so that the total effect of including such contributions is small. For the semi-leptonic processes, one might assume that the tree-level interference, being of lower order, is more important, but in fact the tree-level interference is found to be generally very small, while continuum interference effects can in certain cases alter the signal-only integrated cross section by more than 100%.

Results are also presented for interference effects in the fully leptonic decays of the Standard Model Higgs boson, also calculated with `gg2VV`. Although such results have already been presented in the literature, they are independently calculated here and presented for comparison and validation of the code, and considered to be relevant since they are of interest in discussions of off-shell effects in some of the leading Higgs decay modes at the LHC, and will be included in the latest CERN Yellow Report of the LHC Higgs Cross Section Working Group.

# ACKNOWLEDGEMENTS

I would like to thank my supervisor, Dr Nikolas Kauer, for his help, guidance and support throughout my studies. I would also like to thank all the staff in the Royal Holloway physics department for helping me along the way and cultivating a great environment in which to work.

I am grateful to STFC for my funding, without which I would not have been able to undertake the work in this thesis.

My fellow students have made my time at Royal Holloway a pleasure, and been responsible for many interesting physics conversations and enjoyable evenings - especially Gabriela, Graham, Ian, Joshuha, Russell and Will. Ian, Josh and Michele deserve special mention for useful discussions about experimental aspects of particle physics, and Russell for useful theoretical physics discussions.

I would like to thank my parents, John and Mary, for continual encouragement and support during my education. I would like to dedicate this thesis to them.

Finally, my love and thanks to Chris for all his support, patience and love.

# Contents

# List of Figures

# List of Tables

# Chapter 1

# Introduction

The Standard Model (SM) of particle physics is under intense scrutiny at the Large Hadron Collider (LHC), and it is more necessary than ever to fully understand all effects that could lead to deviations from SM predictions. One part of this process is calculating cross sections to higher orders – for example, the cross section for Higgs production via gluon fusion, which is loop-induced at leading order, meaning that the leading order process is more complex than the many processes that begin at tree-level, is now known to an impressive $\mathrm{N^3LO}$ [1].

Other avenues of progress involve reducing systematic errors such as those on PDFs; for example, the new PDF4LHC15 PDF sets [2] take into account a huge amount of data from the last decades of collider experiments, and combine information from several different well-tested and well-used PDF fits. The current run of the LHC at 13/14 TeV is expected to achieve a total integrated luminosity of about $300\,\mathrm{fb}^{-1}$, which will reduce many statistical uncertainties.

The effect under consideration in this thesis is the interference between signal (sig) and background (bkg) processes. Although often calculated and discussed separately, ‘signal’ and ‘background’ contributions alone are not valid observables. Even if it can be understand probabilistically whether a process with a particular set of kinematic features is more likely to belong to either class of process, the relevant quantity is the total number of events, related to the *combined* signal and background cross sections. The interference term then arises in a cross section calculation when the matrix element squared is calculated by summing all Feynman diagrams connecting the considered initial state to the considered final state, up to a particular order; giving (where $\mathcal{M}$ denotes the matrix element and $\sigma$ the cross section, both described in Chapter 4):

$$\sigma \sim |\mathcal{M}|^2 = \left|\mathcal{M}_{sig} + \mathcal{M}_{bkg}\right|^2 = \left|\mathcal{M}_{sig}\right|^2 + \left|\mathcal{M}_{bkg}\right|^2 + 2\mathrm{Re}(\mathcal{M}^*_{sig}\mathcal{M}_{bkg}) \tag{1.1}$$

and it is the last term which is referred to as interference.

Although such effects were of course not unknown, they were until recent years frequently considered to be unimportant, and if mentioned at all quoted as a source of error. Until the last decade or so, the available cross section calculations of many Higgs processes had errors at the 10% level or higher, due in particular to large scale uncertainties in the hard scattering cross sections. Now, as has already been mentioned, higher-order calculations have been performed, and such errors reduced to the level of a few percent, meaning that once-neglected effects such as interference, which has been shown in some cases to be of order 10% or higher, can dominate. The importance of understanding them better is then clear. In fact, interference effects have recently allowed a constraint on the total Higgs decay width to be calculated [3–6] which is much better than was expected to be obtainable at the LHC.

This thesis is structured as follows: Chapter 2 gives an overview of the Standard Model of particle physics, in particular a discussion of the Higgs mechanism. Chapter 3 describes the phenomenology of hadron colliders, the LHC, and the challenges in searching for the Higgs boson. Chapter 4 discusses cross sections, observables and interference in detail.

Chapter 5 describes the work I carried out to extend the parton-level integrator and event generator, gg2VV [6], to new SM and beyond-SM processes, and the redesign of the phase space integration to take advantage of multi-channel mappings. Chapter 6, based on ref. [7], and Chapter 7, based on ref. [8], then discuss the results I obtained with this code for interference effects in the SM semi-leptonic decays and selected Higgs singlet model leptonic decays.

Chapter 8 describes results for Standard Model fully leptonic decay interference effects and a comparison of PDF and QCD scale choices, calculated with gg2VV for the latest yellow report of the Higgs Cross Section Working Group at the LHC [9]. Finally, conclusions are given in Chapter 9.

# Chapter 2

# The Standard Model

Modern physics is in many ways the study of forces. Gravity, although still perhaps the least understood, was recognised and studied by Newton as far back as 1686. Elements of the electromagnetic force were explained in the late 19th century by Faraday and developed in the early 20th century. The theories of the final two known forces, the so-called 'weak' and 'strong' forces, were developed alongside the many particle physics discoveries derived from cosmic ray experiments and the earliest large scale particle collider experiments in the second half of the twentieth century. One of the early theoretical triumphs of particle physics was the unification of the electromagnetic and weak forces in the electroweak theory of Glashow, Weinberg and Salam [10–12]. Later, the electroweak and strong theories were combined to give what has become known as the Standard Model (SM) of particle physics.

Symmetries play a fundamental role in our understanding of particle physics. In the 1950s and 60s, it seemed as though there were a huge number of seemingly unrelated particles being discovered; this was known as the 'particle zoo'. Gradually a structure emerged – certain groups of particles displayed very similar masses for example. It was realised that group theory could be used as a means of organising the observed particles.

Aside from giving a means of classification, group theory plays an important role in restricting the interactions that are allowed and the limits that can be placed on certain processes. The known fundamental particles can be classified according to their possible interactions by fitting them into representations of particular Lie groups. Even approximate symmetries are helpful, for example in explaining why certain parameters must be constrained to be small when an approximate symmetry is violated.[1] The SM strictly obeys global Poincaré symmetry (symmetry under Lorentz boosts, rotations and space-time translations) and local ('gauge') symmetries $SU(3)_C$, giving rise to the strong force; $SU(2)_L$, the left-handed weak force, and $U(1)_Y$, the weak isospin. The last two combine to give the electroweak force, as will be explained in more detail later.

The Standard Model has been remarkably successful in many ways. So far, no significant deviations have been observed from predictions for collider observables, although in some cases the required precision in measurement is not yet attainable. The last remaining piece of the puzzle, the Higgs boson which was predicted in refs. [13–17], was discovered at CERN in 2012 [18, 19]. However, the theory is far from perfect. The large number of free parameters that can only be fixed by experiment seems inelegant. A truly fundamental understanding of these forces should lead to predictions of many, if not all, of these parameters. It also fails to describe, among other things, dark matter, the matter-antimatter asymmetry in the Universe and neutrino masses. Furthermore, in the absence of new physics at the TeV scale, one would expect the Higgs boson mass to get significant corrections from self-energy loop diagrams, dragging it up to a larger value than is observed. There are many extensions 'beyond the Standard Model' (BSM) that attempt to remedy some or all of these problems, and hopefully the 13/14 TeV runs of the LHC in the coming years will begin to shed light on the way forward.

## 2.1 Particle Content of the Standard Model

The fundamental particles of the Standard Model can be divided into two types. The fermions carry half-integer spin and obey Fermi-Dirac statistics. These particles make up the building blocks of matter. The bosons have integer spin and obey Bose-Einstein statistics, and the spin-1 ('gauge') bosons carry the charges of the symmetries from which they arise and mediate the interactions between fermions.

Fermions are further divided into leptons and quarks. The electron, the first discovered fundamental particle, and its neutrino partner make up the first generation of leptons. Heavier copies of these particles exist: the muon and tauon, with their respec-

---

[1] e.g. custodial SU(2) symmetry ensures a relatively small mass difference between the $Z$ and $W$ bosons.

tive neutrinos make the second and third generations. In a collider environment, the most important property that is useful in performing measurements, apart from mass, is the electric charge, since the bending of a particle's path in a magnetic field is proportional to its charge. The electron, muon and tauon carry a whole unit of negative charge. The neutrinos carry no charge and are practically massless (although the existence of neutrino flavour oscillations means that there must be mass differences and they therefore cannot all be massless); they are therefore very long lived and interact very rarely, and so are difficult to observe in particle detectors. In a particle collider such as the LHC, their presence must usually be inferred from missing momentum and energy.

The quarks come in six flavours, divided into three generations. The 'up-type' quarks of each generation (named up, charm and top, respectively) have electrical charge $+\frac{2}{3}e$ and the 'down-type' quarks (down, strange and bottom) have charge $-\frac{1}{3}e$. The first two generations can nearly always be approximated as massless for the purposes of collider experiments, but the top is the heaviest particle in the Standard Model at around 173 GeV. The heaviness of the top quark means that it has important roles to play in many ways. In processes with quark loops (for example gluon fusion Higgs production), the first two generations of quarks are typically treated as massless without inducing an appreciable effect on the final result, but the top mass is non-negligible. It is also too heavy to hadronise, and decays quickly; although identification of processes containing top quarks is challenging, studies of top processes have been performed at the LHC [20, 21], giving a unique opportunity to explore the perturbative QCD sector. The bottom-quark mass, although smaller at approximately 4.4 GeV, is increasingly recognised as also being important in certain calculations, particularly in BSM processes.

Quarks are triplets of the $SU(3)$ colour symmetry; the three possible states are named red, blue and green. All observed hadrons are found to be 'colour neutral', i.e. contain a red, a green and a blue quark or a colour/anti-colour pair. The idea of colour was first postulated to explain the existence of the $\Delta^{++}$ particle; it is a ground state (L=0, symmetric spatial wave function) resonance with spin-$\frac{3}{2}$ made up of three up quarks. Fermi statistics require that the total wave function be antisymmetric under the interchange of two quarks. The wave function is the product of the spatial, spin and flavour wave functions; the spatial and flavour wave functions are symmetric, as is the only spin configuration that gives a total spin of $\frac{3}{2}$. Either the Pauli exclusion principle must be abandoned or there is more to the story; the solution is the additional property of colour.

The requirement of colour neutrality also explains why quarks are never observed in isolation in nature. Their existence was first inferred from deep inelastic scattering experiments, where scaling behaviour suggested that hadrons had point-like constituents. The term 'hadron' collectively refers to particles made up of either a quark and anti-quark (mesons) or three quarks/anti-quarks (baryons) with an overall integer unit of charge. The property of asymptotic freedom means that the strong potential is very large at large distances but almost negligible at short distances, so that quarks behave like free particles at short distances (high energies). In any collider interaction, it is then the individual quarks that participate, but after the reaction any quarks not confined in a hadron will undergo a process called hadronisation, and instead of an isolated quark, a 'jet' composed of multiple quarks and gluons ('partons') will be observed.

The fermions come in left-handed and right-handed versions (the inclusion of right-handed neutrinos was not part of the original formulation of the Standard Model but is now usually accepted in order to allow for neutrino masses); the right-handed fermions are $SU(2)$ singlets, and the left-handed fermions are $SU(2)$ doublets, since only the left-handed fermions feel the weak force. The five gauge bosons – the massive $W^+, W^-$ and $Z$ and the massless photon $\gamma$ and gluon $g$ – arise as a consequence of the three local symmetries respected by the SM and carry the currents of the symmetries which generate them. This is explained in more detail in the following sections.

There is one final, crucial field that has not yet been mentioned – the Higgs boson. Despite having integer spin it is not a force carrier but rather a consequence of the mechanism required to give the weak vector bosons mass.

## 2.2 The Lagrangian Description

The probability of a particular initial state, such as two colliding particles, evolving to a given final state can be derived from the action,

$$S = \int dt L \tag{2.1}$$

where L is the Lagrangian, the difference of the kinetic and potential energies.

In fact, it will be more useful to consider not the Lagrangian itself, but the Lagrangian density $\mathcal{L}$, related to $L$ by:

$$L = \int d^3x \mathcal{L}. \tag{2.2}$$

From this point forward, Lagrangian should be taken to mean $\mathcal{L}$ in accordance with normal usage in a particle physics context.

The possible interactions of the fields described in the previous section are governed by a Lorentz-symmetric Lagrangian density known as the Standard Model Lagrangian. It is unchanged by the simultaneous application of charge conjugation, parity (mirror reflection) and time reversal to all or any of its fields ('CPT invariant'), and respects the gauge symmetries of $SU(3)_C \otimes SU(2)_L \otimes U(1)_Y$.

The Standard Model is a renormalisable quantum field theory, meaning that its Lagrangian contains at most first order derivatives and terms of dimension no higher than 4. It is known that quantum field theories may contain divergences; this appeared to be an early stumbling block for this formalism until the idea of renormalisation was proposed. The requirement of renormalisability means that all of these divergences can be absorbed into a finite number of parameters using a particular renormalisation scheme. The final result of any calculable quantity must be independent of the scheme used, but parameters (such as couplings and masses) are measured and specified in a particular scheme and predictivity is restored.

Many theorists argue that renormalisability should not be a required condition for a successful theory, once it is accepted that the theory is only valid to a certain energy scale. Any infinities that occur beyond that scale are a result of a lack of understanding of new physics that may exist. A very successful example of this viewpoint is Fermi's predictions for low energy electron-neutrino scattering before the W boson was discovered, where its presence was encapsulated in the Fermi constant $G_F$.

The effective field theory viewpoint also suggested that new physics was required at the electroweak scale to preserve unitarity in longitudinal-$W$ scattering. Without the Higgs boson, the scattering amplitude for this process is proportional to $\frac{s}{M_W^2}$, where $s$ is the centre-of-mass energy squared, and the cross section would grow like $s$ for $s \gg M_W^2$, leading to the total scattering probability becoming larger than one at approximately

1.2 TeV, violating unitarity. Once the Higgs boson is introduced, the electroweak equivalence theorem means that at high energies the amplitude dependence is proportional to

$$-\frac{M_H^2}{v^2}\left(\frac{s}{s-M_H^2}+\frac{t}{t-M_H^2}\right), \tag{2.3}$$

where $v$ is the Higgs field vacuum expectation value and $t$ the momentum transfer squared. Inserting this amplitude into a partial wave expansion, it is found that the optical theorem restricts the real coefficient of the expansion, leading to an upper bound on the Higgs mass of 870 GeV.

Noether's theorem relates global symmetries to the conservation of a particular charge, and can be extended to local symmetries. In the SM, the relevant conserved charges are the colour charge of $SU(3)_C$ which is carried by the quarks and gluons, the third component of weak isospin of $SU(2)_L$, $T_3$, which is carried by the left handed fermions, the four electroweak bosons and the Higgs particle, and weak hyper-charge, Y, of $U(1)_Y$. However, modern particle physics typically deals with energies below the electroweak unification energy (around $10^{16}$ GeV), where the $SU(2)_L \otimes U(1)_Y$ symmetries are broken to $U(1)_{EM}$ and $T_3$ and Y are replaced by the more familiar electromagnetic charge, $Q = T_3 + Y$.

### 2.2.1 Quantum Electrodynamics

The fermions transform under a spinor representation of the Lorentz Group, denoted $\Lambda_{\frac{1}{2}}$, as

$$\psi\left(x\right) \to \Lambda_{\frac{1}{2}}\psi\left(\Lambda^{-1}x\right) \tag{2.4}$$

and the kinetic and mass terms for a free fermion are given by the Dirac Lagrangian:

$$\bar{\psi}\left(i\partial\!\!\!/ - m\right)\psi. \tag{2.5}$$

A global U(1) symmetry, that is, a transformation like $\psi \to e^{i\alpha}\psi$ where $\alpha$ is the same at every space-time point, is trivially respected since $\psi$ only occurs in the combination $\bar{\psi}\psi \to e^{i\alpha}e^{-i\alpha}\bar{\psi}\psi = \bar{\psi}\psi$.[2] However, if the symmetry is gauged, making it such that $\alpha = \alpha(x_\mu)$, then $\psi$ transforms as $\psi \to e^{i\alpha(x)}\psi$. The derivatives in the Lagrangian will

---

[2] $\bar{\psi} = i\gamma^0\psi^\dagger$, rather than simply $\psi^\dagger$, is necessary to keep the combination Lorentz invariant

also act on the transformation parameter $\alpha(x)$ so that

$$\partial_\mu \psi(x) \rightarrow e^{i\alpha(x)} \partial_\mu \psi(x) + i \partial_\mu \alpha(x) \psi(x), \tag{2.6}$$

which obviously will not keep the Lagrangian invariant. This can be remedied by adding a spin-1 field $A_\mu$ that transforms in the adjoint representation as

$$A_\mu \rightarrow A_\mu - \frac{1}{e} \partial_\mu \alpha(x), \tag{2.7}$$

while simultaneously replacing the partial derivative in the Lagrangian with the gauge covariant derivative:

$$\partial_\mu \rightarrow D_\mu \equiv \partial_\mu + ieA_\mu(x), \tag{2.8}$$

which will transform like the field itself. The gauge invariance of the Lagrangian is restored, and a new field has been introduced which interacts with the original field $\psi$ with a strength proportional to $e$.

The kinetic term for the vector field takes the form $-\frac{1}{4}F_{\mu\nu}F^{\mu\nu}$ where

$$F_{\mu\nu} = \partial_\mu A_\nu - \partial_\nu A_\mu. \tag{2.9}$$

The interaction term between the fermion field and vector field arises naturally through the kinetic term from the modification of the partial derivative and respects renormalisability and the local U(1) symmetry. However, if one further tries to add a mass for the new field with a term of the form $m^2 A^\mu A_\mu$, the U(1) symmetry is broken explicitly. For now, it is sufficient to simply forbid terms of this form and leave the field massless: this allows the identification of the Lagrangian composed of the components given above as that of quantum electrodynamics (QED):

$$\begin{aligned} \mathcal{L}_{QED} &= -\frac{1}{4}F_{\mu\nu}F^{\mu\nu} + \bar{\psi}\left(i\not{D} - m\right)\psi \\ &= -\frac{1}{4}F_{\mu\nu}F^{\mu\nu} + \bar{\psi}\left(i\not{\partial} - m\right)\psi - e\bar{\psi}\gamma^\mu\psi A_\mu. \end{aligned} \tag{2.10}$$

The spin-1 field is identified with a massless photon, just as is observed. Note that in order to perform calculations, a gauge-fixing term must be added to remove ambiguity in the propagator, which is derived from the inverse of the quadratic terms.

As a general prescription, this formalism will become problematic when considering other gauge symmetries, where it is found that the prediction of massless gauge bosons contradicts experimental observations.

### 2.2.2 The Electroweak Sector

The previous section showed an example of enforcing a simple gauge symmetry on the Lagrangian. In reality, a more careful treatment is required for several reasons. The SM is a chiral theory: the spinor representation can be split into its left-handed and right-handed components: $\psi = \psi_L + \psi_R$ where each component can be projected out by using the left- and right-handed projection operators, $P_{\substack{L \\ R}} = \frac{1}{2}\left(1 \mp \gamma_5\right)$. The full symmetry group includes $SU(2)_L$, which acts only on the left-handed components, meaning that the simple fermion mass term given above cannot be used, as this mixes left- and right-handed components. It will be seen that the Higgs mechanism allows a mass term to arise for SM fermions in a different way.

The effect of the $U\left(1\right)$ symmetry in the previous section was relatively simple to study in that the group has a single generator and therefore a single possible transformation. However, the vector bosons always lie in the adjoint representation of the gauge group, which for $SU(N)$ has $N^2 - 1$ generators; here there are three generators and hence three vector bosons. Furthermore, $SU(2)$ is a non-abelian group,[3] meaning that its generators do not commute. This allows self interactions of the gauge bosons.

The combined $SU\left(2\right)_L \times U\left(1\right)_Y$ transformations acting on the (left-handed) fermion fields give:

$$\psi \to e^{i(g\boldsymbol{\tau}\cdot\omega(x) + g'Y\beta(x))}\psi. \tag{2.11}$$

and the covariant derivative is now extended to (replacing the QED coupling constant $e$ with $g'$, and the field $A_\mu$ with $B_\mu$ so that the physical theory will arrive at the usual notation)

$$D_\mu = \partial_\mu + ig'YB_\mu + ig\tau_a W^a_\mu \tag{2.12}$$

where $a = 1 \ldots 3$. Note that only the first two terms will apply to the covariant derivative

---

[3] This is true for all SU(N), N> 1.

for right-handed fermions.

Y denotes the weak hyper-charge quantum number, and the 2-dimensional generator matrices of the adjoint representation of $SU(2)$ are given by

$$\tau_a = \frac{1}{2}\sigma_a \tag{2.13}$$

where $\sigma_a$ denote the Pauli matrices. Expanding the covariant derivative makes the field content clearer: the multiplication of the Pauli matrices with the three W components leads to

$$\begin{aligned} \tau_a W^a_\mu &= \frac{1}{2}\begin{pmatrix} W^3_\mu & W^1_\mu - iW^2_\mu \\ W^1_\mu + iW^2_\mu & -W^3_\mu \end{pmatrix} \\ &= \frac{1}{2}\begin{pmatrix} W^3_\mu & \sqrt{2}W^+_\mu \\ \sqrt{2}W^-_\mu & -W^3_\mu \end{pmatrix}, \end{aligned} \tag{2.14}$$

where the linear combinations $W^\pm_\mu = \frac{1}{\sqrt{2}}\left(W^1_\mu \mp W^2_\mu\right)$ have been used. The full covariant derivative is then

$$D_\mu = \begin{pmatrix} \partial_\mu + i\frac{g}{2}W^3_\mu + ig'B_\mu & \frac{i}{\sqrt{2}}gW^+_\mu \\ \frac{i}{\sqrt{2}}gW^-_\mu & \partial_\mu - i\frac{g}{2}W^3_\mu + ig'YB_\mu \end{pmatrix} \tag{2.15}$$

There is a linear combination of fields in the diagonal terms; the system can then be diagonalised, taking:

$$\begin{aligned} A_\mu &= \sin\theta_w W^3_\mu + \cos\theta_w B_\mu \\ Z_\mu &= \cos\theta_w W^3_\mu - \sin\theta_w B_\mu \end{aligned} \tag{2.16}$$

where $\tan\theta_w = \frac{g'}{g}$. Taking $Q = T_3 + Y$, where $T_3$ is the eigenvalue of $\frac{\tau_3}{2}$, gives:

$$D_\mu = \partial_\mu + \begin{pmatrix} ieQA_\mu + i\left(\frac{e}{\sin 2\theta_w} - \frac{eQ\sin\theta_w}{cos\theta_w}\right)Z_\mu & \frac{ig}{\sqrt{2}}W^+_\mu \\ \frac{ig}{\sqrt{2}}W^-_\mu & ieQA_\mu - i\left(\frac{e}{\sin 2\theta_w} + \frac{eQ\sin\theta_w}{cos\theta_w}\right)Z_\mu \end{pmatrix} \tag{2.17}$$

Assuming that $A_\mu$ will be the photon, its coupling has been identified with the electromagnetic coupling:

$$\frac{gg^{'}}{\sqrt{g^{2}+g^{'2}}}=e.$$

It will become clear during the discussion of the Higgs mechanism that this is the correct choice because $A$ will remain massless when the $Z, W^{+}$ and $W^{-}$ particles gain their masses, in agreement with observation.

There are also kinetic terms for the gauge bosons (the fundamental bosons rather than the linear combinations that have been chosen). They are more complicated than those of QED because of the non-abelian nature of SU(2). For the three W bosons,

$$F^{a}_{\mu\nu}=\partial_{\mu}W^{a}_{\nu}-\partial_{\nu}W^{a}_{\mu}+g\epsilon^{abc}W^{b}_{\mu}W^{c}_{\nu} \tag{2.18}$$

where $\epsilon^{abc}$ are the structure constants for the adjoint representation of $SU(2)$. Interaction terms with the fermions arise naturally from the action of the full covariant derivative on their kinetic terms, but an explicit mass term is still forbidden for all four bosons if the $SU(2)_{L}\otimes U(1)_{Y}$ symmetry is to be preserved.

With this grounding, predictions could be attempted for some scattering processes, in the belief that the underlying interactions are well understood. At this stage, some predictions will work very well, for processes involving only leptons and photons (i.e. the QED sector). However, on attempting to include the $SU(2)$ interactions in predictions, theory and experiment immediately diverge: the $SU(2)$ interactions are shown to be short-range, implying that the vector bosons of this interaction have a finite mass. The solution comes from spontaneous symmetry breaking.

### 2.2.3 The Higgs Mechanism

The mechanism by which the electroweak bosons and the fermions are allowed to gain a mass was postulated in 1964 [13–17] , and its crucial prediction, the existence of a neutral, spin-0, CP-even particle, confirmed in 2012 [18, 19]. It remains to be confirmed if the minimal mechanism proposed by Higgs, Kibble, Hagen, Guralnik, Brout and Englert to complete the SM is the full story or if a more elaborate extension is realised, but hopefully the next decade of particle physics experiments at CERN will be able to bring us closer to answering this question.

The crucial idea of the mechanism is that while the Lagrangian respects the full symmetry, the ground state does not; effectively, the vacuum expectation value (VEV) of the Higgs field is non-zero. This is known as spontaneous symmetry breaking (SSB), but this term may be a little misleading; the symmetry is still present in the Lagrangian, although hidden in the physical ground state which is observed.

Symmetry breaking had been considered in other particle physics contexts, for example in explaining the low and similar masses of the pions, but Goldstone's Theorem states that when a continuous symmetry is broken, massless (or nearly massless if the symmetry is approximate) bosons must be present for each broken generator. No such particles were observed, suggesting that this mechanism would not be useful here. Furthermore, because the theory under consideration is local (other known examples were all of global symmetry breaking), their presence would imply oscillations in the basin of the potential, equivalent to changing gauge, and hence they cannot be physical.

The contribution of Higgs and others showed that in the case where the broken symmetry is local and the model already contains particles with the same quantum numbers as the would-be Goldstone bosons, the degrees of freedom of the Goldstone bosons can be absorbed by the existing bosons in the model. In the case of the Standard Model, this gives the extra degree of freedom necessary for massless bosons, with two transverse polarisations, to become massive by adding the longitudinal polarisation. Depending on the gauge that is chosen, the presence of the Goldstone boson degrees of freedom can be made explicit or hidden.

The Higgs field is a complex scalar doublet, with weak isospin $T = \frac{1}{2}$ and hypercharge $Y = \frac{1}{2}$:

$$\phi = \begin{pmatrix} \phi^+ \\ \phi^0 \end{pmatrix} = \begin{pmatrix} \phi_1 + i\phi_2 \\ \phi_3 + i\phi_4 \end{pmatrix} \tag{2.19}$$

where the + and 0 denote the positive and neutrally charged components with respect to the electromagnetic charge $Q = T_3 + Y$. The postulated Higgs potential is (again, the form is dictated by the requirements of symmetry and renormalisability):

$$V_{Higgs} = \lambda \left(\phi^\dagger \phi\right)^2 - \mu^2 \phi^\dagger \phi \tag{2.20}$$

Note the negative sign of the mass-like term, meaning that the minimum of the potential is reached for a non-zero value of $\phi$ – this is equivalent to saying that $\phi$ has a non-zero vacuum expectation value. The VEV is assigned to the neutral component; this choice ensures that one linear combination of generators will still annihilate the vacuum, which means that one particle (the photon) will remain massless. This choice is the point at the which the symmetry becomes broken, since choosing one of a degenerate set of possibilities means that the potential no longer looks symmetric from the viewpoint of this minimum. Note that switching between different choices of VEVs is equivalent to transforming between gauges.

Expanding about the VEV, for now in the unitary gauge (in a different parametrisation to make the gauge transformation clearer), gives:

$$\begin{aligned}\Phi &= \frac{1}{\sqrt{2}} e^{\frac{i\boldsymbol{\tau}\cdot\omega}{v}} \begin{pmatrix} 0 \\ v + H(x) \end{pmatrix} \\ &\simeq \frac{1}{\sqrt{2}} \begin{pmatrix} -\omega_2(x) - i\omega_1(x) \\ v + H(x) + i\omega_3(x) \end{pmatrix}\end{aligned} \tag{2.21}$$

(to first order in the fields $\omega_i$ and $H$) where H is used to denote the degree of freedom that represents the physical scalar particle that will be recognised as the Higgs boson.

Using the freedom of SU(2) rotations to hide the Goldstone bosons (i.e. a transformation by $\phi \to U\phi$ where $U = e^{-\frac{i\boldsymbol{\tau}\cdot\omega}{v}}$) in the expression for $\Phi$ leaves

$$\Phi = \frac{1}{\sqrt{2}} \begin{pmatrix} 0 \\ v + H(x) \end{pmatrix} \tag{2.22}$$

but note that the gauge transformation also affects the W bosons, giving the transformation:

$$W_i \to W_i^{phys} = W_i - \frac{1}{gv}\partial_\mu \omega_i \tag{2.23}$$

reflecting the addition of a new degree of freedom; it is said that the vector bosons have 'eaten' the Goldstone bosons. From now on, $W$ will be taken to mean $W^{phys}$.

The kinetic term for a scalar field looks like $\left|D_\mu \Phi\right|^2$ where D is the covariant derivative. Inserting (2.15) and (2.21) then gives (neglecting constant terms)

$$\begin{aligned} D_\mu \Phi &= \frac{1}{\sqrt{2}} \left( \partial_\mu + i\frac{g}{2}\sigma_a W_\mu^a + i\frac{g^{'}}{2} B_\mu \right) \Phi \\ &= \partial_\mu H + \begin{pmatrix} i\frac{g}{2} W_\mu^+ \left( v + H \right) \\ i\frac{1}{\sqrt{2}} \left( \frac{e}{\sin 2\theta_w} Z_\mu \right) \left( v + H \right) \end{pmatrix}, \end{aligned} \tag{2.24}$$

leading to

$$\begin{aligned} \left| D_\mu \Phi \right|^2 = \partial_\mu H \partial^\mu H &+ \frac{g^2 v^2}{4} W_\mu^+ W^{-\mu} + \frac{v^2 \left( g^2 + g'^2 \right)}{8} Z_\mu Z^\mu + \frac{v g^2}{2} W_\mu^+ W^{-\mu} H \\ &+ \frac{v \left( g^2 + g'^2 \right)}{4} Z_\mu Z^\mu H \end{aligned} \tag{2.25}$$

This leads to a picture that agrees with experiment - two bosons with equal mass $\frac{gv}{2}$ and opposite charge ($W^{\pm}$), and another neutral massive boson ($Z$) that has a mass of $\frac{\sqrt{g^2+g'^2}v}{2}$. The contributions containing $A_\mu$ disappear from the symmetry breaking terms since the symmetry breaking component has $Q = 0$, leaving one massless, neutral boson.

Using experimental values for $M_Z$ and $e$ gives a value for $v$ of approximately 246 GeV. Substituting eq. (2.22) into eq. (2.20) gives quadratic, cubic and quartic terms for the new $H$ field, giving rise to cubic and quartic self-interactions and a mass of

$$M_H = \sqrt{2\lambda} v. \tag{2.26}$$

The Higgs mass is taken to be another free parameter, and sets the Higgs coupling $\lambda$.

Renormalisation means that couplings become ‘running’ couplings that depend on the energy scale. Extrapolating $g$ and $g'$ gives a meeting point of $O(10^{16})$ GeV, and this can then be assumed to be the symmetry breaking scale, the centre-of-mass energy at which the symmetry becomes hidden and instead of $SU(2)_L \times U(1)_Y$, only $U(1)_{EM}$ is observed. This means that below energies of $O(10^{16})$ GeV instead of two distinct couplings, $g$ and $g'$, only the coupling constant of the $U(1)_{EM}$ symmetry is present, the familiar electric charge $e$.

The inclusion of the new Higgs field also allows for new terms giving the leptons and quark masses and allowing interactions with the Higgs, known collectively as Yukawa terms. The term for leptons is:

$$-\frac{1}{\sqrt{2}}\lambda_e \bar{e}_L \, \Phi \, e_R + \text{h.c.} \tag{2.27}$$

where the left handed leptons are in a doublet representation of $SU(2)$ with $Y = \frac{1}{2}$ and the right-handed electron is a singlet with $Y = -1$, meaning that the term is neutral with respect to both $SU(2)_L$ and $U(1)_Y$. This leads to an electron mass term with a mass of $\frac{\lambda_e v}{\sqrt{2}}$ and also an interaction term between the Higgs and two electrons. The electron Yukawa coupling is a free parameter to be set by experiment.

The form of these terms provides a crucial way to test the predictions of the mechanism experimentally - there is a clear dependence of the couplings of the Higgs to the fermions on the mass of the relevant fermion, which should be measurable in the rates of Higgs decays (for the heavier fermions). These may not be accessible at the LHC, at least not soon, but future Higgs factories will hopefully remedy this.

Unitarity and triviality [4] limits suggest that the mass of the Higgs should be less than 1 TeV; the discovered resonance at 125 GeV, close to the electroweak scale, certainly fits the brief, but its relative smallness creates other problems. Because the Higgs is a scalar, it is subject to large mass corrections from integrals over momenta in loop diagrams. Either there is some protection against this that is not yet understood – for example a symmetry that would be violated by such corrections, or that would include other particles whose Feynman diagrams cancel the problematic diagrams (this is a

---

[4] The triviality limits arise from the running of the Higgs coupling, $\lambda$, related to the Higgs mass by eq. (2.26). At lowest order, this is given by

$$\lambda(Q) = \frac{\lambda(Q_0)}{1 - \frac{3\lambda(Q_0)}{4\pi^2}\log\left(\frac{Q^2}{Q_0^2}\right)}, \tag{2.28}$$

with the reference scale usually taken to be $v$ in the SM. As $Q \to \infty$, the denominator can go to 0, so that $\lambda(Q)$ becomes infinite and the theory is non-perturbative unless $\lambda = 0$, i.e. the theory is trivial. An upper limit on the Higgs mass is then obtained by requiring that the coupling remain finite up to some scale of new physics, $\Lambda$, typically a few TeV, which gives

$$M_H^2 < \frac{8\pi^2 v^2}{3\log\left(\frac{\Lambda^2}{v^2}\right)}.$$

A lower limit is also obtained from the running of $\lambda$ in conjunction with the requirement of vacuum stability, i.e. the requirement that $V(v) < V(0)$ (V from eq. (2.20)) is a local minimum, even with the inclusion of one and two-loop corrections to the running coupling. This requires that $\lambda(\Lambda) > 0$.

large reason why supersymmetry is considered so attractive), or there is an unexplained cancellation (to at least 15 digits) between terms, known as fine-tuning. Many people find this very aesthetically unpleasant, but others argue that it should not be considered an issue if it is accepted that the Standard Model is only an effective theory.

### 2.2.4 The Colour Sector

The final sector of the Standard Model describes particles that feel the so-called 'strong' force, and are symmetric under $SU(3)_C$. These are the fractionally charged quarks and their boson, the gluon. The gluon is massless with spin 1.

The covariant derivative required for the kinetic terms of the quarks is

$$D_\mu = \partial_\mu + ig' T_a W_\mu^a + igYB_\mu + ig_s \frac{\lambda_a}{2} G_\mu^a \tag{2.29}$$

The new field, $G_\mu$ is in the adjoint representation of $SU(3)$ and therefore has eight generators. The kinetic term takes the same form as eq. (2.18). The generator matrices, $\lambda_a$, are known as the Gell-Mann matrices.

As with the leptons, the left-handed quarks fit into electroweak doublets and the right-handed into singlets and there are three generations, with increasing masses.

The theory that describes the colour sector is known as Quantum Chromodynamics (QCD). QCD is the most challenging part of the Standard Model to study, owing to the fact that the coupling constant of the colour sector, $g_s$, becomes non-perturbative at low energies. However the underlying, parton-level process can be predicted well in the range that the LHC looks at. The next chapter will discuss hadron collider phenomenology in more detail, but here it is relevant to simply note that the success to-date shows how successful modern methods have become at being able to extract reliable predictions from previous experiments and Monte Carlo modelling.

The quark masses are generated in the same way as the lepton masses, as are their interactions with the Higgs. The Yukawa terms are:

$$\lambda_{di} \bar{Q}_L \, \Phi \, d_R + \lambda_{ui} \bar{Q}_L \, \tilde{\Phi} \, u_R + \text{h.c.}. \tag{2.30}$$

Each term is neutral with respect to weak hyper-charge and $SU(2)_L$. Note that the conjugate Higgs doublet has been introduced,

$$\tilde{\Phi} = i\sigma_2\Phi^* = \begin{pmatrix} \phi^{0*} \\ -\phi^{+*} \end{pmatrix}$$

with electroweak quantum numbers $T = \frac{1}{2}$ and $Y = -\frac{1}{2}$.

Since the quarks also carry weak quantum numbers, they interact with the W and Z bosons. Naively, it might be expected that only members of the same quark generation can interact – this makes sense if the covariant derivative acts on each $Q_{Li}$ doublet for each individual generation number i. This is in fact not the case; interactions are observed between e.g. up and strange quarks where one might expect only up and down quarks to interact. The quark states which are observed are mass eigenstates which are superpositions of the flavour eigenstates, related by the CKM matrix, i.e.

$$Q_{L_i m} = V^{\dagger}_{CKM} Q_{L_i f} V_{CKM}. \tag{2.31}$$

In the limit of $V_{CKM} = 1$ the mass and flavour eigenstates are equal. In reality the non-diagonal elements have been measured to be small but non-zero (see 2.32), allowing interactions between generations i and j to take place with a small probability $\propto V^2_{CKM_{ij}}$.

$$|V_{CKM}| = \begin{pmatrix} v_{ud} & v_{us} & v_{ub} \\ v_{cd} & v_{cs} & v_{cb} \\ v_{td} & v_{ts} & v_{tb} \end{pmatrix} \simeq \begin{pmatrix} 0.97427 & 0.22536 & 0.00355 \\ 0.22522 & 0.97343 & 0.0414 \\ 0.00886 & 0.0405 & 0.99914 \end{pmatrix} \tag{2.32}$$

At tree level, this applies only to the interactions between up-type and down-type quarks, i.e. those that proceed via the charged weak current interaction (via W bosons). The ‘flavour changing neutral current’ (FCNC) interactions are loop-induced and accounted for by diagrams such as those in figure 2.1 - again, in the limit of $V_{CKM} = 1$ such processes are forbidden. A current area of interest in SM precision tests is whether these diagrams entirely account for any FCNC effects observed, or whether there could be more to the story.

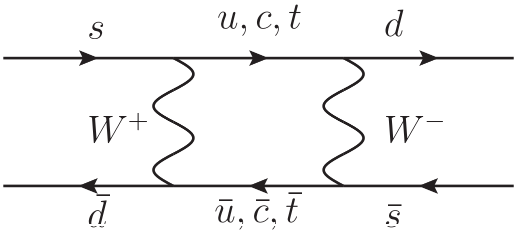

Figure 2.1: Example of flavour-changing neutral current process.

## 2.3 The Standard Model Lagrangian

In summary, the electroweak, strong and Higgs sectors are represented by a Poincaré invariant, renormalisable Lagrangian that respects the local symmetries $SU(3)_C \otimes SU(2)_L \otimes U(1)_Y$. The full Lagrangian, before spontaneous symmetry breaking, is given by:

$$\begin{aligned}\mathcal{L}_{SM} = &-\frac{1}{4}F^a_{\mu\nu}F^{\mu\nu}_a - \frac{1}{4}G^a_{\mu\nu}G^{\mu\nu}_a - \frac{1}{4}B_{\mu\nu}B^{\mu\nu} \\ &+ \left|D_\mu\phi\right|^2 + \lambda\left(\phi^\dagger\phi\right)^2 - \mu^2\phi^\dagger\phi \\ &+ i\bar{L}_i \not{D}_\mu L_i - \frac{1}{\sqrt{2}}\lambda_{Li}\bar{L}_{Li}\,\Phi\,L_{Ri} + h.c. \\ &+ i\bar{Q}_i \not{D}_\mu Q_i + \lambda_{di}\bar{Q}_L\,\Phi\,d_R + \lambda_{ui}\bar{Q}_L\,\tilde{\Phi}\,u_R + \text{h.c.}. \\ &+ \mathcal{L}_{gauge-fixing}\end{aligned} \tag{2.33}$$

with the field strengths defined by

$$\begin{aligned}F^a_{\mu\nu} &= \partial_\mu W^a_\nu - \partial_\nu W^a_\mu + g\epsilon^{abc}W^b_\mu W^c_\nu \\ G^a_{\mu\nu} &= \partial_\mu G^a_\nu - \partial_\nu G^a_\mu + g_s f^{abc}G^b_\mu G^c_\nu \\ B_{\mu\nu} &= \partial_\mu B_\nu - \partial_\nu B_\mu\end{aligned} \tag{2.34}$$

and the covariant derivatives act as:

$$D_\mu L = (\partial_\mu + ig\tau_a W^a_\mu + ig'YB_\mu)L \tag{2.35}$$

for left-handed leptons,

$$D_\mu Q = (\partial_\mu + ig\tau_a W^a_\mu + ig'YB_\mu + ig_s\frac{\lambda_a}{2}G^a_\mu)Q \tag{2.36}$$

for left-handed quarks, and the above without the $ig\tau_a W_\mu^a$ term for the right-handed counterparts.

As mentioned in section 2.2.2 an overall gauge fixing term must be added in order to define the photon propagator. This has the form

$$\mathcal{L}_{gauge-fixing} = -\frac{1}{2}\frac{(\partial_\mu A^\mu)^2}{\xi}. \tag{2.37}$$

A commonly used gauge is the $\xi = 1$ Feynman gauge, which is easy for performing tree-level calculations but leads to unphysical ‘ghost’ particles in loops.

The discovery of the Higgs has completed the SM, although extensions may yet be realised in the form of new symmetries or degrees of freedom. Indeed, it is hoped that the LHC will give hints of some new effects that may help to solve some or all of the current limitations of the model.

# Chapter 3

# Higgs Phenomenology at the Large Hadron Collider

## 3.1 Hadronic Collisions

The collision of two hard (high momentum) partons and production of intermediate resonances and final state partons or leptons is called the hard process, and this is generally well understood, as it occurs in an energy regime where QCD is perturbative and the Feynman rules are applicable. The principles discussed in Chapter 2 then allow reliable predictions to be made for hard process cross sections. However, it is important to remember that the hard process is only an intermediate stage – it is this fact that makes a hadron collider such a challenging environment for discoveries.

In a typical collision, the hard process happens at high centre-of-mass energies where partons (quarks and gluons) are effectively free, so that individual partons, rather than a hadron, form the initial and final states. Each colliding parton carries some fraction $x_i$ of the total available centre-of-mass energy, $\sqrt{s}$.[1] Given two colliding protons, it must then be possible to predict the probability of a particular parton with a particular value of $x_i$ taking part in a collision. This information is encoded in parton distribution functions (PDFs), which must be determined from experimental data.

Two important facts allow reliable predications to be made for the cross sections of

---

[1] The individual beam energy is up to 7 TeV for each beam at the LHC, giving a total centre-of-mass energy of 14 TeV.

hadronic processes. Firstly, the factorisation theorem [22] means that the PDF accounts for all emissions and effects at energy scales below some sensibly chosen factorisation scale $\mu_f$, and above this the hard process calculation will be valid. The important point is that these can be combined in a consistent way which includes all contributions appropriately, and ideally has a low dependence on the choice of $\mu_f$, although at leading order this may not be the case.

Secondly, PDFs are, to an excellent approximation, universal for a particular hadron – they have no dependence on the particular hard process which they are used to initialise. They can then be extracted from well-measured, simpler processes, e.g. in electron-proton collisions at HERA, and applied to more complicated processes, such as proton-proton collisions at the LHC.

At the other end of the collision, after the hard process, a certain number of final state partons will have been produced; the probability for producing this particular final state is fixed, but there is still more work required to predict what will be seen in the detector. In the same way that final state leptons would undergo electromagnetic showering, there is a finite probability for emitting more coloured particles; a final state quark may emit a gluon, and a gluon may split into a quark or gluon pair.[2] Formally this is still a perturbative process, and these real emissions come under the remit of higher order corrections, but they cannot be neglected even at leading order because certain regions of the phase space give enhanced contributions at all orders, and without their inclusion the perturbative series will not converge well. Fortunately, there is a well-understood procedure to include these contributions. This part of the process is known as parton showering, and is summarised in section 3.1.3.

Once the energy has reduced to a point where further splittings are unlikely, partons undergo a non-perturbative[3] process known as hadronisation, where free partons combine with vacuum quark pairs. This preserves the requirement that any final states are colour neutral, in practice meaning that collimated jets of hadrons are observed instead of isolated final state partons.

The work in this thesis focuses on the hard processes, with no further discussion

---

[2] This is due to the non-abelian nature of SU(3); the gluon carries colour charge so can split into a gluon pair, unlike photons in the electromagnetic shower.

[3] The strong coupling constant becomes large (non-perturbative) at approximately 2 GeV.

after this chapter of PDFs or showering. The Les Houches format [23] for simulated Monte Carlo events adopted by most modern particle physics groups in their software allows compatibility between calculations of different stages of the process. This allows different groups to focus on different parts of the calculation and combine them in a modular and consistent way. However, since the work done here needs to be considered in the full context of a hadronic collision in order to provide useful predictions for the LHC, a brief summary of the challenges and tools available for different parts of the calculation at the LHC follows.

### 3.1.1 Parton Branching

The formalism used to describe the probability of a coloured particle splitting into two others can be applied both to initial state branching, which is included in the PDF, and to final state branching in the parton shower. The equations governing the evolution of an initial state, specified as a function of the energy scale $Q^2$, are very similar for the two cases, although for the initial state the splitting functions must also be averaged over the azimuthal angle, since this is not measurable.

The two types of branching that yield important enhancements in the emission probability are for a very soft gluon emitted from a quark/anti-quark, and for a gluon splitting into two nearly collinear partons. A full treatment of parton branching is given in [24], the results are quoted here. The splitting kernels, also known as the Altarelli-Parisi splitting functions, form the basis of the evolution equations used in both the PDF (section 3.1.2) and parton shower (section 3.1.3). They are the first terms in a perturbative expansion in $\alpha_s$. The notation convention is that $P_{ab}$ describes parton $b$ splitting into $a$ and $z = E_b/E_a$. The relevant kernels are then:

$$P_{gg}(z) = 6\left(\frac{1-z}{z} + \frac{z}{(1-z)_+} + z\,(1-z) + \left(\frac{11}{12} - \frac{n_f}{18}\right)\delta(1-z)\right), \tag{3.1}$$

$$P_{qg}(z) = \frac{1}{2}\left(z^2 + (1-z)^2\right), \tag{3.2}$$

$$P_{gq}(z) = \frac{4}{3}\left(\frac{1+(1-z)^2}{z}\right) \tag{3.3}$$

and

$$P_{qq}(z) = \frac{4}{3}\left(\frac{1+z^2}{(1-z)_+} + \frac{3}{2}\delta(1-z)\right), \tag{3.4}$$

where $n_f$ is the number of quark flavours and the + subscript denotes

$$\frac{1}{(1-z)_+} = \frac{1}{1-z} \qquad \text{for } \ 0 \leq z \leq 1 \tag{3.5}$$

and

$$\int_0^1 dz\, \frac{f(z)}{(1-z)_+} = \int_0^1 dz\, \frac{f(z)-f(1)}{1-z}. \tag{3.6}$$

### 3.1.2 Parton Distribution Functions

The quantities of interest for the probability of a particular initial state being produced are the functions $f_{h\to a}(x,\mu_f^2)$, for a parton of type $a$ in a particular hadron $h$. These functions describe the probability distribution of the parton's momentum as a fraction $x$ of the momentum of the hadron, including all parton emissions with transverse momentum less than the factorisation scale $\mu_f$. There are thirteen separate PDFs, one for every quark and anti-quark and one for the gluon, for each hadron type. Note that the probability of seeing a top or anti-top from an initial state hadron is negligible, and generally published PDF data is for either a 4- or 5-flavour scheme, with the 5-flavour scheme including the $b$ and $\bar{b}$ distributions. For a practical (Monte Carlo) calculation of the cross section, such as will be discussed in Chapter 4, the full details of the evolution from hadron to parton are not required, only the probability for a particular initial state parton to be produced with momentum fraction $x$ for the chosen value of $\mu_f$.

The double differential cross section $\frac{d^2\sigma}{dQ^2dx}$, describing the probability of an event occurring with particular values of virtuality $Q^2$ and momentum fraction $x$, can be parametrised in terms of structure functions $F_i(x,Q^2)$. These functions can be measured experimentally, for example the structure functions for the proton are measured in deep inelastic scattering (DIS) experiments.[4] The naive parton model initially proposed by Feynman predicts 'Bjorken scaling': as Q → ∞ with $x$ fixed, $F_i(x,Q^2) \simeq F_i(x)$, and this behaviour is indeed observed, although the scaling is not exact. However, the breaking

---

[4] A charged lepton (neutrino) scatters against a proton, with a $t$-channel photon ($W$ boson) acting as a probe.

of Bjorken scaling is predicted by QCD corrections to the basic parametrisation due to hard gluon emissions and the measured effect is in excellent agreement with predictions.

The individual structure functions can then be related to the parton distribution functions $f_i(x, Q^2)$, where $i$ denotes the parton flavour, by

$$F_i(x, Q^2) = \sum_a \int_x^1 \frac{dz}{z} C_i^a f_a \left(\frac{x}{z}, Q^2\right), \tag{3.7}$$

where $C_i$ are coefficients in a perturbation series, defined for a particular factorisation scheme (which then must be used consistently in the rest of the cross section calculation).

The $Q^2$ dependence of the parton distribution is then known from the DGLAP renormalisation group equations [25–27], here using the notation $t = Q^2$:

$$t\frac{\partial}{\partial t} f_i(x, t) = \frac{\alpha_s(t)}{2\pi} \sum_j \int_x^1 \frac{dz}{z} P_{ij}(z)\, f_j \left(\frac{x}{z}, t\right) \tag{3.8}$$

where $P_{ij}(z)$ is a perturbative expansion, with the first order term given by the splitting kernels of eqs. (3.1) to (3.4). This then means that if a particular structure function can be measured over as broad a range of $x$ as possible for any value of $Q^2$, its value at any other $Q^2$ (in particular $\mu_f^2$, the chosen factorisation scale) can be derived. In practice, the region of very small $x$, of large importance for the gluon fusion Higgs production channel, is very difficult to measure so some extrapolation is necessary.

The measured value of the total cross section is of course independent of the choice of renormalisation and factorisation scales. Although the calculated PDF and hard-scattering cross sections are separately dependent on these choices, their convolution should not be (to a particular order). The residual scale dependence is usually estimated by comparing the result for the total cross section calculated at double and half the scale being used. This is used as a measure of whether it is necessary to calculate to higher order or not; the solutions to the DGLAP equations are currently known to NNLO [28, 29].

The treatment of the initial state described here is somewhat simplistic – in this first approximation the colliding partons will be moving in line with the beam, although in a hadronic initial state further emissions from the partons before they participate in the hard collision can result in them acquiring a transverse momentum. This is known as initial state radiation (ISR) and can be simulated in a similar way to the parton shower described below using eq. (3.9), however it is often neglected, particularly in gluon-gluon initial states, and so it will not be discussed further.

### 3.1.3 Parton Showering and Hadronisation

The non-perturbativity of low energy QCD means that the final state of every collision requires the use of information that so far can only be calculated using Monte Carlo simulations. Since these processes happen at such long distance scales, they occur too late to affect the probability of the event occurring, but nonetheless modify the final state that is observed in the detector, so a good understanding is important to correctly reconstruct an event.

A very useful quantity in discussing parton branching is the Sudakov form factor:

$$\Delta_i(t) = \exp\left( -\sum_j \int_{t_0}^{t} \frac{dt'}{t'} \int_0^{1-\epsilon} dz \frac{\alpha(s)}{2\pi} \hat{P}_{ij}(z) \right) , \tag{3.9}$$

which corresponds to the probability for a parton of flavour $i$ to evolve from virtuality $t$ to $t_0$ at a fixed momentum fraction without any resolvable branching. The fixed value $t_0$ is the virtuality threshold, beyond which no further branching will occur. The splitting functions $\hat{P}_{ij}$ are related to those in eqs. (3.1) to (3.4), but without the plus-prescription defined in eq. (3.5), which enforces baryon number conservation. Note that since unitarity demands that the total probability of branching and the probability of not branching must sum to one, the probability of not branching, although derived from the branching probabilities, therefore automatically includes the contribution from loop corrections as well as real emissions.

The Sudakov form factor then allows us to incorporate the *total* probability (to all orders) that a splitting will occur, which can be used in simulations. Given an initial state parton of flavour i with momentum fraction $x_1$ and virtuality $t_1$, it should be possible to generate the next step, $(x_2, t_2)$. First $t_2$ is generated by solving

$$\frac{\Delta_i(t_1)}{\Delta_i(t_2)} = R \tag{3.10}$$

where $R$ is a random number distributed uniformly between 0 and 1; then the momentum fraction $z = \frac{x_2}{x_1}$ is generated similarly according to the splitting function function $P(z)$.

Below the threshold scale $t_0$, it is very unlikely that further splitting will occur. Therefore the algorithm proceeds by starting with the outgoing partons from the final state, and generating successive steps, with each new splitting starting its own evolution branch, until a virtuality $t < t_0$ is generated and no further splitting occurs. The shower terminates when every branch has reached this threshold, which should also occur close to the low-energy regime where QCD becomes non-perturbative, at which point the hadronisation process will take over. The threshold virtuality, $t_0$, is a free parameter, determined by comparing the parton shower and hadronisation combination, and the accepted best-fit value is approximately 1 GeV.

This procedure assumes the final state partons which initialise the shower have some virtuality $t$, which contradicts the assumption made in the hard process calculation that external momenta are on-shell; this is usually dealt with by rescaling the final state momenta and boosting to a new frame at the end of the process.

Once the shower has terminated, the portion of the calculation in which perturbation theory can be applied is finished. The final stage is hadronisation, which must be modelled computationally – two leading models exist, the string model and the cluster model, both based on the principle of parton-hadron duality, which postulates that hadrons will preserve the momentum and quantum number flows of the original final state parton, so for example one would expect to find a hadron near the centre of the jet containing the flavour of parton that emerged from the hard process. A hadronisation algorithm should reproduce several jet properties that are observed; for example a broad $p_T$ distribution is not expected in a single jet, and fragmentation should be at low energies and roughly collinear to the momentum direction of the original parton.

Commonly used parton shower and hadronisation event generators include HERWIG [30], ARIADNE [31] and PYTHIA [32]. PYTHIA and ARIADNE are both based on a 'colour string' model, they use the same JETSET [33] hadronisation algorithm but perform the parton showers differently. The string model assumes that a quark and anti-quark moving away from each other will deposit energy into the colour field between them, which is thought of as a string with an energy density. Quark-antiquark pairs are created out of the vacuum in order to reduce the energy density, and combine with the original quark and anti-quark as well as each other to create hadrons. Gluons are ‘kinks’ in the string that contribute to the momentum distribution and energy density.

HERWIG uses the cluster hadronisation model. The basic idea of this is that final state partons will cluster with vacuum pairs to form colour singlets, and these clusters will split isotropically into two back-to-back hadrons. Both types of model agree well with each other and with data.

The output should be a model of jets as they might appear in a collider, so certain parameters to define a jet (as well as a choice of algorithm) must be specified, for example the maximum $p_T$ at which a parton may be emitted in showering and still be considered to be part of the same jet rather than initialising a new jet, the spatial extent of a jet $\Delta R$, and the scheme used to recombine momenta of individual partons. Typical algorithms base their jet distinctions on a combination of the shape in the detector and their separation.

The variation in jet definition obviously presents a difficulty in studying higher order corrections, for example with one algorithm a process may be included as part of a ‘process + 1 extra jet’ correction, whereas another may assign it to the 2 extra jets category. This is one of the reasons why observables should be as inclusive as possible, covering for example all hadronic final states rather than specifying the number of extra jets. However with careful study this ambiguity can be ironed out, and good algorithms should give consistent and finite results for IR-safe observables, including jet multiplicity.

## 3.2 The LHC

The LHC is a proton-proton collider with a design centre-of-mass energy of 14 TeV, built in a circular tunnel with a circumference of 27 km at CERN, 100 m underneath the Swiss-French border region. Throughout Run I, during 2012-2014, it provided collision data at the lower energies of 7 and 8 TeV; it has just been switched back on at 13 TeV after a maintenance and upgrade period and it is envisioned that it will reach its design energy sometime in 2017. It has four main experiments: ATLAS and CMS are multi-purpose detectors, and it was these collaborations that announced the Higgs discovery. LHCb looks at b-physics, and ALICE is a heavy-ion detector, studying the quark-gluon plasma and other large ion collision physics.

An important quantity in understanding the performance of the LHC is the integrated luminosity,

$$L_{int} = \int L\,dt = \int \frac{N_a N_b f}{A} dt, \tag{3.11}$$

where $N_i$ is the number of particles in beam $i$, $f$ is the frequency of bunch collisions and $A$ is the area of cross-sectional overlap between the two beams. The total number of events is then given by

$$N = L\sigma \tag{3.12}$$

where $\sigma$ is the cross section for an event to occur, which will be discussed in Chapter 4. In practice, the number of events should also be multiplied by an efficiency factor to account for experimental event selection, detector inefficiencies, etc.

The LHC is designed to achieve a bunch-separation time of 25 ns and a bunch-crossing rate of 40 MHz; this corresponds to more than 600 million proton-proton collisions per second.

While in principle it seems like high luminosities are desirable for collecting a lot of data, this presents challenges in being able to distinguish important collisions in many simultaneous events and resetting the trigger and data acquisition hardware quickly enough to record as many interesting events as possible. Run I collected approximately $20\,\mathrm{fb}^{-1}$; the proposed high-luminosity upgrade of the LHC envisions a total integrated luminosity of $3000\,\mathrm{fb}^{-1}$, a factor of 10 improvement on the value expected before the upgrade.[5]

## 3.3 Searching for the Higgs Boson

The general challenges of a hadron collider, which apply to all hadronically induced processes, heave been discussed. However, the LHC was designed with the Higgs discovery in mind, and by the beginning of Run I had been left with a reasonably small search window; LEP had excluded the mass range $M_H \lesssim 114.4$ GeV and electroweak precision tests gave an indirect bound of $M_H \lesssim 158$ GeV [34]. On the 4th of July 2012, the

---

[5] Runs II and III combined (before the high luminosity upgrade) are expected to produce approximately $300\,\mathrm{fb}^{-1}$ of data.

discovery was announced of a resonance with a mass of 125-126 GeV, observed by both ATLAS and CMS [18, 19].

The discovery required sophisticated statistical analysis of the available data in order to be sure that statistical fluctuations were quantified and ruled out in the case of the excess of events of interest. Hypothesis testing requires forming a null or background-only hypothesis (making Monte Carlo based predictions based on a model with no Higgs boson) and a signal-plus-background hypothesis, and testing the data against both options. The p-value measures the probability of a local excess or deficit in a test statistic designed to measure the agreement with a particular hypothesis being due to a statistical fluctuation in the null hypothesis; for a $5\sigma$ deviation, the threshold for discovery, the p-value is about 1 in $3 \times 10^6$. The global p-value quantifies the probability that a deviation seen in *any* region in the data is due to a statistical fluctuation. Taken over a large range, the global p-value is higher than the local p-value – this is known as the look-elsewhere effect.

A further quantity of interest is the signal strength, $\mu$, given by the ratio of the cross section observed to the cross section in the SM hypothesis. The discovered Higgs boson gives a cross section consistent with $\mu = 1$, i.e. is consistent with the SM-like Higgs boson. This does not rule out an extended Higgs sector; it is perfectly possible that the effects of additional Higgs-like particles at high masses on the low-mass Higgs would not be large enough to be observable at current levels of precision.

Since LEP proved unable to reach the Higgs mass, the best choice for a discovery machine was a hadron collider; although a lepton collider is a cleaner environment, synchrotron radiation losses, proportional to $\left(\frac{E}{m}\right)^4$, for an electron-positron collider mean that reaching very high centre-of-mass energies is difficult (although more predictable, since the full beam energy goes into every collision). The Tevatron, Fermilab's proton-antiproton collider, had a maximum centre-of-mass energy of 1.96 TeV and eventually could have discovered the Higgs boson; its CDF and D0 collaborations announced observation of the 125 GeV resonance several months after the LHC [35, 36].

The Higgs production channels at the LHC are shown in figure 3.1. In hadron-hadron collisions at typical LHC centre-of-mass energies, gluon fusion (figure 3.1(a)) is the dominant Higgs production mechanism, even though it is of higher order since it

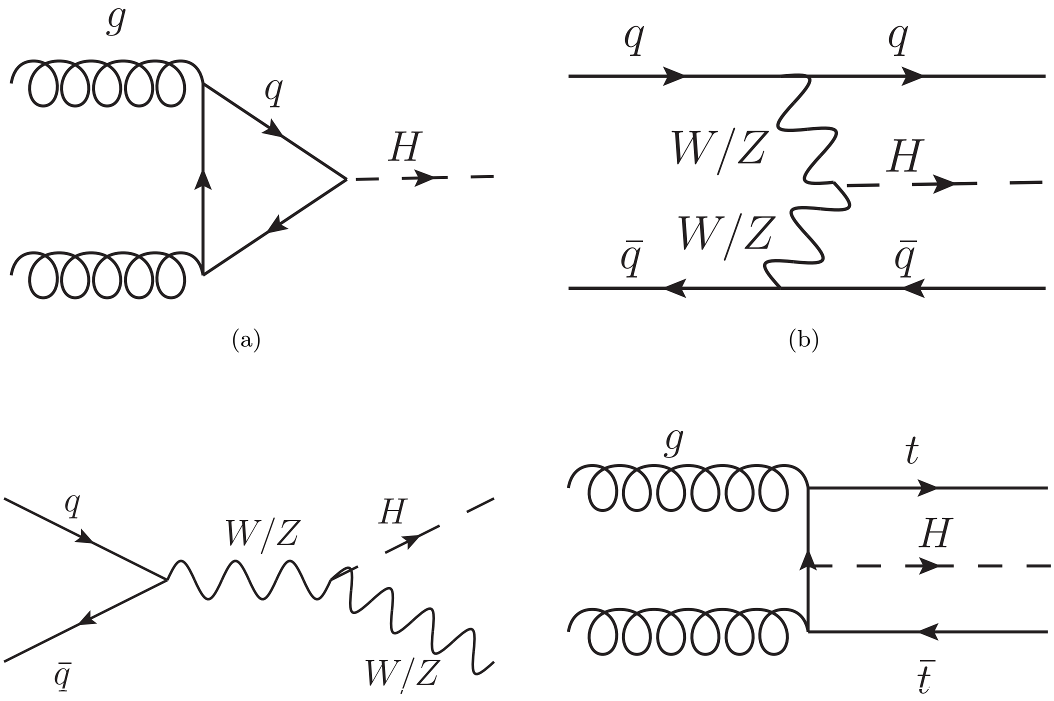

(a) (b)

(c) (d)

Figure 3.1: The Higgs production mechanisms for a hadron collider. The rates of production are given in figure 3.2.

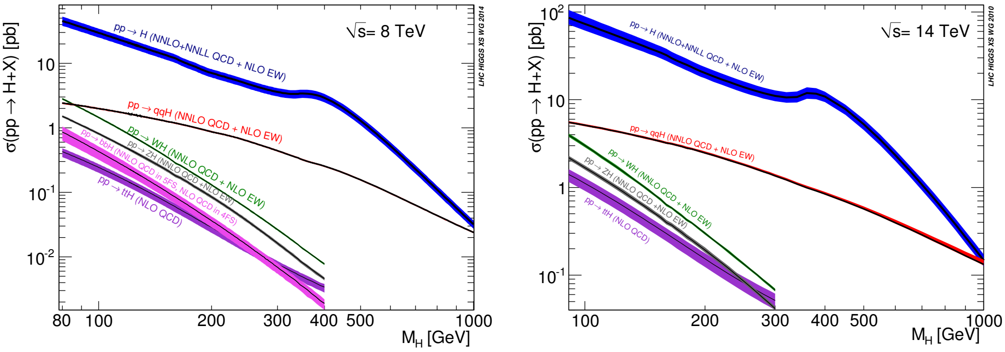

Figure 3.2: Higgs Production cross sections from the Higgs Cross Section Working Group [37] for centre-of-mass energies of 8 TeV and 14 TeV.

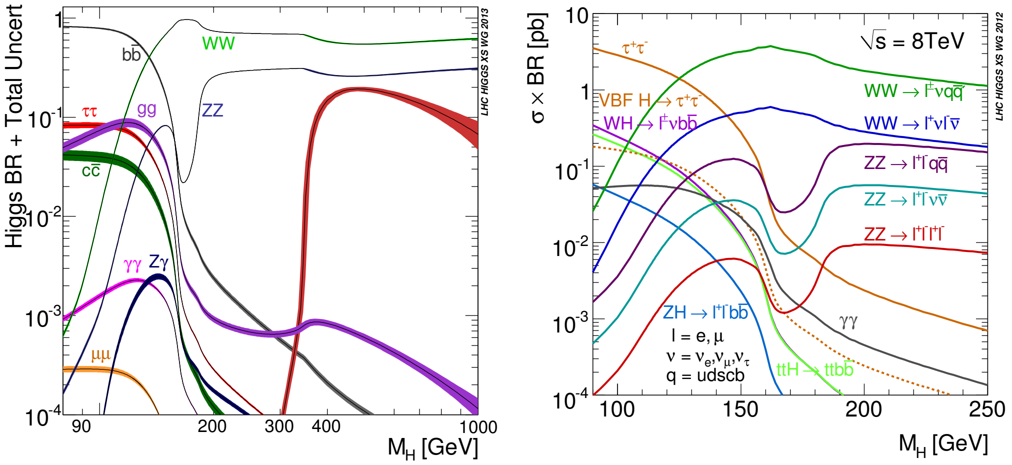

Figure 3.3: Higgs Decay Branching Ratios and Higgs to final state branching ratios from the Higgs Cross Section Working Group [37] for a centre-of-mass energy of 8 TeV.

must be induced by a heavy quark loop. This is mostly due to the very large gluon flux at the low momentum-fraction regions of the phase space that are common at the LHC. The second most important production channel is $qq \to qqH$ (figure 3.1(b)), where incoming quarks radiate vector bosons, which combine to give an $s$-channel Higgs, giving a relatively clean signature of a Higgs decay plus two additional separated jets. This channel is known as vector (or weak) boson fusion (VBF/WBF), and becomes more important at higher energies so is of greater interest for Run II. Other channels of interest are associated production, where a weak boson radiates a Higgs boson (figure 3.1(c)), and $ttH$ associated production (figure 3.1(d)). Figure 3.2 shows the production cross sections at 8 and 14 TeV.

The gluon fusion [38,39], associated weak boson production [40–44] and vector boson fusion [45–48] production cross sections are known to at least next-to-next to leading order (NNLO) in QCD corrections[6] and NLO in EW corrections, and the ttH associated production channel to NLO in QCD [49, 50]. Figure 3.2 shows gluon fusion to NNLO+NNLL (next-to-next-to-leading log) QCD and NLO EW; in fact N$^3$LO (next-to-NNLO) corrections have recently been made available [1]. Calculation to such high orders, which has been a major technical challenge, is motivated by the large scale dependence and bad convergence of the perturbative series at low orders; the NLO result is approximately twice the LO result.

The branching fractions of the various relevant decays of the Higgs boson are shown in figure 3.3, along with the branchings into the various observable final states. The couplings of the Higgs boson to fermions and gauge bosons are proportional to the masses of the particle; although formally it can therefore decay to $e^+e^-$, this decay is not shown because the branching fraction is tiny; note that a log scale is used, and the $\mu^+\mu^-$ branching fraction, although shown, is $O(10^{-4})$.

For the 125 GeV Higgs, the dominant decay channel is $b\bar{b}$, but this channel suffers from a very large irreducible hadronic background, so was not useful as a discovery channel. The $gg$, $\tau^+\tau^-$ and $c\bar{c}$ channels suffer from the same problem; $\tau^+\tau^-$ and $c\bar{c}$ are included in combined analyses but were not used as discovery channels. The decay channels used in the Higgs discovery were the $ZZ$ decay, with a branching fraction of 2.8%, and perhaps surprisingly, the $\gamma\gamma$ channel, which has a branching fraction of only 0.23% and is formally of higher perturbative order than the usual decay mechanisms, since it occurs via a top or weak boson loop (and is therefore a two loop process when initiated by gluon-fusion). However, this channel provides one of the cleanest final states, where the momenta and energy of the two photons are measurable with good resolution in the electromagnetic calorimeters so that the invariant mass of the Higgs can be reconstructed with good precision. This is also true for the $H \to ZZ \to 4\ell$ decay, although this has higher irreducible backgrounds. The dominant background for $\gamma\gamma$ comes from $pp \to \gamma\gamma$, but this background varies smoothly with centre-of-mass energy, so an excess of events close to the Higgs boson mass gives a clear peak above the background, as shown in figure 3.4.

---

[6] QCD corrections are dominant due to the running of $\alpha_s$.

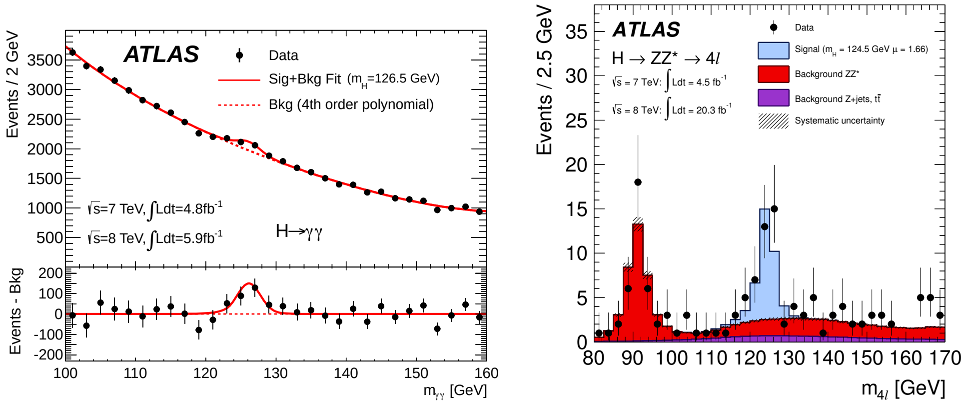

Figure 3.4: ATLAS plots from [19] and [51] showing the $H \to \gamma\gamma$ and $H \to ZZ \to 4\ell$ channels respectively. In each case, an excess of events is clearly visible above the background in the signal region.

The required discovery significance of $5\sigma$ was reached in 2012 in the combined analyses of the ATLAS and CMS detectors in the channels $gg \to H \to ZZ \to \ell\bar{\ell}\ell\bar{\ell}$ and $gg \to H \to \gamma\gamma$ and supported by evidence in the $WW \to \ell\bar{\nu}\bar{\ell}\nu$, $b\bar{b}$ and $\tau^+\tau^-$ channels.

Only the total (combined signal and background) number of events in any region is observable; therefore some method must be used to quantify what is considered an excess in the signal region. In addition to Monte Carlo modelling, comparisons are performed by measuring the background in a region with a very low probability of a signal event occurring, known as a control region, and comparing this to Monte Carlo and theory predictions from which a relationship between the signal and control region can be extrapolated, and the number of background events in the signal region estimated. For the Higgs discovery, ATLAS predicted 4.9 background events in the signal region and observed 13, and CMS predicted 3.8 events and observed 9.

The ATLAS best fit of signal strength was for a Higgs mass of $126.0 \pm 0.4(\text{stat}) \pm 0.5(\text{sys})\,\text{GeV}$ and the corresponding value for CMS was $125.3 \pm 0.4 \pm 0.5\,\text{GeV}$; there is some tension between these two results. This has largely been resolved, the current values are $125.36 \pm 0.36 \pm 0.18\,\text{GeV}$ for ATLAS [52], and $125.02 \pm 0.27 \pm 0.15\,\text{GeV}$ for CMS [53]. A combined analysis has been published [54], giving the currently accepted value of $125.09 \pm 0.21 \pm 0.5\,\text{GeV}$. Two numbers are quoted for uncertainty in each case; the first quantifies statistical error, due to for example random fluctuations in data and fluctuations due to finite simulated sample sizes, and the second is the systematic error, covering effects including uncertainty in the underlying model and in the calibration of measurement apparatus.

The success of Run I means that the Standard Model as we know it is complete. Run II will gather more data on the decays of the Higgs boson into particular final states, allowing most of the couplings to be constrained, although not directly measured. It will also search for new physics beyond the Standard Model, and hopefully hints in the next few years will give much-needed guidance on the goals of the next generation of high energy collider experiments.

## Chapter 4

# Theoretical Predictions for LHC Cross Sections

## 4.1 Cross Sections, Decay Rates and Differential Distributions

Arguably the quantity of most interest both in new physics searches and in precision measurements is the cross section, denoted $\sigma$, for a particular initial state to evolve to a particular final state. This may be defined as a total cross section, measured over the entire phase space, or as a fiducial cross section, where the phase space is defined for a particular process in a particular detector, based on sensitive regions of the detector and regions of the phase space where kinematics allow good signal to background discrimination. The cross section can be interpreted physically as the number of events (collisions) that occur, $N$, divided by the number of particles passing per unit time through the overlapping beam area:

$$\sigma = \frac{N}{\rho_A l_A \rho_B l_B A} = \frac{N}{L} \tag{4.1}$$

where $\rho_i$ is the density of particles in a bunch in beam $i$, $l_i$ is the bunch length and $A$ is the area of overlap between the colliding beams. In fact the densities $\rho_i$ and hence the numbers of particles $N_i$ are not constant within each beam and should be averaged over time. The denominator is then recognisable as the integrated luminosity of eq. (3.11), which can be measured using Standard Model 'candles' such as the Drell-Yan process, so assuming that the process and detector are sufficiently well understood and it is possible to count the number of events of interest, the goal for theorists and phenomenologists is to provide a value for the cross section, allowing a direct comparison. The cross section has units of area, in SI units measured in $\mathrm{m}^2$, but more commonly quoted in barns: $1\,\mathrm{b} = 10^{-24}\mathrm{cm}^2$.

A related class of comparable quantities are differential cross sections, the rate of change of the total cross section with respect to a particular observable $O$, defined by

$$\sigma = \int_{O_{min}}^{O_{max}} \frac{d\sigma}{dO} dO. \tag{4.2}$$

These can be visualised in differential distributions of observables measured event-by-event in the detectors such as transverse momentum, invariant mass (or missing transverse momentum if dealing with invisible particles), azimuthal opening angle between particular particles, and many others. The y-axis value will be proportional to the number of events observed with a value of $O$ in the bin range $dO$.

It will be shown later in this chapter that the Monte Carlo integration performed to obtain a cross section is very similar to simulating events such as might be observed in a detector, so keeping track of the event-by-event values of observables required to produce differential distributions for comparison is not difficult. In addition to providing another comparison between data and the predictions of a particular theory, differential distributions are helpful for example in deciding on selection cuts that enhance the signal to background ratio, and also in the study of particle properties. Studying angular distributions can also give information about the spin of a new particle, which is not directly measurable.

The final related quantity of interest is the total decay rate, $\Gamma$, which describes the probability per unit time of an unstable particle decaying. In the differential distributions just described, an unstable particle of mass $M$ that decays to other particles will be visible as a Breit-Wigner peak in the invariant mass squared distribution, with the shape of the peak described by

$$f(q^2) \sim \frac{1}{(q^2 - M^2)^2 + M^2\Gamma^2}. \tag{4.3}$$

$\Gamma$ then corresponds to the width of the Breit-Wigner resonance peak in the distribution. For this reason, an unstable particle is often referred to as a 'resonance' and the total decay rate of the unstable particle is equal to the width of the resonance. This is an intrinsic property of any unstable particle, and is a quantity of great interest in the discovery of new particles - if the total decay rate can be measured and matched to predictions, this means that all allowed (non-negligible) decays have been accounted for. Partial decay rates $\Gamma_i$ to decay channel $i$ are also useful since these depend on the couplings in that channel, which must be measured as well as possible in order to fix free parameters in the SM. In the case of the Higgs boson, the predicted total width is extremely small, around 4 MeV, and it is unlikely that it will be possible to measure the total decay rate at the LHC with sufficient accuracy to say whether there are any decays unaccounted for or not.[1] Branching fractions, the ratio of a partial decay rate for a particular channel to the total decay rate, are also of interest.

The importance of being able to predict cross sections for comparison to experimental results is clear. Theoretical calculations are possible to a particular order in perturbation theory by calculating the matrix element, denoted $\mathcal{M}$, also known as the scattering amplitude, for a given initial state to evolve to a given final state. Formally, the scattering amplitude describes the overlap of the initial and final state wave packets with a function governed by the interaction Hamiltonian. The cross section is then calculated by integrating the squared matrix element over all external momenta and enforcing conservation of four-momentum:

$$\sigma_{A,B\to f} = \int \frac{1}{2\hat{s}} \prod_f \frac{d^3 p_f}{(2\pi)^3} \frac{1}{2E_f} \delta^4\Big(p_A + p_B - \sum_f p_f\Big) \Big|\mathcal{M}\big(p_A + p_B \to \{p_f\}\big)\Big|^2 \tag{4.4}$$

for an initial state of particles A and B colliding and producing an unspecified final state

---

[1] It will certainly not be possible to perform a direct measurement, as the momentum resolution is not good enough - a direct measurement would most likely require a muon collider, which is not on the present horizon of future accelerators. Possibilities for an indirect measurement are discussed in section 4.5.

of two or more particles, denoted $f$. $p_i$ refers to the 4-momentum of particle $i$, $E_i$ its energy and $\hat{s}$ the square of the total *parton* centre-of-mass energy (which will be some fraction of the total available centre-of-mass energy).

In a hadron collider, the question of what constitutes the initial state must be treated more carefully, as was discussed in Chapter 3. Including the parton distribution function $f(x, \mu_f^2)$ and integration over the parton's momentum $x_i$ as a fraction of the available momentum for each beam then gives, for the total cross section at a hadron collider:

$$\sigma_{had} = \sum_{A,B} \int_0^1 dx_1 \int_0^1 dx_2 \, f_{1\to A}(x_1, \mu_f^2) f_{2\to B}(x_2, \mu_f^2) \sigma_{A,B\to f} \tag{4.5}$$

where $\mu_f$ is the factorisation scale.

Different techniques have been developed to perform such calculations efficiently. The commonly used Feynman diagram approach is simple to understand, and straightforward to implement in an algorithm, but a process with $N$ diagrams at first glance requires calculation of $O(N^2)$ individual terms. Processes with large numbers of external legs or calculated to high orders may have huge numbers of diagrams and a brute-force approach is therefore not suitable for modern applications where in some cases N$^3$LO precision is required. The memory and CPU time requirements are unreasonable, and alternatives must be found.

Fortunately, a technique has been developed that allows a way around this by evaluating the scattering amplitude directly before squaring by representing all external particles and intermediate resonances as two-component helicity spinors and dramatically reducing the number of expressions by exploiting identities for spinor products and introducing colour decomposition. This is known as a helicity amplitude approach, and most modern algorithms take advantage of this method.

Even with these simplifications, there are still expressions to be integrated that may include complicated tensor structures, and although tensor reduction methods combined with helicity amplitudes allow the integrals to be grouped into combinations of lower rank master integrals, many integrals considered in particle physics are generally not analytically solvable. This is the limit of what analytic calculations alone can do - at this point making a cross section prediction requires the use of numerical methods, in particular Monte Carlo integration, which is the subject of section 4.3.

Aside from the complexity in the number of expressions, there is the issue of performing the large-dimensional phase space integral. Including the initial state momentum fraction integrations (only required for a hadron collider), a four-particle final state requires a ten-dimensional integration.[2] Again, Monte Carlo integration will provide an efficient way to do this.

## 4.2 Hadron Collider Observables

In a hadron collider, the parton centre-of-mass frame does not coincide with the lab frame (hadron centre-of-mass frame), since although the protons have equal and opposite momenta, the individual partons which form the initial state of the hard process do not. The lab frame and the centre-of-mass frame are related by a boost along the axis of the beam line, usually chosen as the $z$-axis in the frame of reference - therefore any hadron collider observable $O$ should also be invariant under a $z$-boost. Care must be taken with the definition of rapidity: the quantity

$$y = \tanh^{-1}\left(\frac{p_z}{E}\right) = \frac{1}{2}\ln\left(\frac{E+p_Z}{E-p_Z}\right), \tag{4.6}$$

is not itself $z$-boost invariant but the difference of two rapidities is.

The other requirements for a good observable still apply; they should be measurable for the process under consideration, for example invariant mass is a good observable in a process where the final state particles are charged and energetic, so that they are visible in detectors, but it is not a suitable observable for final states that contain neutrinos.

The more inclusive the cross section, considering for example final state with all hadronic additions rather than just final state or final state with 1 additional jet, the more reliable our predictions are, since exclusive cross sections may have unwanted dependancies, for example on the jet definition algorithm. Also, the precision of observables is ultimately limited by the precision of the PDFs, so errors on the PDF should be well quantified.

---

[2] For an n-particle final state there will be 3n-4 degrees of freedom, with an additional 2 added for initial state momentum fractions in a 2-particle hadronic initial state.

Typical hadron collider observables generic to many processes include transverse momentum $p_T$ $\left(= \sqrt{(p_x)^2 + (p_y)^2}\right)$ and azimuthal opening angle between two particles $\Delta\phi$. Secondary observables, i.e. those derived from primary observables rather than measured directly, are also useful, such as transverse energy $E_T$ $\left(= \sqrt{p_T^2 + m^2}\right)$,[3] invariant mass for groups of massive particles, transverse mass,[4] rapidity difference $\Delta y$, or $\Delta R = \sqrt{\Delta y^2 + \Delta\phi^2}$ which is a measure of separation and is useful in defining the point at which a jet emission becomes a new jet.

## 4.3 Monte Carlo Integration

Monte Carlo integration is one of the most popular methods of numerical integration, and there are well established algorithms to perform it efficiently. The basis of the method is the fact that given an integrable[5] function $f(x)$ to be integrated over $x$, the integral $I$ can be approximated as:

$$I = \int d^n x f(x) \approx V \cdot \langle f \rangle = V \cdot \frac{1}{N} \sum_{i=1}^{N} f(x_i) \,. \tag{4.7}$$

where $V = \int d^n x$. By sampling enough randomly distributed points, one hopes to build up a good picture of the true function. The error of this method is related to the variance:

$$Var(f) = \langle f^2 \rangle - \langle f \rangle^2 \tag{4.8}$$

by

$$Err(I) = \sqrt{\frac{Var(f)}{N}} \tag{4.9}$$

For a constant function the sample at every point will be equal and the average will give exactly the correct answer. For a more complicated function, particularly those of the type considered in particle physics that have strongly peaked resonances, the precision relies on firstly having enough points that the resonance is not completely

---

[3] A different definition of $E_T$ which is often used by experimentalists is $E_T = E \sin\theta = E \frac{p_T}{|\vec{p}|}$, but this is not invariant under $z$-boosts.

[4] For a single particle, transverse mass is defined as the boost-invariant $E_T$ above, but it has varying definitions for groupings of particles. E.g. when studying a process containing a $WW \to 2\ell 2\nu$ decay, ATLAS define $M_{T,WW} = \sqrt{((M_{T,\ell\ell} + M_{T,miss})^2 - (\vec{p}_{T,\ell\ell} + \vec{p}_{T,miss})^2}$ where $M_{T,\ell\ell} = \sqrt{p_{T,\ell\ell}^2 + M_{\ell\ell}^2}$

[5] In fact, it should also be square integrable in order to calculate the error.

missed, especially if it has a narrow width, and secondly having enough points in the resonant region to build up a good picture of its contribution to the integration.

A Monte Carlo (MC) generator typically generates random numbers on a unit hypercube with dimension equal to the number of degrees of freedom. Any phase space parametrisation will therefore contain a mapping of these random numbers,

$$f : r \to PS. \tag{4.10}$$

for an $m$-dimensional vector $r$, a 4-momentum configuration PS and a single mapping $f$. This choice of mapping is not unique.

A common approach to improving convergence is to perform a mapping of the integrand to a flatter function. Describing the total cross section as a product of all phase space (including parton momentum fraction) contributions, called $\Phi(PS)$, and everything else (the matrix element, parton distribution functions, any required spin sums etc.), called $h(PS)$, one can then write

$$\sigma = \int h(PS) d\Phi(PS) = \int h\big(f(r)\big)\, g\big(f(r)\big)\, dr \tag{4.11}$$

where the function $g$ is simply the Jacobian of the transformation. The mapping $f$ will be well chosen such that $g\left(f\left(r\right)\right)$ is similar to the inverse of $h\left(f\left(r\right)\right)$, so that their product leaves a considerably flatter integrand in the new variables.

A basic Monte Carlo generator simply generates points in the phase space and evaluates the function at each point. However, a more intelligent way to do this is to use sampling: while by default a uniform distribution might be chosen, points in the phase space where either the function is large or the variance is large (the choice of which is more important varies in different implementations) deserve more investigation, so the random number generation should be adapted on subsequent iterations to generate more points in interesting regions. Note that the non-uniform distribution employed in importance sampling necessitates a reweighting at each phase space ‘shot’.

### 4.3.1 Multi-Channel Mappings

In particle physics applications, a more sophisticated approach is generally needed since quantities of interest, like cross sections, require the integration of the squared sums of diagrams with differing kinematic structures (containing different singular or strongly peaked regions) that must be integrated over a large dimensional phase space. In simpler processes, there may be few enough kinematic structures that it may be possible to divide the phase space into different regions, assume a particular type of structure to be dominant in each region so that one mapping is used for each region, and sum the results. This was the approach taken in the fully leptonic implementations in `gg2VV`. However for more complicated cases, such as the semi-leptonic decays described in Chapter 6, this approach is not suitable.

The semi-leptonic decays (via two vector bosons) of the Higgs Boson differ fundamentally from the fully leptonic decays in that they have a tree-level background, which is of lower order than the loop-induced signal process. If one wishes to consider the background to the loop induced signal processes

$$gg \to H \to \ell\bar{\nu}q\bar{q}'/\ell\bar{\ell}q\bar{q}, \tag{4.12}$$

there are then two types of contributions: tree-level diagrams, as shown in figure 4.1 with a single vector boson, and loop continuum diagrams, as shown in figure 4.2, with two vector bosons. The fully leptonic decays only have the latter background. For example, the inclusion of tree level diagrams adds 8 possible kinematic 'channels' for the $WW$ case (3 unique types as shown, and 5 duplicates with certain permutations that alter the kinematic structure) with overlapping regions of importance and the approach of dividing up the phase space is no longer feasible.

In `gg2VV`, multi-channel[6] mappings [55] have been chosen to deal with this problem. In cases where the integrand under consideration is described by a sum of many Feynman diagrams, each with their own phase space structure, it is appropriate to have a mapping for each of $N$ classes of diagrams ('channels'). The overall weight for each phase space

---

[6] The terminology 'channel' is confusing but common in the literature - it refers not to the usual channel in the sense of a decay channel, where each channel would be a different process, but to the different types of Feynman diagrams (kinematic structures/channels) in a single process.

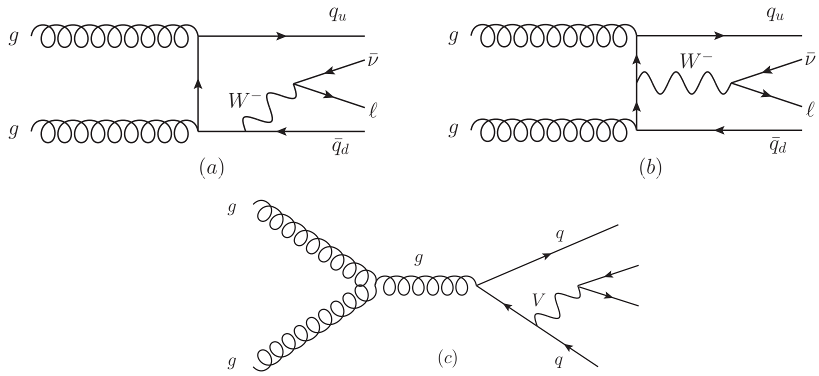

Figure 4.1: Representative tree-level background diagrams for the semi-leptonic processes considered in gg2VV.

point, which for a single mapping was simply the Jacobi determinant, is now obtained from the weighted inverse sum of the Jacobi determinants from all channels:

$$g\left(f\left(r\right)\right)=\left(\sum_{i=1}^{N}\alpha_i\frac{1}{g_i\left(f\left(r\right)\right)}\right)^{-1}. \tag{4.13}$$

The $\alpha_i$ are weights required to preserve unitarity; their only a priori requirement is that they sum to 1, so it is reasonable to initially set them equal to the inverse of the number of mappings, but a possible improvement to this will be discussed briefly below.

Each mapping is designed to deal with a particular structure, and it can be assumed that typically one type of diagram will dominate at a particular point of phase space. The idea now is that in a small enough sub-volume of the total phase space volume, $h\left(PS\right)g_i\left(PS\right)\approx 1$ for some $i$. The integrand becomes:

$$\begin{aligned}\int h\left(PS\right)d\Phi\left(PS\right) &= \int h\left(PS\right)g\left(PS\right)\,\frac{d\Phi\left(PS\right)}{g\left(PS\right)}\\ &= \sum_i \alpha_i\int h\left(PS\right)g\left(PS\right)\,dr\end{aligned} \tag{4.14}$$

Note that in fact a separate mapping is not necessary for the third diagram of figure 4.1 and its duplicate, since the singularity in these diagrams coincides with the phase space volume going to 0, and so the number of required $WW$ tree-level background mappings is reduced to 6.

Such an approach is ideal for algorithmic computation, as different kinematic chan-

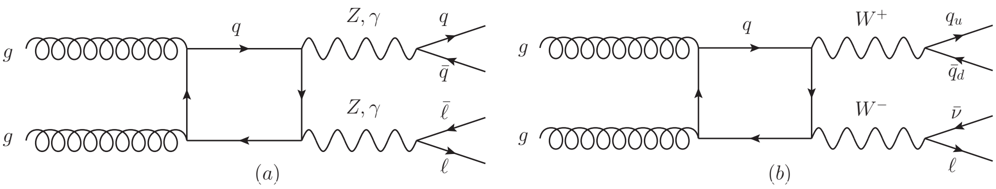

Figure 4.2: Representative one-loop background diagrams for the semi-leptonic processes considered in gg2VV.

nels have some common components. In section 4.3.2 all structures that are used in the Feynman diagrams shown in figure 4.1 and figure 4.2 are described. For computation, it is necessary to know the mappings between the random number variables distributed on a unit hypercube and the phase space variables (usually final state momenta and initial state momentum fractions), and the Jacobi determinants for these mappings.

As a full example, the channels implemented in the semi-leptonic process in gg2VV are given below. Firstly, the components common to several mappings are described in detail, followed by the random number transformations and Jacobi factor for each separate mapping.

### 4.3.2 Mapping Components

#### Two-Body Decay

In the parton centre-of-mass frame, it is useful to consider the kinematics of an initial state with momentum $p = (E, \vec{p})$ (note that this can be a single particle initial state or a configuration with total momentum p) decaying to two particles with momentum $p_1$ and $p_2$; the phase space volume element is denoted by $d\phi_2(p; p_1, p_2)$. It is relevant to note that $p_i^2 = M_i^2$, $E = E_1 + E_2$ by conservation of energy, $M_i^2 = E_i^2 - |\vec{p}|^2$ and $\vec{p_1} = -\vec{p_2}$ in the centre-of-mass frame which is considered here. There is an additional kinematic constraint, $E_{CM} = \sqrt{p^2} > M_1 + M_2$. Combined, these identities lead to:

$$E_1 = \frac{E^2 + M_1^2 - M_2^2}{2E} \qquad\qquad E_2 = \frac{E^2 + M_2^2 - M_1^2}{2E} \tag{4.15}$$

and

$$|p_1| = \frac{1}{2E}\sqrt{\left(E^2 - (M_1 - M_2)^2\right)\left(E^2 - (M_1 + M_2)^2\right)} \tag{4.16}$$

The phase space element is

$$d\phi_2 = \frac{1}{16\pi^2}\frac{|\vec{p_1}|}{E}d\Omega_1 = \frac{1}{16\pi^2}\frac{|\vec{p_1}|}{E}d\cos\theta_1 d\phi_1. \tag{4.17}$$

In this simple case, the decay can be taken to be isotropic with respect to the azimuthal and polar angles, and so random numbers can be assigned to the two angular degrees of freedom according to

$$\begin{gathered} \cos\theta_1 = 2r_1 - 1 \to d\cos\theta_1 = 2dr_1 \\ \phi_1 = 2\pi r_2 \to d\phi_1 = 2\pi dr_2 \end{gathered} \tag{4.18}$$

so that the total transformation is

$$d\phi_2 = \frac{\sqrt{\left(E^2 - (M_1 - M_2)^2\right)\left(E^2 - (M_1 + M_2)^2\right)}}{32\pi^2 E^2} 4\pi dr_1 dr_2. \tag{4.19}$$

This 2−body decay will appear in many other examples, so it is helpful to define the notation

$$\lambda\left(E_{CM}^2, M_1^2, M_2^2\right) = \left(E^2 - (M_1 - M_2)^2\right)\left(E^2 - (M_1 + M_2)^2\right) \tag{4.20}$$

**Breit-Wigner Propagator**

A Breit-Wigner propagator is a common component of the integrand for any process containing a resonance, and is integrated over its virtuality $q^2$. It has the general form

$$\int_{q^2_{min}}^{q^2_{max}} \frac{dq^2}{2\pi}\frac{1}{(q^2 - M^2)^2 + (M\Gamma)^2} \tag{4.21}$$

and for small $\frac{\Gamma}{M}$ has a strong peak in the region $q^2 \sim M^2$. Performing a change of variables,

$$z = \arctan\left(\frac{q^2 - M^2}{M\Gamma}\right) \to dq^2 = \frac{(q^2 - M^2)^2 + (M\Gamma)^2}{M\Gamma}dz, \tag{4.22}$$

the Jacobian factor perfectly compensates for the peaked structure. The integrand is then:

$$\int_{q^2_{min}}^{q^2_{max}} \frac{dq^2}{2\pi} \frac{1}{(q^2 - M^2)^2 + (M\Gamma)^2} = \int_{z_{min}}^{z_{max}} \frac{1}{2\pi M\Gamma}\, dz, \tag{4.23}$$

which is constant and trivial to integrate.

The mapping to the random number is given by

$$z = z_{min} + (z_{max} - z_{min})\, r \rightarrow dz = (z_{max} - z_{min})\, dr \tag{4.24}$$

so that the full mapping from $q^2$ to $r$ will be

$$\int_{q^2_{min}}^{q^2_{max}} dq^2 = \int_0^1 \frac{(q^2 - M^2)^2 + (M\Gamma)^2}{M\Gamma} (z_{max} - z_{min})\; dr. \tag{4.25}$$

### Massless $s$-Channel Propagator

A massless $s$-channel propagator with virtuality $q^2$ will appear in an amplitude calculation as

$$\int_{q^2_{min}}^{q^2_{max}} \frac{dq^2}{2\pi} \frac{1}{\left(q^2\right)^n} \tag{4.26}$$

for an exponent $n$, which is chosen empirically to be equal to $\frac{3}{2}$. This expression is singular in the $q^2 \rightarrow 0$ limit, so there is a kinematic constraint of $q^2 > 0$. The mapping is

$$x = \frac{(q^2)^{1-n}}{1-n} \rightarrow dx = \frac{1}{(q^2)^n} dq^2 \tag{4.27}$$

and the mapping to the random number is simply

$$x = x_{min} + (x_{max} - x_{min})r \rightarrow dx = (x_{max} - x_{min})dr. \tag{4.28}$$

The full mapping from $q_2$ to $r$ is then:

$$\int_{q^2_{min}}^{q^2_{max}} dq^2 = \int_0^1 dr\, (q^2)^n (x_{max} - x_{min}). \tag{4.29}$$

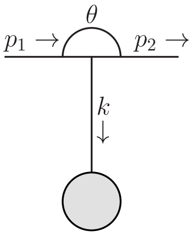

Figure 4.3: Layout of notation for a mapping with a massless $t$-channel propagator

### Massless *t*-Channel Propagator

A massless $t$-channel propagator, as shown in figure 4.3, appears in the amplitude as a factor $\propto \frac{1}{(k^2)^n}$ where the exponent $n$ is close to but not equal to 1 (in fact it is usual to take $n = 0.9$). Then,

$$\begin{aligned} k^2 = (p_1 - p_2)^2 = p_1^2 + p_2^2 - 2p_1 \cdot p_2 &= M_1^2 + M_2^2 - 2E_1E_2 + 2\,|\vec{p_1}|\,|\vec{p_2}|\cos\theta \\ &= M_1^2 + M_2^2 - 2E_1E_2 + 2\,|\vec{p_1}|\,|\vec{p_2}|\cos\theta \end{aligned} \tag{4.30}$$

The integration variable is $\cos\theta$, restricted to the range $-1 \leq \cos\theta_{min} < \cos\theta_{max} \leq 1$. This gives (for $k^2 < 0$):

$$\frac{d\cos\theta}{-k^2} = \frac{1}{2\,|\vec{p_1}|\,|\vec{p_2}|}\cdot\frac{d\cos\theta}{\frac{2E_1E_2 - M_1^2 - M_2^2}{2|\vec{p_1}||\vec{p_2}|} - \cos\theta}. \tag{4.31}$$

Letting

$$\frac{2E_1E_2 - M_1^2 - M_2^2}{2\,|\vec{p_1}|\,|\vec{p_2}|} = a, \tag{4.32}$$

and $y = a - \cos\theta$, as in the case of the massless $s$-channel propagator the mapping eq. (4.27) can be used, and the random number mapping is eq. (4.28). The expression in the amplitude will look like (discounting factors constant with respect to the $\cos\theta$ integration)

$$\int_{\cos\theta_{min}}^{\cos\theta_{max}} \frac{d\cos\theta}{(a - \cos\theta)^n} = \int_{y_{min}}^{y_{max}} \frac{dy}{y^n} = \int_{x_{min}}^{x_{max}} \frac{y^n}{y^n} dx \tag{4.33}$$

In total,

$$\int_{\cos\theta_{min}}^{\cos\theta_{max}} d\cos\theta = \int_{x_{min}}^{x_{max}} y^n dx = \int_0^1 y^n \left(x_{max} - x_{min}\right) dr. \tag{4.34}$$

### 2→2 Decay

For a general hadronic two-particle to two-particle decay, there will be two extra degrees of freedom compared to the simple two-body decay, arising from $p = x_A p_A + x_B p_B$ where $x_i$ and $p_i$ denote the fraction of momentum carried by the parton originating in hadron $i$ and the momentum of hadron $i$ respectively. The full phase space element becomes $dx_A\, dx_B\, d\phi_2$. $x_A$ and $x_B$ are constrained to be between 0 and 1, so the trivial mapping

$$\begin{aligned} x_A &= r_1 \to dx_A = dr_1 \\ x_B &= r_2 \to dx_B = dr_2, \end{aligned} \tag{4.35}$$

can be used, giving the total phase space element (in the centre-of-mass frame):

$$dx_A dx_B d\phi_2 = \frac{\sqrt{\left(E^2 - (M_1 - M_2)^2\right)\left(E^2 - (M_1 + M_2)^2\right)}}{8\pi E^2} dr_1 dr_2 dr_3 dr_4. \tag{4.36}$$

### Special case: 2→2 with Intermediate Resonance

If there is an intermediate massive, $s$-channel propagator with mass $M$ and decay width $\Gamma$, for small $\frac{\Gamma}{M}$ it will have a pronounced Breit-Wigner peak, contributing a factor to the amplitude of the form shown in eq. (4.21). Some modifications are made to the $2 \to 2$ prescription above, since the resonance is greatly enhanced when the propagator has a virtuality (corresponding to the parton centre-of-mass energy by conservation of momentum) in a narrow region around the peak value of $q^2 = M^2$, so generating $x_A$ and $x_B$ uniformly across the whole phase space will be inefficient and it is necessary to compensate for the (difficult to integrate) Breit-Wigner peak in the squared amplitude.

Denoting the centre-of-mass energy squared by $s$ and the parton centre-of-mass energy squared by $\hat{s}$, note that the parton momentum fractions $x_A$ and $x_B$ from the previous section satisfy $\hat{s} = x_A x_B s$. It is then useful to define $\tau = x_A x_B = \frac{\hat{s}}{s}$.

In this case, the virtuality $q^2$ of the Breit-Wigner propagator will coincide with the total parton centre-of-mass energy, $\hat{s}$. Using eqs. (4.22) and (4.24) to assign $\hat{s}$ between 0 and $s$ (but overwhelmingly most probably close to $M^2$) and eq. (4.22) to perform the mapping, the integration is transformed according to:

$$\begin{aligned}\int_0^1 d\tau = \frac{1}{s}\int d\hat{s} &= \int_{z_{min}}^{z_{max}} \frac{1}{s}\frac{(\hat{s}-M^2)^2+(M\Gamma)^2}{M\Gamma}dz \\ &= \int_0^1 \frac{1}{s}\frac{(\hat{s}-M^2)^2+(M\Gamma)^2}{M\Gamma}\left(z_{max}-z_{min}\right)dr.\end{aligned} \tag{4.37}$$

The factor of $\frac{(\hat{s}-M^2)^2+(M\Gamma)^2}{M\Gamma}$ will cancel with the Breit-Wigner propagator in the amplitude.

It is convenient to parametrise the other initial state degree of freedom as the boost rapidity of the centre-of-mass frame:

$$y = \frac{1}{2}\ln\frac{x_1}{x_2} \tag{4.38}$$

which, knowing $\tau$, can be assigned according to

$$y = \frac{1}{2}\ln\tau - \ln\tau\, r_2 \to dy = -\ln\tau dr_2. \tag{4.39}$$

Combining this with the two body decay, the total transformation is then

$$\begin{aligned}&\int_0^1 \frac{1}{s}d\tau\int_{\frac{1}{2}\ln\tau_{min}}^{\frac{1}{2}\ln\tau_{max}} dy\, d\phi_2 = \int_0^1 dr_1 dr_2 dr_3 dr_4\ \frac{1}{s}\left(\arctan\frac{s-M^2}{M\Gamma} - \arctan\frac{-M^2}{M\Gamma}\right) \\ &\ln\tau\frac{(\hat{s}-M^2)^2+(M\Gamma)^2}{M\Gamma}\frac{\sqrt{\left(E^2-(M_1-M_2)^2\right)\left(E^2-(M_1+M_2)^2\right)}}{8\pi E^2}\end{aligned} \tag{4.40}$$

**Special Case: 2→2 Decay with massless *t*-channel propagator**

The 2 → 2 decay with an intermediate massless $t$-channel propagator does not place restrictions on the initial state momentum fractions, so they can be generated them uniformly according to eq. (4.35). Once these are assigned, assuming the colliding particles are massless and the parton centre-of-mass frame is used, $a$ can be determined from eq. (4.32). The 2 body decay can then be calculated as in eq. (4.17) with the $\cos\theta$ integration performed according to the massless $t$-channel propagator mapping, eq. (4.34).

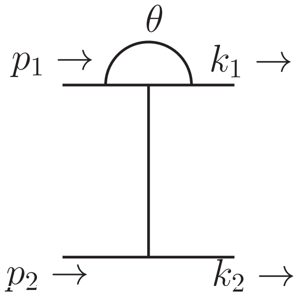

Figure 4.4: Layout of notation for 2 → 2 decay with a massless $t$-channel propagator

The phase space volume for the 2 → 2 decay with a massless $t$-channel propagator as in figure 4.4 is then (assuming the colliding particles are also massless):

$$\begin{aligned}&\int_0^1 dx_A \int_0^1 dx_B \int_{\cos\theta_{min}}^{\cos\theta_{max}} \frac{d\cos\theta}{k^2} d\phi_2 = \\ &\int_0^1 \frac{\lambda^{\frac{1}{2}}\left(E_{CM}^2, k_1^2, k_2^2\right)}{32\pi^2 E_{CM}^2} 4\pi\left(x_{max} - x_{min}\right) dr_1 dr_2 dr_3 dr_4 dr_5.\end{aligned} \tag{4.41}$$

where $\lambda^{\frac{1}{2}}\left(E_{CM}^2, k_1^2, k_2^2\right)$ is defined in eq. (4.20) and

$$\begin{aligned}x_{max/min} &= \frac{(y_{max/min}^2)^{1-n}}{1-n} \\ y_{max/min} &= \frac{E_{CM}E_{k1} - k_1^2}{E_{CM}\left|\vec{k}_1\right|} - \cos\theta_{max/min}\end{aligned} \tag{4.42}$$

**General Three-Body Decay**

For a general three-body decay, where $p$ is the incoming momentum:

$$\begin{aligned} d\phi_3(p;k_1,k_2,k_3) &= (2\pi)^4\,\delta\left(p-k_1-k_2-k_3\right)\frac{d^3k_1}{(2\pi)^3\,2E_1}\frac{d^3k_2}{(2\pi)^3\,2E_2}\frac{d^3k_3}{(2\pi)^3\,2E_3} \\ &= \frac{d^3k_1}{(2\pi)^3\,2E_1}(2\pi)^4\,\delta\left((p-k_1)-k_2-k_3\right)\frac{d^3k_2}{(2\pi)^3\,2E_2}\frac{d^3k_3}{(2\pi)^3\,2E_3} \\ &= \frac{d^3k_1}{(2\pi)^3\,2E_1}d\phi_2\left(p-k_1;k_2,k_3\right) \\ &= \frac{\left|\vec{k}_1\right|^2 d\left|\vec{k}_1\right| d\Omega_1}{(2\pi)^3\,2E_1}\frac{1}{16\pi^2}\frac{\left|\vec{k}_2^{\,CM23}\right|}{E_{CM23}}d\Omega_2^{CM23} \\ &= \frac{1}{16\,(2\pi)^5}\left|\vec{k}_1\right| dE_1 d\Omega_1\,\lambda^{\frac{1}{2}}\left(1,\frac{M_2^2}{s_{23}},\frac{M_3^2}{s_{23}}\right)d\Omega_2^{CM23} \end{aligned} \tag{4.43}$$

where $E_1 = \sqrt{\left|\vec{k}_1\right|^2 + M_1^2}$ and so $\frac{dE_1}{d\left|\vec{k}_1\right|} = \frac{\left|\vec{k}_1\right|}{E_1}$. Also, $d\Omega_1 = d\cos\theta_1 d\phi_1$; $d\Omega_2^{CM23} = d\cos\theta_2^{CM23} d\phi_2^{CM23}$. All polar and azimuthal angles $\theta_i$ and $\phi_i$ refer to the angles between outgoing particle $i$ in the specified frame with the total incoming momentum.

The random numbers are assigned according to

$$\begin{aligned} \cos\theta_1 = 2r_1 - 1 &\rightarrow d\cos\theta_1 = 2dr_1 \\ \phi_1 = 2\pi r_2 &\rightarrow d\phi_1 = 2\pi dr_2 \end{aligned} \tag{4.44}$$

and similarly for $\phi_2^{CM23}$ and $\cos\theta_2^{CM23}$ with $r_2$ and $r_3$. A fifth degree of freedom is assigned according to:

$$E_1 = E_{1,min} + \left(E_{1,max} - E_{1,min}\right) r_5 \rightarrow dE_1 = \left(E_{1,max} - E_{1,min}\right) dr_5. \tag{4.45}$$

In the centre-of-mass frame, the kinematic limits for $E_1$ are determined by

$$M_1 \leq E_{1,min}^{CM} < E_{1,max}^{CM} \leq \frac{E_{CM}^2 + M_1^2 - (M_2+M_3)^2}{2E_{CM}} \tag{4.46}$$

and also

$$\begin{aligned}
\left|\vec{k}_1^{CM}\right| &= \left(\left(E_1^{CM}\right)^2 - M_1^2\right)^{\frac{1}{2}} \\
s_{23} &= E_{CM}^2 + M_1^2 - 2E_{CM}E_1^{CM} \\
\left|\vec{k}_2^{CM23}\right| = \left|\vec{k}_3^{CM23}\right| &= \frac{\lambda^{\frac{1}{2}}\left(s_{23}, M_2^2, M_3^2\right)}{2E_{23}^{CM23}} = \frac{\lambda^{\frac{1}{2}}\left(s_{23}, M_2^2, M_3^2\right)}{2\sqrt{s_{23}}^{CM23}}.
\end{aligned} \tag{4.47}$$

The general three-body phase space element can then be written as:

$$d\phi_3 = \frac{1}{4\left(2\pi\right)^3}\int_0^1 \left(E_{1,max} - E_{1,min}\right)\left|\vec{k}_1\right|\lambda^{\frac{1}{2}}\left(1, \frac{M_2^2}{s_{23}}, \frac{M_3^2}{s_{23}}\right) dr_1 dr_2 dr_3 dr_4 dr_5. \tag{4.48}$$

**Three-Body Tree-Level Decay with Two Massless $t$-Channel Propagators**

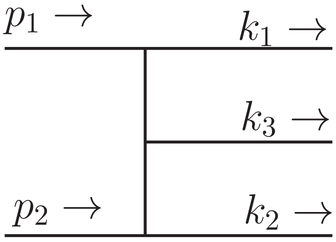

Figure 4.5: Layout of notation for a three body decay.

For the case under consideration, the layout is as given in figure 4.5, with the assumption that $p_1^2 = p_2^2 = 0$. Then $\sqrt{\hat{s}} = E_{CM} = 2E_1^{CM} = 2E_2^{CM}$; $\vec{p}_1^{CM} = -\vec{p}_2^{CM}$, $\left|\vec{p}_1^{CM}\right| = \left|\vec{p}_2^{CM}\right|$. The simple mappings $x_A = r_1$ and $x_B = r_2$ can be used. This allows us to assign $p = \hat{p}_A + \hat{p}_B = x_A p_A + x_B p_B$. The goal is then to find an expression for $dx_A dx_B d\phi_3$. Boosting $p$ to the centre-of-mass frame gives $p \rightarrow p_{CM}$, and a three-body decay can then be performed as described above:

$$\begin{aligned}
E_1^{CM} &= E_{1,min}^{CM} + \left(E_{1,max}^{CM} - E_{1,min}^{CM}\right) r_1 \\
E_{1,min}^{CM} &= M_1, \qquad E_{1,max}^{CM} = \frac{\hat{s} + M_1^2 - \left(M_2 + M_3\right)^2}{\sqrt{\hat{s}}} \\
\phi_1^{CM} &= 2\pi r_3.
\end{aligned} \tag{4.49}$$

The kinematics described in the previous discussion of the general three-body decay lead to

$$\begin{aligned}\left|\vec{k}_1^{CM}\right| &= \sqrt{\left(E_1^{CM}\right)^2 - M_1^2} \\ s_{23} &= E_{CM}^2 + M_1^2 - 2E_{CM}E_1^{CM} = \left(E_{23}^{CM}\right)^2 \\ \left|\vec{k}_2^{CM23}\right| = \left|\vec{k}_3^{CM23}\right| &= \frac{\lambda^{\frac{1}{2}}\left(s_{23}, M_2^2, M_3^2\right)}{2E_{23}^{CM23}}.\end{aligned} \tag{4.50}$$

To define angles in the centre-of-mass frame of particles 2 and 3 ($CM_{23}$), it is necessary to boost $p_2$ to $CM_{23}$ to define the $z$-axis. In this frame, it is then possible to generate $\cos\theta$, using the mapping defined in eq. (4.34) for a massless $t$-channel propagator:

$$\begin{aligned}\cos\theta_2^{CM23} &= a_2 - y_2 \\ y_2 &= \left(\left(1-n\right)x_2\right)^{\frac{1}{1-n}} \\ x_2 &= \frac{y_2^{1-n}}{1-n} = x_{2,min} + \left(x_{2,max} - x_{2,min}\right) r_4\end{aligned} \tag{4.51}$$

giving

$$\begin{aligned}d\cos\theta_2^{CM23} &= -dy_2 = -y_2^n\left(x_{2,max} - x_{2,min}\right) dr_4 \\ \phi_2^{CM23} &= 2\pi r_5.\end{aligned} \tag{4.52}$$

Now that the required angles are assigned, $\vec{k}_2^{CM23}$ can be constructed by rotating $\vec{p}_2^{CM23}$ by $(\cos\theta_2^{CM23}, \phi_2^{CM23})$ and finally boosting it back to the centre-of-mass frame.

### 4.3.3 Mappings used in gg2VV

The mappings used in the multi-channel implementation for the semi-leptonic Higgs decays in gg2VV are described here in detail, making use of the components given in the previous section. It is important to emphasise that in many cases there are in fact two (sequential) mappings of the same phase space variables; the first to deal with kinematic structures that may be difficult to integrate (not required in every case), and the second to map between the phase space variables (momenta and angles) to the random numbers; this second mapping must always be present.

### Higgs Resonance Decaying to Two Massive Vector Bosons

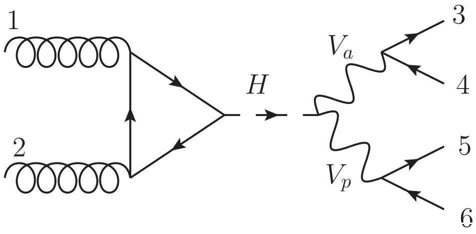

Figure 4.6: Feynman diagram showing layout of notation for the phase space mapping used for the signal process with a resonant Higgs in `gg2VV`.

The relevant components are the 2 → 2 with resonance phase space (eq. (4.40)) with two Breit-Wigner mappings (eq. (4.22)) and two body decays (eq. (4.17), one for each vector boson). Care must be taken with the integration limits: the Higgs boson will have a virtuality close to 125 GeV and so cannot produce two resonant W or Z bosons. Hence two mappings are needed, one in which say $V_a$ (the notation and labelling is shown in figure 4.6) is assigned its variables first and therefore will be close to on-shell, while $V_p$ receives its energy from the remaining parton centre-of-mass energy and will be far off-shell, and a second mapping where this is switched so that $V_p$ is in the on-shell region.

The ten random numbers then correspond to:

$$\begin{aligned}&(r_1, r_2, r_3, r_4, r_5, r_6, r_7, r_8, r_9, r_{10}) \rightarrow \\ &\left(\hat{s}, y, q_{34}^2, q_{56}^2, \cos\theta_a, \phi_a, \cos\theta_3, \phi_3, \cos\theta_5, \phi_5\right)\end{aligned} \tag{4.53}$$

where $\theta_a$ and $\phi_a$ are the polar and azimuthal angles between the incoming parton and $V_a$ in the centre-of-mass frame, $\theta_3$ and $\phi_3$ are the angles between outgoing parton 3 and its parent vector boson, and $\theta_5$ and $\phi_5$ similarly for outgoing parton 5. $\hat{s}$ and $y$ are mapped as in eq. (4.40).The two $q^2$ variables are mapped by eqs. (4.22) and (4.24), and the angles by eq. (4.18). In total, this gives:

$$\begin{aligned}\int dx_a dx_b d\phi = \int_0^1 dr_1 \cdots dr_{10}\ \frac{1}{s}\ln\tau \frac{\left(\hat{s}-M_H^2\right)^2+\left(M_H\Gamma_H\right)^2}{M_H\Gamma_H}\left(z_{\hat{s},H,max}-z_{\hat{s},H,min}\right)\\ \frac{\left(q_{34}^2-M_V^2\right)^2+\left(M_V\Gamma_V\right)^2}{M_V\Gamma_V}\left(z_{q_{34}^2,V,max}-z_{q_{34}^2,V,min}\right)\\ \frac{\left(q_{56}^2-M_V^2\right)^2+\left(M_V\Gamma_V\right)^2}{M_V\Gamma_V}\left(z_{q_{56}^2,V,max}-z_{q_{56}^2,V,min}\right)\\ \left(\frac{1}{32\pi^2}\right)^3 (4\pi)^3\ \lambda^{\frac{1}{2}}\left(1,\frac{q_{34}^2}{\hat{s}},\frac{q_{56}^2}{\hat{s}}\right)\end{aligned} \tag{4.54}$$

where, by eq. (4.22),

$$z_{q^2,i,max/min} = \arctan\frac{\left(q_{max/min}^2-M_i^2\right)}{M_i\Gamma_i}. \tag{4.55}$$

Eqn. (4.54) describes the mapping with the $V_a$ vector boson assigned first (and therefore having a mass close to $M_V$); the mapping with $V_p$ will then be identical but with $q_{34}^2$ and $q_{56}^2$ swapped in eq. (4.54) and eq. (4.53).

### Continuum Production of Two Massive Vector Bosons

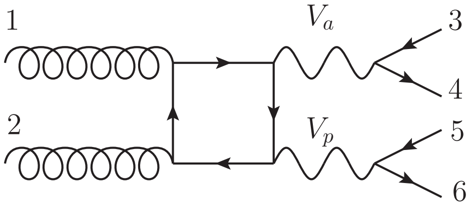

Figure 4.7: Feynman diagram showing layout of notation for the phase space mapping used for the continuum background process with two massive vector bosons in `gg2VV`.

This mapping is similar to the previous Higgs resonance mapping, except with simpler mappings for the initial state variables (eq. (4.35)) and one less Breit-Wigner mapping. The random numbers correspond to (with simply eq. (4.35) for the first two variables, and everything else as above):

$$\begin{aligned}&(r_1, r_2, r_3, r_4, r_5, r_6, r_7, r_8, r_9, r_{10}) \to \\ &\left(x_1, x_2, q_{34}^2, q_{56}^2, \cos\theta_a, \phi_a, \cos\theta_3, \phi_3, \cos\theta_5, \phi_5\right),\end{aligned} \tag{4.56}$$

where $\theta_a$ and $\phi_a$ refer to the angle between incoming gluon 1 and $V_a$ in the centre-of-mass frame. In total, this gives:

$$\begin{aligned}\int dx_a dx_b d\phi = \int_0^1 dr_1 \cdots dr_{10} \; & \frac{\left(q_{34}^2 - M_V^2\right)^2 + (M_V\Gamma_V)^2}{M_V\Gamma_V}(z_{q_{34}^2,V,max} - z_{q_{34}^2,V,min}) \\ & \frac{\left(q_{56}^2 - M_V^2\right)^2 + (M_V\Gamma_V)^2}{M_V\Gamma_V}(z_{q_{56}^2,V,max} - z_{q_{56}^2,V,min}) \\ & \left(\frac{1}{32\pi^2}\right)^3 (4\pi)^3 \, \lambda^{\frac{1}{2}}\left(1, \frac{q_{34}^2}{\hat{s}}, \frac{q_{56}^2}{\hat{s}}\right).\end{aligned} \tag{4.57}$$

Note that the limits are again asymmetric, as once the first vector boson virtuality is assigned (say $q_{34}^2$) it reduces the available energy left for the second, given by $\left(q_{56,max}^2 = \left(E_{CM} - \sqrt{q_{34}^2}\right)^2\right)$. In most cases, the two vector bosons are on-shell so this does not have an effect on the final result. However, to take account for situations where cuts might be asymmetric, again a duplicate mapping with $q_{34}^2$ and $q_{56}^2$ reversed should be included.

### Continuum Production of One Z-Boson and One Photon

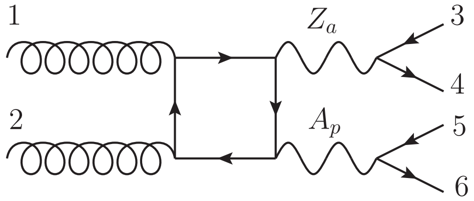

Figure 4.8: Feynman diagram showing layout of notation for the phase space mapping used for the continuum background process with one Z boson and one photon in `gg2VV`.

Again, this mapping uses many components of the previous, but one of the Breit-Wigner mappings is replaced by the massless $s$-channel propagator mapping, eq. (4.27).

The random numbers correspond to:

$$
\begin{aligned}
&(r_1, r_2, r_3, r_4, r_5, r_6, r_7, r_8, r_9, r_{10}) \rightarrow \\
&\left(x_1, x_2, q_{34}^2, q_{56}^2, \cos\theta_a, \phi_a, \cos\theta_3, \phi_3, \cos\theta_5, \phi_5\right)
\end{aligned}
\tag{4.58}
$$

where the only difference from the previous case is that $q_{56}^2$ is mapped to $r_4$ using eqs. (4.27) and (4.28).

The full mapping is:

$$
\begin{aligned}
\int dx_a dx_b d\phi = \int_0^1 dr_1 \cdots dr_{10} \; & \frac{\left(q_{34}^2 - M_V^2\right)^2 + (M_V \Gamma_V)^2}{M_V \Gamma_V} (z_{q_{34}^2,V,max} - z_{q_{34}^2,V,min}) \\
\left(q_{56}^2\right)^n (x_{max} - x_{min}) & \left(\frac{1}{32\pi^2}\right)^3 (4\pi)^3 \, \lambda^{\frac{1}{2}}\left(1, \frac{q_{34}^2}{\hat{s}}, \frac{q_{56}^2}{\hat{s}}\right)
\end{aligned}
\tag{4.59}
$$

where

$$
x_{max/min} = \frac{(q_{34,max/min}^2)^{1-n}}{1-n}. \tag{4.60}
$$

Again, a duplicate mapping is requiring to account for the leg 56 being the Z boson and 34 the photon, swapping $q_{34}^2$ and $q_{56}^2$ in the above equation.

### Continuum Production of Two Photons

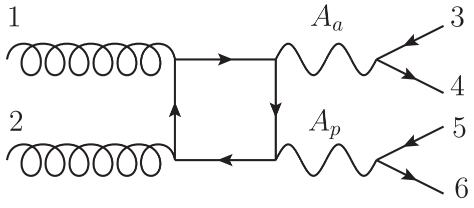

Figure 4.9: Feynman diagram showing layout of notation for the phase space mapping used for the continuum background process with two photons in `gg2VV`.

The mapping is again similar to the previous section but with the second Breit-Wigner mapping replaced also by the massless $s$-channel propagator mapping. The random numbers correspond as before (with both $q^2$ variables now mapped by eqs. (4.27) and (4.28)) to:

$$\begin{aligned}&(r_1, r_2, r_3, r_4, r_5, r_6, r_7, r_8, r_9, r_{10}) \rightarrow \\ &\Big(x_1, x_2, q_{34}^2, q_{56}^2, \cos\theta_a, \phi_a, \cos\theta_3, \phi_3, \cos\theta_5, \phi_5\Big)\end{aligned} \tag{4.61}$$

The mapping is:

$$\begin{aligned}&\int dx_a dx_b d\phi = \int_0^1 dr_1 \cdots dr_{10} \, \Big(q_{34}^2\Big)^n (x_{34,max} - x_{34,min}) \Big(q_{56}^2\Big)^n (x_{56,max} - x_{56,min}) \\ &\left(\frac{1}{32\pi^2}\right)^3 (4\pi)^3 \, \lambda^{\frac{1}{2}} \left(1, \frac{q_{34}^2}{\hat{s}}, \frac{q_{56}^2}{\hat{s}}\right)\end{aligned} \tag{4.62}$$

### Tree-Level Production of Two Quarks and One Vector Boson (Massless *s*-Channel and Massless *t*-Channel Propagators)

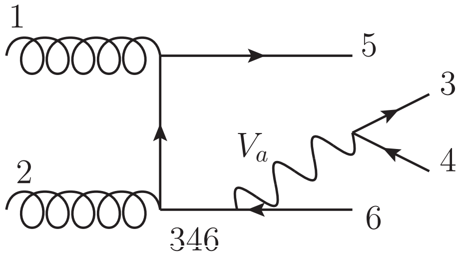

Figure 4.10: Feynman diagram showing layout of notation for the phase space mapping used for the tree-level background process with one massless *s*-channel propagator and one massless *t*-channel propagator in `gg2VV`.

Here, the $2 \rightarrow 2$ with massless *t*-channel propagator phase space, described above, is used, where one of the outgoing legs of the $2 \rightarrow 2$ decay becomes a massless *s*-channel propagator and radiates an additional Breit-Wigner resonance and two-body decay. This mapping in fact has 4 permutations: firstly, as before, the massive vector boson can be radiated off either leg, and since the integration limits are asymmetric each mapping should be repeated with the order of assignation of $q_{34}^2$ and $q_{56}^2$ reversed.

The random number assignation is

$$\begin{aligned}&(r_1, r_2, r_3, r_4, r_5, r_6, r_7, r_8, r_9, r_{10}) \rightarrow \\ &\Big(x_a, x_b, q_{34}^2, s_{346}, \cos\theta_3, \phi_3, \cos\theta_{34}, \phi_{34}, \cos\theta_5, \phi_5\Big)\end{aligned} \tag{4.63}$$

where the $q_{34}^2$ mappings are those for a Breit-Wigner resonance, eqs. (4.22) and (4.24) and the $s_{346}$ mappings those for the massless $s$-channel propagator, eqs. (4.27) and (4.28). The mapping for $\cos\theta_5$ (between incoming particle 1 and outgoing particle 5) is no longer the simple mapping from eq. (4.18) (still used for $\phi_5$ and the remaining angles), but the mapping for a massless $t$-channel propagator of eq. (4.34). The full mapping is then:

$$\begin{aligned}\int dx_a dx_b d\phi = \int_0^1 dr_1 \cdots dr_{10} & \left(\left(q_{34}^2 - M_V^2\right)^2 + \left(M_V \Gamma_V\right)^2\right)\left(z_{q_{34}^2,V,max} - z_{q_{34}^2,V,min}\right) \\ & \left(s_{346}\right)^n \left(x_{346,max} - x_{346,min}\right)\frac{1}{32\pi^2}\,\lambda^{\frac{1}{2}}\left(1, 0, \frac{s_{346}}{\hat{s}}\right) \\ & \left(1 - \cos\theta\right)^n \left(c_{max} - c_{min}\right)\cdot 2\pi\frac{1}{32\pi^2}\,\lambda^{\frac{1}{2}}\left(1, \frac{q_{34}^2}{s_{346}}, 0\right)\left(4\pi\right)^2\frac{1}{32\pi^2},\end{aligned} \tag{4.64}$$

where $c_{max/min}$ are given by $x_{max/min}$ in eq. (4.42).

### Three-Body Decay: Production of Two Quarks and One Massive Vector Boson

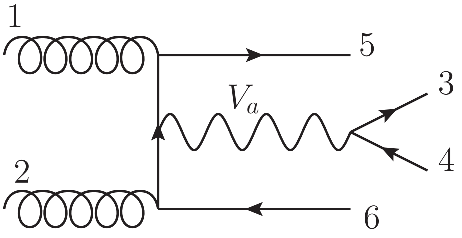

Figure 4.11: Feynman diagram showing layout of notation for the phase space mapping used for the tree-level background process with two massless $t$-channel propagators in `gg2VV`.

This mapping, with layout as in figure 4.11, uses the 2 → 3 body decay mapping given in eqs. (4.51) and (4.52), combined with a Breit-Wigner propagator and 2-body decay. Care must be taken with the frames that each factor is calculated in, as described in the text surrounding the equations. The mapping assumes that $p_1^2 = p_2^2 = M_5^2 = M_6^2 = 0$.

The random number assignment is

$$\begin{aligned}&\left(r_1, r_2, r_3, r_4, r_5, r_6, r_7, r_8, r_9, r_{10}\right) \to \\ &\left(x_a, x_b, q_{34}^2, E_5^{CM}, \cos\theta_5, \phi_5, \cos\theta_6^{CM346}, \phi_6^{CM346}, \cos\theta_3^{CM34}, \phi_3^{CM34}\right).\end{aligned} \tag{4.65}$$

$q^2_{34}$ is mapped by eq. (4.22); $E_5^{CM}$ by eq. (4.49), $\cos\theta_5$ and $\cos\theta_6$ by eq. (4.34), and the remaining angles by the usual simple angular mapping in eq. (4.18).

The full mapping is:

$$\begin{aligned}\int dx_a dx_b d\phi = \int_0^1 dr_1 \cdots dr_{10} & \left(\left(q^2_{34} - M_V^2\right)^2 + \left(M_V\Gamma_V\right)^2\right)\left(z_{q^2_{34},V,max} - z_{q^2_{34},V,min}\right) \\ & \frac{1}{16\left(2\pi\right)^5} E_5^{CM}\left(E_{max} - E_{min}\right)\left(1 - \cos\theta_5^{CM}\right)^n \left(c_{5,max} - c_{5,min}\right)\cdot 2\pi \\ & \lambda^{\frac{1}{2}}\left(1, 0, \frac{q^2_{34}}{s_{346}}\right)\left(1 - \cos\theta_6^{CM346}\right)^n \left(c_{6,max} - c_{6,min}\right)\cdot 2\pi\frac{1}{32\pi^2}4\pi\end{aligned} \tag{4.66}$$

where $E_{min} = 0$, $E_{max} = \frac{\hat{s} - M_V^2}{2\sqrt{\hat{s}}}$ and the relevant values of $c_{i,max/min}$ are derived from eq. (4.42).

### 4.3.4 Implementation of Multi-Channel Mappings in gg2VV

From a computational point of view, there are two ways in which the mappings $f_i$ for $i = 1 \cdots N$ will be used. For every phase space point, a mapping will be chosen (either sequentially or with uniform probability) as the 'main' mapping, with which the phase space variables for this point, denoted $PS$, are calculated in a new basis. However, even with this mapping chosen, the Jacobi determinants $g_j(PS)$ of every other mapping will still need to be calculated for the chosen phase space point and summed to give the overall weight for that phase space point; these give the total $g\left(PS\right)$ factor in the change of variables, but it is the additional Jacobi determinant from the main mapping that will compensate the peak in the matrix element.

The code implementation consists of classes for the different kinematic components (e.g. resonance, two body decay) and a class for each mapping, containing a 'main mapping' method to take a vector of random numbers (and any other values that one might wish to reuse in a different circumstance, and should therefore not be constants: e.g. the mass and width of a vector boson, meaning that some of the same mappings can be used for $WW/ZZ$ diagrams) and assign values in the chosen phase space basis, and a 'jacobi' method to calculate the Jacobi determinant for that mapping using the phase space variables assigned by the main mapping. A further method sums the inverse

Jacobi determinants and assigns the total weight $g(PS)$ to every point. In the code used throughout this thesis, `gg2VV` (written in C++), there is also an "enum" for each mapping, allowing the appropriate mappings to be chosen automatically depending on the amplitude contributions that are included (e.g. signal-only, background-only).

Note that the different mappings cover overlapping regions of phase space - any mapping can be performed at any point, although it will automatically receive a large (small) weighting if it is more (less) important. The different error contributions are therefore not independent, hence are summed linearly rather than in quadrature.

An immediate advantage of the multi-channel approach is that the code is easily generalisable, e.g. to cases with an additional heavy Higgs-like boson: the same mapping used for the SM Higgs boson can be recycled, with the SM mass and width replaced with the desired values. It will be seen in Chapter 7 how this can be neatly applied in the Higgs singlet extension of the Standard Model, for example.

Improved error convergence on subsequent iterations can in principle be achieved with adaptive $\alpha_i$ weights [55]. Since the error is dependant on the variance, which is calculated from the square of the integrand, $\left(h\left(PS\right)g_i\left(PS\right)\right)^2$, the authors suggest minimising

$$W = \left\langle \left(h\left(PS\right)g_i\left(PS\right)\right)^2 \right\rangle \tag{4.67}$$

with respect to the weights, and finding an optimal set of weights $\bar{\alpha}$ such that the derivative

$$W_i' = -\frac{1}{2}\frac{\partial W}{\partial \alpha_i} = \left\langle \frac{h^2(PS)g^3(PS)}{g_i(PS)} \right\rangle \tag{4.68}$$

is independent of the channel $i$, which they argue is the condition for a minimum.

For the particular case of stratified sampling, a type of Monte Carlo integration where the phase space is divided into bins of a predetermined size and a predetermined number of points sampled in each bin, the authors have shown that the optimal set $\bar{\alpha}$ is achieved for

$$W_i'(\alpha) = c\,\bar{\alpha}^{-2} \tag{4.69}$$

where $c$ is a constant with respect to the index i, the channel being considered. They then propose that the optimal set will therefore be immediately reached by setting

$$\alpha_{i,new} = \alpha_{i,old}\sqrt{W_i'}. \tag{4.70}$$

This justification is based on the special case of stratified sampling, and no more general result is given. Stratified sampling assumes that each channel is separate and independent, i.e. that each channel covers a separate phase space region and so has a constant finite probability density in the region and zero probability density outside. This is not the case in the situations considered here - the entire reason that multi-channel mappings are necessary is that the importance of different channels overlaps across the entire phase space. Nonetheless, the authors have confirmed in private correspondence that this general procedure works well in practice for more general situations than those described, in particular for particle physics applications.

Since the procedure is not exact, an implementation requires a measure of the success of the weight adaptation, and ideally several iterations will be performed and the best set of weights chosen. The authors argue that, in special cases, the error is minimised when all channels contribute equally to the variance, so the quantity

$$D = \max_{i,j}\left|W_i'(\alpha) - W_j'(\alpha)\right| \tag{4.71}$$

is calculated for each iteration and the set of weights that minimise $D$ chosen.

This method was implemented and tested in gg2VV, but the gain was found to be minimal, particularly in combination with the competing adaptation of the importance sampling weights used to optimise the individual channels, and so it was discarded, and uniform $\alpha_i$ weights are used.

## 4.4 Event Generation

In many cases, the desired output of a Monte Carlo integrator is not only a numerical answer for a cross section or a set of differential distributions, but a set of simulated events such as might be expected in an analysis of real detector data - a list of final state particles and their measurable properties, in particular their energy and momenta.

Code designed to perform Monte Carlo integration is easily adapted to output events, since evaluating the integral at a phase space point effectively means generating values for all the integration variables, i.e all external momenta and the initial state momentum fractions, and can be considered an event.

Events generated in this way can be either weighted or unweighted. If events are weighted, there can be as many events generated in unlikely regions of the phase space as in likely regions, but with a lower weight (reflecting the probability) attached. Events will therefore contribute more or less to the computation of observables depending on their probability of occurring. Typically, experimentalists wish to compare *unweighted* events to data, where every event has equal weighting and so the events are distributed as in nature. The usual strategy for unweighting events, by default generated weighted in a Monte Carlo integrator like gg2VV, is to find the maximum weight in the total sample, and keep or reject each simulated event with a probability of $P = \frac{f_{event}}{f_{max}}$ where $f$ is the integrand $\frac{d\sigma}{dr}$ evaluated at that point, here referred to as the weight. In practice this means generating a random number $r$ between 0 and 1 and keeping the event if $r < P$.[7]

An advantage of generating a set of events in a standard format is that they can be easily interfaced with other code, for example samples created in a parton-level generator, designed to simulate the hard process only, can be showered and hadronised using different software.

## 4.5 Interference

The squared sum of Feynman diagrams used to calculated the matrix element requires some clarification. Physicists typically talk of a ‘signal process’, referring to the process of interest containing a particular resonance or feature of interest and the ‘background processes’ which are non-signal processes that are formally indistinguishable from the signal. However, signal and background in isolation are not observables; although it may be possible to make inferences about the most likely intermediate state based on kinematic distributions of observables, the quantum principle that any and all paths

---

[7] This strategy is a general technique for generating distributions corresponding to an arbitrary probability distribution.

between a given and initial final state occur with a finite probability applies. If only subsets of all available paths are considered, there is no guarantee of unitarity or gauge invariance.

Backgrounds can be further divided into reducible backgrounds, that have the same initial and final state at detector level but typically look very different in their output, for example they may have distinguishing kinematic features like back-to-back jets, and irreducible backgrounds, i.e. those that look very similar to the signal process. All types of backgrounds must be formally included, but with particular selection cuts reducible backgrounds can be rendered less important. Further backgrounds come from 'fakes' - events that in fact come from a different process, and would not formally be included in a theoretical prediction, but are incorrectly identified by tracking and identification procedures, for example due to a particle being deposited in a detector blindspot and therefore registered as contributing missing energy and transverse momentum to the process, incorrectly indicating an invisible particle such as a neutrino.

Typically the signal and background are discussed separately. However, it is not correct to simply take the sum of these to calculate the observable number of events; since the quantities under consideration are quantum fields and coherent processes, it is important to consider a third type of contribution, the interference term. Formally, denoting the matrix element as $\mathcal{M}$,

$$\sigma \sim |\mathcal{M}|^2 = \left|\mathcal{M}_{sig} + \mathcal{M}_{bg}\right|^2 = \left|\mathcal{M}_{sig}\right|^2 + \left|\mathcal{M}_{bg}\right|^2 + 2\mathrm{Re}(\mathcal{M}^*_{sig}\mathcal{M}_{bg}) \tag{4.72}$$

and it is the last term which is described as interference.

It should be emphasised that although the quantity in eq. (4.72) is gauge independent, as mentioned above, this is not guaranteed for individual components.[8] Gauge dependence in automatically generated amplitudes for unstable particle production and decay is a long-standing unresolved problem and not specific to interference calculations. Here, the fixed-width prescription for unstable particle propagators is adopted, because no phenomenologically relevant example is known where it leads to significant deviations compared to a gauge independent treatment of the amplitudes. This is generally true, including for interference calculations.

---

[8] All results calculated in this thesis are calculated in the Feynman gauge.

Until the last decade or so, in many approximations this final interference term was considered only as a correction,[9] and if mentioned at all was quoted as a source of error. However, in the processes considered at the LHC, other large sources of error, notably PDF and scale errors, have gradually reduced to the percent level, meaning that treating any effects that can be of similar or larger order more carefully is merited. Interference effects in many cases are now known to be at the level of a 10% or higher correction to the pure signal, and can be reduced or enhanced with selection cuts, therefore a more careful study is required.

Interference effects are often related to (although not confined to) off-shell effects. Typically, all intermediate resonances in a process are approximated as being 'on-shell' since the Breit-Wigner resonance contribution to the squared amplitude shown in eq. (4.3) is dramatically enhanced when the centre-of-mass energy is close to the mass, tending to overshadow all other effects. However, it is increasingly recognised that 'off-shell' effects must be properly treated. In certain cases, other effects give enhancements in the differential distribution away from the on-shell region. It is when these enhancements overlap with important regions from other contributions in the sum that significant interference can be observed.

A good example of the relevance of off-shell effects is the importance of the weak boson decay channels of the light Higgs boson. The presence of these channels at all is an off-shell effect, since for $M_H < 2M_V$, which 125 GeV certainly is, one of the vector bosons to which the Higgs decays must be far off-shell. The narrow-width approximation, which replaces the full resonance propagator with $\frac{\pi}{m\Gamma}\delta(q^2 - M^2)$ in the limit that $M \gg \Gamma$, is naively expected to be excellent for a low mass (and therefore small width) Higgs boson, since the error is expected to be $O(\frac{\Gamma_H}{M_H})$. However, this error estimate assumes that the strongest centre-of-mass energy dependence comes from the resonance; in the case of the Higgs boson decaying to two vector bosons the matrix element is dramatically enhanced when the second vector boson can go on-shell, above $q^2 \sim (2M_V)^2$. At this point, the decay matrix element squared has an energy scale dependence $\sim (q^2)^2$, and so the narrow width approximation is no longer appropriate [6]. There is a distinct bump in the tail of the distribution at $\sim 2M_V$, and a further bump in the gluon fusion case at $2M_t$ due

---

[9] With a few notable exceptions, for example destructive interference arising from the Higgs-mediated process in longitudinal $WW$ scattering is crucial to unitarise the cross section.

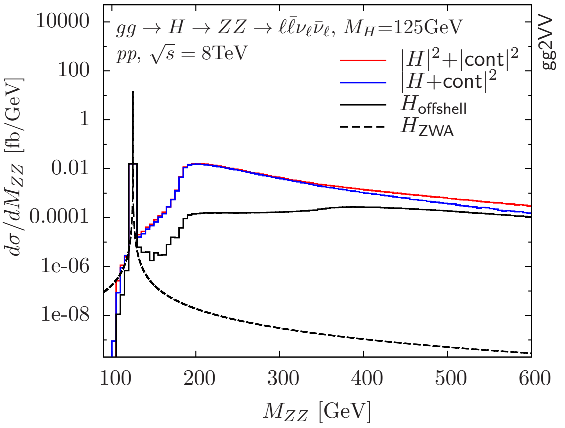

Figure 4.12: Invariant mass distribution comparing results with and without the narrow-width approximation, and with and without interference (taken from [6]).

to two top quarks in the gluon-fusion-to-Higgs quark loop being allowed to be on-shell. Without cuts excluding these off-shell regions, the inclusion of these effects enhances the signal by about 10%. These effects are clearly visible in figure 4.12, reproduced from ref. [6].

In recent times, the different off-shell dependence of cross sections has been exploited in a very neat way to allow a much stronger limit to be set on the Higgs boson width than was ever expected at this early stage of the LHC programme. It is arguable [56] whether this limit is robust against new physics effects in loops in gluon fusion,[10] but it is nonetheless promising. The idea is that while the on-shell cross section is inversely proportional to the total width and so is sensitive only to ratios of couplings (and therefore cannot distinguish between the SM case and a case where couplings are uniformly scaled by an identical factor), the off-shell region has no width dependence. Comparison of on- and off-shell event rates then allows a limit to be extracted on the allowed scaling of the SM Higgs width [5]. ATLAS [3] and CMS [4] have performed analyses bases on this method and published 95% confidence upper limits on the Higgs width of 17.4 MeV and 22.7 MeV respectively, about 5 times the SM value.

Another use of interference to limit the Higgs width has been described in references [57] and [58], where the interference effects between the very clean $gg \to H \to \gamma\gamma$ process and the $gg \to \gamma\gamma$ background, combined with the smearing effects of the detector, cause the measured value of the mass peak of the Higgs boson to shift from its theoretical

---

[10] So far, this method has been applied to $gg \to H \to ZZ$.

prediction without interference (or its measured value in the $gg \to H \to ZZ$ channel, which is not affected by on-resonance interference) by a potentially measurable amount. However with current precision and luminosities, this method is not precise enough to compete with the on-shell/off-shell comparison method.

In addition to the references cited above, refs. [59, 60] gave an early study of the interference between the Higgs signal and continuum background for $gg \to ZZ$, which is followed up in ref. [61]. Reference [62] considers this process in vector boson fusion, i.e. with two extra final state jets. Reference [63] considers the Higgs production in $gg \to WW$, ref. [64] studies the same process beyond leading order and ref. [65] gives a study for all fully leptonic final states, including interference between the $gg \to H \to WW$ and $gg \to H \to WW$ signals in the case with a same flavour $2\ell 2\nu$ final state. Further papers studying interference in the di-photon process to leading order and beyond are refs. [66–68]. Studies of interference between SM and BSM processes have also been carried out, for example in the SM+Higgs singlet model in refs. [7, 69, 70].

The papers cited above consider a single initial state of $gg$ or $q\bar{q}$, however the distinguishable initial state is in fact $pp$ rather than $gg$; beyond leading order, there is then the possibility of interference between different Higgs production mechanisms that give the same final state, for example the production of a Higgs boson with two jets arising from NLO gluon fusion or LO vector boson fusion. It has been pointed out [71] that this interference is not necessarily negligible. For Run I of the LHC, gluon fusion was by far the dominant production mechanism, but VBF will become more important in Run II and this may merit further study. The studies in this thesis are not affected by this, since only the leading order gluon fusion case is considered.

# Chapter 5

# gg → VV: A Parton-Level Integrator and Event Generator

## 5.1 The Code

gg2VV [6] is a publicly available program to compute cross sections and generate parton-level events at leading order for the gluon fusion Higgs decays via weak bosons. Previous versions of the code covered all fully leptonic Standard Model final states. My work has been to add the SM semi-leptonic decays and the BSM Higgs singlet model with the main fully leptonic decays; both additions are publicly available as new versions, separate to the main development line, gg2VV_EWS [7] and gg2VV-3.1.2_semilept [8] respectively. I have also implemented multi-channel mappings, as discussed in Chapter 4, in the phase space integration part of the code, which is a significant redesign of how the phase space integration is performed. This was necessary in order to accommodate the semi-leptonic decays, due to the large number of different kinematic structures, and was useful in the implementation of the BSM processes since it is easily extendable to additional Higgs-like resonances.

The code is structured as follows:

- The main function begins by checking for external input of random number seed, initialised phase space grid, or initialised event file. Monte Carlo integrator and parallelisation objects (discussed further in section 5.1.1) are instantiated and initialised, and all relevant parameters are printed out for reference.

- The phase space integration is set up by selecting the number of kinematic channels based on the process and requested amplitude contributions, and Monte Carlo objects created for each section/channel. The number of integrands to be kept track of is selected and the integrator objects instantiated (integrands include the main integrand at the chosen PDF and renormalisation scale, and the integrands at the scales varied by a specified factor, usually two).
- At this point, the flow diverges depending on whether event generation is chosen or not. If no event generation is required, an initial estimate of efficiency is performed, and if necessary initial adaptation runs will be carried out in order to produce a sample with the desired number of shots passing the selection cuts and consistency tests. A single successful 'shot' consists of performing the phase space mapping to get a valid phase space configuration, testing that this passes consistency checks like conservation of 4-momentum and energy, and checking that it passes the selection cuts. The amplitude is then calculated and combined with the phase space weight, PDF probability, and additional factors excluded in the amplitude calculation like $\alpha_s$ (set to 1 initially) raised to the relevant power, and the conversion factor from $\text{GeV}^{-2}$ to fb.

  The requested number of iterations are then run, with grid adaptation and Monte Carlo weight adaptation (i.e related to importance sampling weights as in section 4.3, not multi-channel weight as in section 4.3.1) after each section. Note that in some cases with a large number of multi-channel sections, there may be some tension in the importance sampling weight adaptation, especially if it is performed based on early runs with low efficiency and high error. For this reason, it is recommended that the number of initial shots is not too low (say $\gtrsim 10^5$).
- If event generation is selected, the code runs several shorter cross section type runs in order to adapt the grid, and then runs in event generation mode; the number of events to be generated in each section[1] is estimated and the phase space points randomly generated; the produced phase space point is then passed to an event generation module that undoes the approximation of massless leptons for $\mu$ and $\tau$ and prints the output in a standardised form [23]. By default events are weighted,

---

[1] In this context a section is defined as a set of phase space points which will be generated according to a particular main multi-channel mapping.

if necessary they can then be unweighted; the code keeps track of the maximum weight and maximum cross section to perform this as described in section 4.4.

- On the final iteration in both event generation and integrated cross section mode, all data is binned into histograms as requested and new adapted grid files are printed for use in future runs.

### 5.1.1 External Packages

During runtime, gg2VV makes use of several external packages:

- LHAPDF [72] is the standard PDF library format and PDF reader used by many HEP event generators; gg2VV calls functions for the value of the PDF at a particular value of the parton momentum fraction for each colliding beam and the specified value of the factorisation scale $\mu_f$. It also requests the value of the strong coupling constant at the chosen scale. PDF errors, where available, can be requested.
- LoopTools [73] performs the evaluation of the one-loop integrals in the amplitude expressions; it was designed in tandem with FormCalc (described in the same reference), the code used to generate the amplitude expressions used in gg2VV.
- OmniORB [74] is a distributed worker system based on CORBA,[2] used in the parallelisation of the code. Each section of the phase space integration must select phase space points and evaluate the amplitude $N$ times (typically $N \sim 10^6$) with $m$ worker nodes. The "omnicomp" module which takes advantage of omniORB distributes roughly $N/m$ points to each worker node in order to speed up the runtime. Differing worker (CPU) speeds are taken into account and error treatment is handled appropriately. At present the omnicomp module is not able to recombine events generated by different workers so the parallelisation is only suitable for cross section calculations, although a script is supplied that runs a separate event generation process for each worker and combines the returned files. Another disadvantage of this type of parallelisation is that if a single worker crashes, the calculation must be killed and restarted.

---

[2] A commonly used IDL interface for distributed broker/request management.

### 5.1.2 Multi-channel Mappings Implementation

The multi-channel implementation is similar in overall structure to the older ‘phase space’ class which divided up the phase space into separate integration regions. There is a multi-channel namespace, with a class for each different mapping. Each mapping class has a ‘mainMapping’ method that performs the phase space transformation and assigns the required phase space variables according to the mapping, and also a Jacobi function that returns the Jacobi determinant (taking an already-mapped phase space point as input, and returning the Jacobi determinant that would have been calculated if this mapping had been the main mapping). Two further methods in the namespace deal with assigning the relevant mappings for each process and amplitude combination, and calling the relevant “mainMapping” and “Jacobi” functions to assign all phase space variables, including the overall weight.

Each channel is designed with a particular type of Feynman diagram in mind, in order to compensate that diagram’s difficult or singular regions. Switches then allow the selection of all continuum background diagram channels if one wishes to include the continuum background and so on. Note that many of the diagrams in fact compensate structures in the *squared* amplitude rather than the amplitude itself; this means that if one chooses to separate the interference contribution and calculate this on its own[3] the mappings may not be ideal, however in practice it is found that they still work well.

Each channel has been tested separately to confirm that it succeeds in compensating for the singular or strongly peaked structure for which it is designed, and also that it satisfies the known analytic result for the phase space volume. With the amplitude and PDF contributions simply set to one, a channel-by-channel test has been performed by comparing the analytic result to the differential distribution obtained by integrating over the phase space volume. For $n$ massless final state particles,

$$\int d\Phi_n(PS) = (2\pi)^{(4-3n)} \left(\frac{\pi}{2}\right)^{(n-1)} \frac{p^{(2n-4)}}{\Gamma(n)\Gamma(n-1)}. \tag{5.1}$$

---

[3] This is not strictly valid when event generation is desired and all results should be positive definite, which the interference contribution alone is not. However in practice, if one wishes to get high precision on interference in the cross section calculation, particularly in far off-shell regions of the phase space, separating the interference contribution proves to be the best strategy.

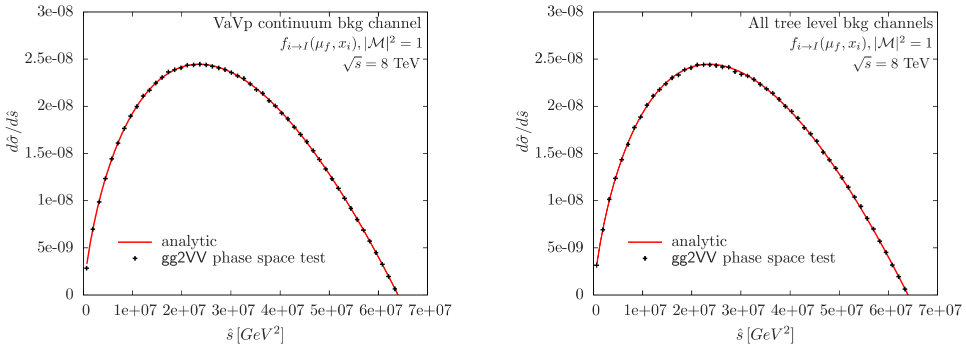

Figure 5.1: Comparison between the analytic result given in eq. (5.4) and the gg2VV calculation for phase space integration only, i.e. with the matrix element and PDF components set equal to 1. Examples are shown for a single channel (described in section 4.3.3) and for a summed group of channels.

where $p$ is the total momentum, given by the sum of the incoming momenta; then $p^2 = \hat{s}$ and for $n = 4$ this gives

$$\int d\Phi_n(PS) = \frac{\pi^{-5}2^{-11}}{12}\hat{s}^2 = c\hat{s}^2 \tag{5.2}$$

The more general cross section is given by:

$$\sigma_{tot}\left(a, b \to n)\right) = \int_0^1 dx_A \int_0^1 dx_B f_{A,a}\left(x_A, \mu_f\right) f_{B,b}\left(x_B, \mu_f\right) \frac{1}{2\hat{s}} \int d\phi_n\left(PS\right) \sum |\mathcal{M}|^2 . \tag{5.3}$$

Setting the matrix element and PDF contributions to 1, using $dx_A dx_B = \frac{1}{x_B} d\tau dx_B$ where $\tau = \frac{\hat{s}}{s} = x_A x_B$, and combining this with eq. (5.2) then gives the comparison formula for the differential cross section:

$$\frac{\partial}{\partial\tau}\sigma_{PSonly} = \frac{c}{2}\int_\tau^1 dx_b \frac{1}{x_b}\tau = \frac{c}{2}(-\log\tau)\tau. \tag{5.4}$$

Every channel implemented in gg2VV has passed this test. Sample results for the continuum box (figure 5.2, described in section 4.3.3) channel alone and for all tree-level background channels, summed as described in eq. (4.13), are given in figure 5.1.

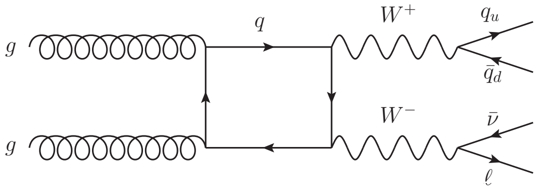

Figure 5.2: Sample Feynman diagram of the type that causes problems for numerical stability due to the Gram determinant approaching 0.

### 5.1.3 Errors and Precision

Regions of phase space where the vector bosons have very low $p_T$ suffer from singularities in the continuum diagrams of the type shown in figure 5.2. The helicity amplitude for diagrams of this type contains a term proportional to the inverse of $\det G = 2s\,(t \cdot u - s_3 s_4)$, the two-dimensional Gramm determinant, where $s_3$ and $s_4$ refer to the invariant mass of the vector bosons, and $s, t, u$ are the Mandelstam variables $s = (p_1 + p_2)^2$, $t = (p_2 + p_3)^2$and $u = (p_1 + p_3)^2$. $p_1$ and $p_2$ refer to the initial state gluons, and $p_3$ to one of the $W$ bosons. As the transverse momentum of the vector boson approaches 0, the amplitude diverges while the cross section remains finite. A more comprehensive discussion can be found in ref. [75], which uses the same LoopTools external code as gg2VV for amplitude evaluation.

In gg2VV these issues are dealt with by evaluating points within a certain range of the singularity in quadruple precision[4] and cutting out any points with $p_T(V) < 1\,\text{GeV}$; this has less than a 1% effect on the final cross section. For consistency, this cut is then generally applied (in the cut selection phase rather than inherently) to the signal cross section, especially if signal-continuum interference is to be included in results. Note that quadruple precision evaluation is significantly slower, so it is not feasible to evaluate the whole phase space in quadruple precision.

Naïvely, one might assume that since the integration is performed in sections, the error for each section should be summed in quadrature to produce an overall error estimate. However, since the weight at every phase space point contains contributions from every kinematic structure, the sections are not independent. Testing has revealed that summing in quadrature underestimates the error, and hence errors are added linearly.

---

[4] When much of the code was written this was only achievable with intel Fortran compilers; the gcc Fortran compilers now also allow quadruple precision compilation.

Cases where it is possible to isolate a contribution to the total cross section that is not positive-definite are also considered. For example, it is possible to evaluate the interference contribution only. There may be a large cancellation between positive and negative contributions to the final result from each section, and to avoid underestimating the error it is important to keep track of the variance for both types of contribution separately and combine them in quadrature, before summing the contributions from each channel linearly.

## 5.2 New Processes

The typical workflow of adding a new process is

- For a BSM Model, produce a FeynArts model file by implementing the model in Feynrules (write the Lagrangian, specify output parameters and calculate derived parameters such as widths as required). For a Standard Model process the default 'SMQCD' model in FeynArts is sufficient, so this step is unnecessary. If Feynrules is used to generate the file, the external parameter defaults need to be changed to match gg2VV; those used in the SMQCD model in FeynArts match gg2VV already.
- Using FeynArts and Formcalc [73, 76] in Mathematica, produce the amplitude code (in Fortran). FeynArts is only equipped to select contributions based on loop order rather than coupling order; in cases with a loop-induced process and a tree-level background such as the semi-leptonic processes considered in this thesis, this then means that unwanted contributions such as the tree-level diagrams with electroweak corrections must be excluded manually. The validity of this is discussed further in Chapter 6.
- Adapt the Formcalc output for compatibility with gg2VV: where there are several contributions to the interference that need to be separated, new variables need to be added to keep track of the different components (by default all are included but summed before the results are returned). The propagators for the vector bosons and Higgs boson need to be adapted to include the partial widths, and some formatting changes made to the default Fortran files for compatibility with compilers.
- Add the adapted 'squaredME' folder generated in the previous step to the gg2VV

amplitude/formcalc folder, and add a macro for the new process as a compilation option. Any switches that depend on the process will need to be extended or added as necessary, for example selection cuts optimised for a particular process, event generation options, amplitude contribution options, and additional parameters needed for a BSM process.

- If necessary, add new channels for the multi-channel integration. In many cases, it will be possible to use existing channels. In all cases, it will be necessary to specify which channels are to be included with which amplitude contributions.

For a new FeynArts model file, or one adapted from the SMQCD default (as was the case for the Higgs singlet model discussed in Chapter 7), the model file should be validated in some way, for example checking agreement with SM limits.

## 5.3 Comparison with Other Tools

The multi-channel mappings were a significant change in how gg2VV performed the phase space integration. Validation against existing tools is therefore important, and has shown good agreement. Although the point of implementing our chosen processes was that no existing tools calculated all the contributions under consideration, certain subsets of the contributions could be compared to other programs. SHERPA [77] was able to calculate the tree-level contributions considered in Chapter 6, the comparisons are shown in table 5.1. Comparisons for the loop-induced components were performed with VBFNLO and MCFM; MCFM could only calculate the fully leptonic loop-induced $WW$ decays, but the only difference in this component with the $WW$ semi-leptonic decays is a factor of 3 due to the colour contribution for the hadronically decaying boson. Note that although subsections of the calculation could be verified with different tools, no previous implementation was capable of including all types of leading-order contributions (and therefore including interference effects). Again, all comparisons showed good agreement.

These tests were performed during the initial implementation of the multi-channel method; for the results given in [8], Eleni Vryonidou of the MG5 collaboration performed a detailed comparison of our results using a custom implementation[5] of MAD-

---

[5] The public version of MADGRAPH5_aMC@NLO now allows automated calculation of loop-induced processes but this was not complete at the time.

Table 5.1: Early comparison of results for the integrated cross section of the tree-level background with SHERPA, using identical cuts and PDF (CT10nnlo.LHGrid).

| Process | SHERPA | gg2VV |
|---|---|---|
| $gg \to \bar{\ell}\nu q^{'}\bar{q}$ | 5346(11) | 5325(5) |
| $gg \to \ell\bar{\nu}q\bar{q}^{'}$ | 5332(11) | 5324(7) |
| $gg \to \ell\bar{\ell}d\bar{d}$ | 507(1) | 505(1) |
| $gg \to \ell\bar{\ell}u\bar{u}$ | 470(1) | 464(1) |

Table 5.2: Comparison of cross sections for $S = |\mathcal{M}_H|^2$, $I_{tree} = 2\text{Re}\left|\mathcal{M}_H\mathcal{M}^*_{tree}\right|$ and $I_{cont} = 2\text{Re}\left|\mathcal{M}_H\mathcal{M}^*_{cont}\right|$, calculated with gg2VV and MadGraph5_aMC@NLO for the process $gg \to H \to W^-W^+ \to \ell\bar{\nu}_\ell\, q_u\bar{q}_d$. The gg2VV results are taken from table 6.1.

| cuts | $S$ | $I_{tree}$ | $I_{cont}$ |
|---|---|---|---|
| min. (gg2VV) | 67.28(9) | -2.47(2) | -4.99(1) |
| min. (MG5) | 67.19(6) | -2.49(2) | -5.004(3) |
| LHC (gg2VV) | 1.978(6) | 0.266(4) | -2.647(6) |
| LHC (MG5) | 1.963(3) | 0.264(4) | -2.646(7) |
| bkg. (gg2VV) | 13.30(2) | -0.0054(2) | -1.052(5) |
| bkg. (MG5) | 13.30(2) | -0.0057(5) | -1.08(2) |

Graph5_aMC@NLO [78], both at the matrix element squared level for a single point and at the cross section level. No discrepancies between the two tools were found, and the results are shown in table 5.2 and table 5.3 for a single sample process. The comparisons of $S = |\mathcal{M}_H|^2$ (signal process occurring via an intermediate Higgs) and the two interferences, $I_{tree} = 2\text{Re}\left|\mathcal{M}_H\mathcal{M}^*_{tree}\right|$ and $I_{cont} = 2\text{Re}\left|\mathcal{M}_H\mathcal{M}^*_{cont}\right|$ are shown.

No tools were available to perform a direct comparison of the Higgs singlet code; however the channels used in the phase space integration were all used and validated for the semi-leptonic code, and agreement with the SM limits of the processes considered was verified.

Table 5.3: Comparison of matrix element squared calculated for two particular phase space points labelled PS1 and PS2 with gg2VV and MadGraph5_aMC@NLO for the process $gg \to \bar{\ell}\nu_\ell\bar{q}_u q_d$. Detail as in 5.2, with $I_{full} = I_{tree} + I_{cont}$

| Contribution | PS1 | PS2 |
|---|---|---|
| $S$(gg2VV) | 2.733390391490007e–21 | 3.069651925020353e–05 |
| $S$(MG5) | 2.7335747944552452e–21 | 3.0691125525738243e–05 |
| $I_{tree}$(gg2VV) | –3.235534490462558e–15 | 1.475452008046954e–06 |
| $I_{tree}$(MG5) | –3.235675020969737e–15 | 1.475167900958353e–06 |
| $I_{cont}$(gg2VV) | –1.768513287795656e–18 | 2.319939187335657e–09 |
| $I_{cont}$(MG5) | –1.765899031616023e–18 | 2.319497322110389e–09 |
| $I_{full}$ (gg2VV) | –3.237303003750353e–15 | 1.477771947234289e–06 |
| $I_{full}$ (MG5) | –3.237440920001353e–15 | 1.477487398280464e–06 |

# Chapter 6

# Interference Effects in Semi-leptonic Higgs Decays

## 6.1 The Processes

The semi-leptonic decay channels of the Higgs boson are those where the Higgs boson decays to two weak bosons, one of which decays leptonically and the other hadronically. It can be seen in figure 3.3 that these channels in fact have higher branching ratios than their fully leptonic counterparts, but the hadronic component means that these processes have a very large QCD background, and so they were not included in the Higgs discovery analyses. Nonetheless, their large rates mean that they merit further study. It has already been pointed out in the discussion of multi-channel mappings that in fact the dominant backgrounds are tree level, while the signal process is loop induced.

The following four parton-level processes are considered for single lepton and quark flavours:

$$gg \to H \to W^- W^+ \to \ell \bar{\nu}_\ell q_u \, \bar{q}_d \tag{6.1}$$

$$gg \to H \to W^+ W^- \to \bar{\ell} \nu_\ell q_d \, \bar{q}_u \tag{6.2}$$

$$gg \to H \to ZZ \to \ell \bar{\ell} q_u \, \bar{q}_u \tag{6.3}$$

$$gg \to H \to ZZ \to \ell \bar{\ell} q_d \, \bar{q}_d \tag{6.4}$$

Representative Feynman diagrams for the signal processes are shown in figure 6.1.

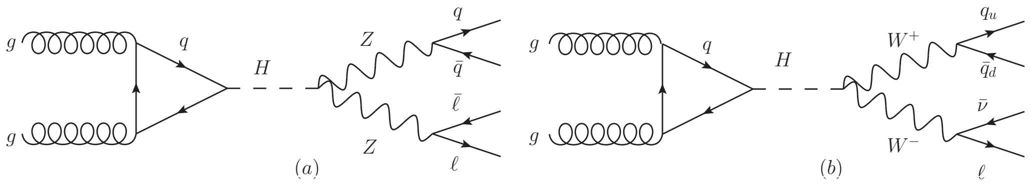

Figure 6.1: Representative Feynman diagrams for the signal processes considered: (a) $gg \to H \to ZZ \to \ell\bar{\ell}\bar{q}q$ ($q_u\bar{q}_u$ and $q_d\bar{q}_d$ final states are calculated separately) and (b) $gg \to H \to WW \to \ell\bar{\nu}_\ell\bar{q}_d q_u$ (the charge conjugated process is also calculated).

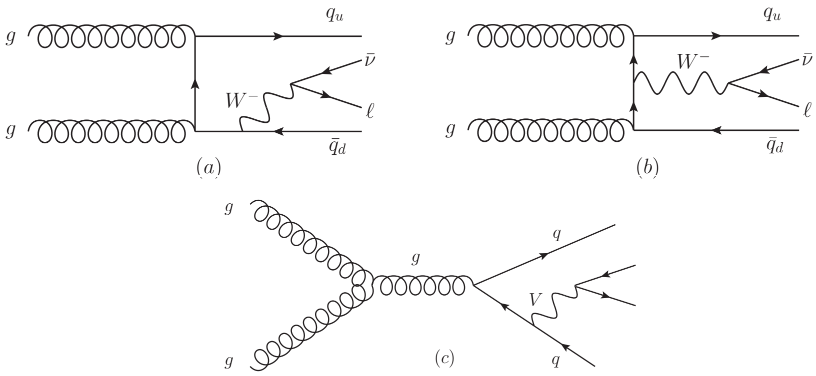

Figure 6.2: Representative tree-level diagrams that contribute to $gg \to \ell\bar{\nu}_\ell\bar{q}_u q_d$ and $gg \to \ell\bar{\ell}q\bar{q}$.

Processes (6.1) and (6.2) are related by CP symmetry and so will be identical (the selection cuts are also symmetric), so in general results are only shown for (6.2), although they have both been calculated and verified to be identical. Processes (6.3) and (6.4) differ (without cuts) by the ratio

$$\frac{(V_d^2 + A_d^2)}{(V_u^2 + A_u^2)} = \frac{(\frac{1}{2} - \frac{4}{3}\sin^2\theta_W)^2 + (\frac{1}{2})^2}{(-\frac{1}{2} + \frac{2}{3}\sin^2\theta_W)^2 + (\frac{1}{2})^2} \tag{6.5}$$

where $V_f$ and $A_f$ are the vector and axial couplings for a quark of flavour $f$. This ratio is approximately 1.28. Note that with selection cuts this will not necessarily hold in all cases, but it is useful as a guide in verifying the results of the signal process with minimal cuts (see for example tables 6.5 and 6.7).

Figures 6.1-6.4 show representative Feynman diagrams for the different components of the amplitude. This study considers interference with the leading order background diagrams with the same final states as the signal processes. These are $O(g_s^2 e^2)$ and tree

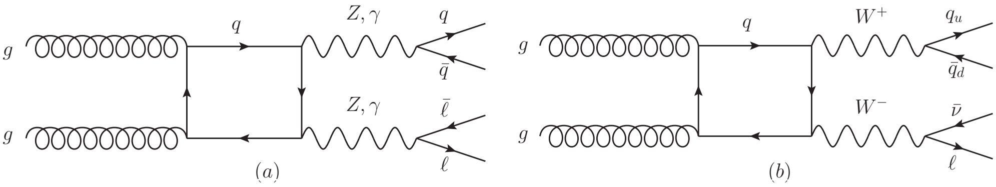

Figure 6.3: Representative continuum diagrams that interfere with the signal diagrams above.

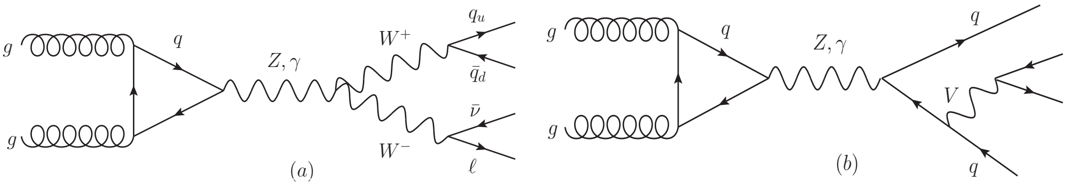

Figure 6.4: Representative triangle diagrams that formally contribute to $gg \to \ell\bar{\nu}_\ell\bar{q}_u q_d$, but do not contribute in the case of vanishing final state lepton and quark masses.

level. Since continuum interference for $gg \to VV$ is known to be large, particularly for $M_H > 2M_V$, the continuum interference diagrams (Figure 6.3) that are $O(\alpha_s^2 e^4)$ are also studied. These are of the same order as the $\mathcal{O}(e^2)$ virtual electroweak (EW) corrections to $\mathcal{M}_{tree}$. The complete set of these virtual corrections (specifically, all self-energy corrections and all diagrams with boson propagators in the loop) will not be finite and is hence not taken into account. It can be argued that these are part of the next-to-leading order (NLO) EW corrections to $I_{tree}$ and are genuinely suppressed by $\mathcal{O}(\alpha)$ relative to the included contributions, so given that $I_{tree}$ at LO yields a small (tiny) correction to $I_{loop}$ for integrated results when LHC (background suppression) cuts are applied (see section 6.2), it can be concluded that this treatment is justified. It can be similarly argued that neglecting the NLO QCD corrections to $I_{tree}$ in our calculation is justified.

Formally, the background also includes quark triangle diagrams such as those in figure 6.4, however these are identically zero for a photon and the vector coupling of the Z boson as an intermediate resonance by Furry's theorem. They have also been shown analytically to be zero for the axial component of the Z boson with massless quarks in the final state [79,80]. The arguments still apply to these semi-leptonic decays, however these diagrams are nonetheless included for completeness and it has been verified numerically that their summed contributions are negligible.

In a collider, the relevant processes are in fact $pp \to l\bar{l}jj$ and $pp \to l\bar{\nu}jj$; light jets cannot be flavour tagged, so only the sum of the processes (6.3) and (6.4) (multiplied by two since the second generation jets are indistinguishable) is observable. The first two generations of quarks are assumed to be massless for the purposes of these calculations so the cross section for the second generation will be equal to the first and a simple scaling of the results is valid. For processes (6.1) and (6.2), the opposite signs of the leptons make them distinguishable in a detector based on the direction of their paths in a magnetic field, so the processes do not need to be summed, but for experimental comparison they must still be multiplied by two to account for second generation jets.

The processes $pp \to \ell\bar{\ell}jj$ and $pp \to \ell\bar{\nu}jj$ also include $t$-channel Higgs diagrams from the processes $g\bar{q} \to \ell\bar{\ell}g\bar{q}$ and $g\bar{q} \to \ell\bar{\nu}g\bar{q}$. It has been verified in MadGraph5_aMC@NLO using the Higgs effective field theory model that their contributions are several orders of magnitude smaller than the $s$-channel diagrams that are considered and so they are neglected for this study.

Experimental analyses have been performed with the semi-leptonic channels for heavy Higgs searches [81–84] and for the SM-like Higgs boson [85–88]. The processes have been studied at the Tevatron [89, 90], a phenomenological study for the $ZZ$ case is discussed in ref. [91] and the $WW$ decays have been considered in ref. [92] although without interference effects. Reference [93] considers the processes with the as-yet unrealised prospect of charm-tagging at the Tevatron.

## 6.2 Results

### 6.2.1 Parameters and Cuts

To obtain numerical results, the renormalisation and factorisation scales are set to $M_{\ell\bar{\nu}q\bar{q}}/2$ for $V = W$ and $M_{\ell\bar{\ell}q\bar{q}}/2$ for $V = Z$. The MSTW2008LO [94] PDF set is used with default $\alpha_s$. The CKM matrix is approximated by the unit matrix, which causes a negligible error [65]. As input parameters, the recommendation of the LHC Higgs Cross Section Working Group in App. A of ref. [37] are followed, with $G_\mu$ scheme and LO weak boson widths for consistency. More specifically, $M_W = 80.398\,\text{GeV}$, $M_Z =$

91.1876 GeV, $\Gamma_W = 2.141$ GeV, $\Gamma_Z = 2.4952$ GeV, $M_t = 172.5$ GeV, $M_b = 4.75$ GeV, $G_F = 1.16637 \cdot 10^{-5}\text{GeV}^{-2}$ are used. The Higgs width $\Gamma_H$ is set to 4.098973 MeV and 26.59768 GeV for a Higgs mass of 125.5 and 400 GeV, respectively. Finite top and bottom quark mass effects are included. Lepton and light quark masses are neglected. Proton-proton collision energies of 8, 13 and 14 TeV are considered.

The narrow-width approximation is not suitable for the Higgs propagator, as was discussed in section 4.5, and so an alternative must be specified. A common choice is to use the fixed-width Breit-Wigner propagator,

$$\frac{i}{q^2 - M_H^2 + iM_H\Gamma_H} \tag{6.6}$$

and it is this choice that is adopted here. Other schemes exist; the difference is most noticeable for heavy Higgs studies (where the width is significantly broader); differences in schemes are discussed and quantified for example in refs. [95–97]

The phase space integration was performed with multi-channel mappings, implemented as discussed in section 4.3.1. There are two channels for each signal process (one for each weak boson close to on-shell), two for the $WW$ continuum background, four for the $ZZ$ continuum background (two similar to the $WW$ channels, and two with intermediate photons instead of Z bosons). The tree-level contributions require six mappings for the $WW$ case (12 for $ZZ$), dealing with diagrams of the type displayed in figure 6.2 (a) and (b), with permutations on the incoming legs for both and with the $W$ boson emitted from the other leg (again with a second permutation for the incoming legs). The singularities in these diagrams arise in the $t$-channel quark propagator when the scattering angle between incoming and outgoing massless particles is small.

Originally, mappings were included for diagrams with an $s$-channel gluon propagator as in figure 6.2 (c), but when checking that all singularities were compensated by their relevant mapping it was realised that the singularity as the $s$-channel gluon virtuality goes to zero coincided with a vanishing phase space volume and so these mappings could be eliminated.

Results for all processes are computed for the following three sets of cuts:[1]

---

[1] No jet clustering algorithm is applied.

- *minimal cuts*: $p_{Tj} > 4\,\text{GeV}$, and $M_{\ell\ell} > 4\,\text{GeV}$ for the $ZZ$ processes to eliminate soft photon singularities
- *LHC cuts* (mainly detector resolution): minimal cuts and $p_{T\ell} > 20\,\text{GeV}$, $|\eta_\ell| < 2.5$, $p_{Tj} > 25\,\text{GeV}$, $|\eta_j| < 4.5$, and for $H \to WW$ in addition: $\not{p}_T > 20\,\text{GeV}$
- *background suppression cuts* for a 400 GeV SM Higgs boson [88]: LHC cuts and $|M_{jj} - M_V| < 5\,\Gamma_V$, $p_{Tj,1st} > 60\,\text{GeV}$, $p_{Tj,2nd} > 40\,\text{GeV}$, $|\eta_j| < 2.8$, $\Delta R_{jj} < 1.3$

For the processes with intermediate $W$-boson pairs, results are also calculated using the *background suppression cuts* proposed in ref. [92] for a 125.5 GeV Higgs boson at $\sqrt{s} = 14\,\text{TeV}$:

- $p_{Tj,1st} > 30\,\text{GeV}$, $p_{Tj,2nd} > 20\,\text{GeV}$, $65\,\text{GeV} < M_{jj} < 95\,\text{GeV}$, $p_{T\ell} < 30\,\text{GeV}$, $\not{p}_T < 40\,\text{GeV}$, $|\eta_j| < 5$, $|\eta_\ell| < 2.5$, $M_{\ell\nu} < 45\,\text{GeV}$, $M_{jj\ell\nu} < 130\,\text{GeV}$, $\Delta R_{j\ell} > 0.2$

Requiring the hadronically decaying vector boson to be close to on-shell gives a dramatic improvement in the signal-to-tree-background ratio for the 125 GeV Higgs boson, since it only reduces the signal by approximately half (one of the two vector bosons will be on-shell in the signal process, with equal probability) but greatly restricts the tree-level processes since the two jets do not come from a weak boson, so have no *a priori* reason to have a combined invariant mass close to that of a weak boson.

Results are also given for the minimal and LHC cuts confined to a region around the Higgs Breit-Wigner peak, referred to as the 'on-shell' region:

- $110\,\text{GeV} < M_{VV} < 140\,\text{GeV}$

and the 'off-shell' region:

- $M_{VV} > 140\,\text{GeV}$

in order to separate interference effects related to the Higgs off-shell tail and on-shell peak regions.

### 6.2.2 Cross sections and Differential Distributions

In this section, results are presented for integrated cross sections and differential distributions for the considered Higgs signal processes, taking into account the interference with the tree- and loop-level background contributions.[2] The following notation is used:

$$S \sim |\mathcal{M}_H|^2 \tag{6.7}$$

$$B_{tree} \sim |\mathcal{M}_{tree}|^2 \tag{6.8}$$

$$B_{loop} \sim \left|\mathcal{M}_{loop}\right|^2 \tag{6.9}$$

$$B_{full} \sim \left|\mathcal{M}_{tree} + \mathcal{M}_{loop}\right|^2 \tag{6.10}$$

$$I_{tree} \sim 2\,\mathrm{Re}(\mathcal{M}_H^* \,\mathcal{M}_{tree}) \tag{6.11}$$

$$I_{loop} \sim 2\,\mathrm{Re}(\mathcal{M}_H^* \,\mathcal{M}_{loop}) \tag{6.12}$$

$$I_{full} = I_{tree} + I_{loop} \tag{6.13}$$

$$R_i = \frac{S + I_i}{S} \tag{6.14}$$

$$R_{2i} = \frac{S + B_i + I_i}{S + B_i} \,. \tag{6.15}$$

where in the final two measures the subscript $i$ refers to the interfering background. The measure $R_{2i}$, although having the advantage of being positive definite and related to the change in the observable total number of events rather than signal alone, is only suitable when the size of the two interfering contributions are of the same order, which is not the case when the tree-level backgrounds are included, unless they are greatly suppressed; it is therefore only included when it is relevant, i.e in the two sets of background suppression cuts, in table 6.4. More generally, $R_i$ gives the relative change in the signal-only contribution, and in the case of very large destructive interference can be negative.

In tables 6.1 to 6.4, integrated cross sections are given for the $WW$ process for the cuts specified above at 8, 13 and 14 TeV. Tables 6.5 and 6.6 give the results for $ZZ$ decaying to the $\ell\bar{\ell}q_u\bar{q}_u$ final state, and tables 6.7 and 6.8 show the corresponding results for the $\ell\bar{\ell}q_d\bar{q}_d$ final state.

The corresponding differential distributions for the invariant mass of the $WW$ system, denoted $M_{WW}$, are given in figures 6.5 to 6.8, and the equivalent distributions for both $ZZ$ processes are shown in figures 6.9 to 6.14.

The results presented in the tables and plots have been obtained with gg2VV and

---

[2] The interference between the tree-level and loop background contributions is at the 1% level or less. This was verified for the $ZZ$ channels and all cut sets using gg2VV.

Table 6.1: Cross sections for the signal process $gg \to H \to W^-W^+ \to \ell\bar{\nu}_\ell q_u \bar{q}_d$ ($S$) and its interference with the tree-level ($I_{tree}$) and quark-loop ($I_{loop}$) $gg$ background contributions as well as $I_{full} = I_{tree} + I_{loop}$ in $pp$ collisions at $\sqrt{s} = 8$ TeV; minimal and LHC cuts for a 125.5 GeV SM Higgs boson and background suppression cuts for a 400 GeV SM Higgs boson are applied (see main text). To illustrate the relative effect of the signal-background interference, the ratios $R_i = (S + I_i)/S$ are given. Cross sections are given for single lepton and quark flavour combinations. The integration error is displayed in brackets.

| $gg \to H \to W^-W^+ \to \ell\bar{\nu}_\ell q_u \bar{q}_d$<br>$\sigma$ [fb], $pp$, $\sqrt{s} = 8$ TeV | | | interference | | | ratio | | |
|---|---|---|---|---|---|---|---|---|
| $M_H$ [GeV] | cuts | $S$ | $I_{tree}$ | $I_{loop}$ | $I_{full}$ | $R_{tree}$ | $R_{loop}$ | $R_{full}$ |
| 125.5 | min. | 67.28(9) | -2.47(2) | -4.99(1) | -7.48(9) | 0.963(2) | 0.926(2) | 0.889(3) |
| 125.5 | LHC | 1.978(6) | 0.266(4) | -2.647(6) | -2.38(3) | 1.135(5) | -0.338(4) | -0.20(2) |
| 400 | bkg. | 13.30(2) | -0.0054(2) | -1.052(5) | -1.058(4) | 1.000(2) | 0.921(2) | 0.920(2) |

Table 6.2: Cross sections for the signal process $gg \to H \to W^-W^+ \to \ell\bar{\nu}_\ell q_u \bar{q}_d$ and its interference with the tree-level and quark-loop $gg$ background contributions in $pp$ collisions at $\sqrt{s} = 13$ TeV. Other details as in table 6.1.

| $gg \to H \to W^-W^+ \to \ell\bar{\nu}_\ell q_u \bar{q}_d$<br>$\sigma$ [fb], $pp$, $\sqrt{s} = 13$ TeV | | | interference | | | ratio | | |
|---|---|---|---|---|---|---|---|---|
| $M_H$ [GeV] | cuts | $S$ | $I_{tree}$ | $I_{loop}$ | $I_{full}$ | $R_{tree}$ | $R_{loop}$ | $R_{full}$ |
| 125.5 | min. | 162.1(3) | -5.9(1) | -15.36(4) | -21.2(4) | 0.964(3) | 0.905(2) | 0.869(3) |
| 125.5 | LHC | 5.56(2) | 0.83(3) | -8.34(3) | -7.51(7) | 1.15(2) | -0.500(5) | -0.35(2) |
| 400 | bkg. | 43.10(4) | -0.018(2) | -4.29(2) | -4.30(4) | 1.000(2) | 0.901(2) | 0.900(2) |

cross checked with MadGraph5_aMC@NLO [78].

Table 6.3: Cross sections for the signal process $gg \to H \to W^-W^+ \to \ell\bar{\nu}_\ell q_u \bar{q}_d$ and its interference with the tree-level and quark-loop $gg$ background contributions in $pp$ collisions at 13 and 14 TeV with background suppression cuts for a 125.5 GeV SM Higgs boson at $\sqrt{s} \approx 14$ TeV (see main text). Other details as in table 6.1.

| $gg \to H \to W^-W^+ \to \ell\bar{\nu}_\ell q_u \bar{q}_d$<br>$\sigma$ [fb], $pp$, $M_H = 125.5$ GeV<br>background suppression cuts | | interference | | | ratio | | |
|---|---|---|---|---|---|---|---|
| $\sqrt{s}$ [TeV] | $S$ | $I_{tree}$ | $I_{loop}$ | $I_{full}$ | $R_{tree}$ | $R_{loop}$ | $R_{full}$ |
| 13 | 42.16(5) | -0.0148(5) | 0.0264(2) | 0.0118(6) | 1.000(2) | 1.001(2) | 1.000(2) |
| 14 | 47.44(5) | -0.0164(5) | 0.029(1) | 0.0131(6) | 1.000(2) | 1.001(2) | 1.000(2) |

Table 6.4: Cross sections for the signal process $gg \to H \to W^-W^+ \to \ell\bar{\nu}_\ell q_u\bar{q}_d$ and its interference with the tree-level and quark-loop $gg$ background contributions in $pp$ collisions at 8, 13 and 14 TeV with background suppression cuts (different for each mass) for a 125.5 GeV or 400 GeV SM Higgs boson as described in the text. The $R_2$ results show the relative change in signal + indicated background when interference is included. The subscript "full" indicates tree and continuum background contributions combined.

| $gg \to H \to W^-W^+ \to \ell\bar{\nu}_\ell q_u\bar{q}_d$<br>$\sigma$ [fb], $pp$, $M_H = 125.5$ GeV<br>background suppression cuts | | | | | | | |
|---|---|---|---|---|---|---|---|
| $\sqrt{s}$ [TeV] | $M_H$ [GeV] | $S$ | $S + B_{full}$ | $S + B_{full} + I_{full}$ | $R_{2tree}$ | $R_{2loop}$ | $R_{2full}$ |
| 8 | 400 | 13.30(2) | 23.88(3) | 22.82(3) | 1.000(2) | 0.928(2) | 0.956(2) |
| 13 | 400 | 43.10(4) | 76.0(2) | 71.7(2) | 1.000(2) | 0.911(2) | 0.943(2) |
| 13 | 125.5 | 42.16(5) | 47.5(2) | 47.5(2) | 1.000(4) | 1.001(2) | 1.000(4) |
| 14 | 125.5 | 47.44(5) | 53.5(3) | 53.5(3) | 1.000(6) | 1.001(2) | 1.000(6) |

Table 6.5: Cross sections for the signal process $gg \to H \to ZZ \to \ell\bar{\ell}q_u\bar{q}_u$ and its interference with the tree-level and quark-loop $gg$ background contributions. $\gamma^*$ background contributions are included. Other details as in table 6.1.

| $gg \to H \to ZZ \to \ell\bar{\ell}q_u\bar{q}_u$<br>$\sigma$ [fb], $pp$, $\sqrt{s} = 8$ TeV | | | interference | | | ratio | | |
|---|---|---|---|---|---|---|---|---|
| $M_H$ [GeV] | cuts | $S$ | $I_{tree}$ | $I_{loop}$ | $I_{full}$ | $R_{tree}$ | $R_{loop}$ | $R_{full}$ |
| 125.5 | min. | 1.954(2) | -0.19(2) | -0.3442(6) | -0.535(9) | 0.902(7) | 0.824(2) | 0.726(5) |
| 125.5 | LHC | 0.1164(7) | 0.0173(9) | -0.1940(4) | -0.177(2) | 1.15(2) | -0.667(7) | -0.52(2) |
| 400 | bkg. | 1.256(2) | -0.00082(4) | -0.0908(3) | -0.0917(3) | 0.999(2) | 0.928(2) | 0.927(2) |

Table 6.6: Cross sections for the signal process $gg \to H \to ZZ \to \ell\bar{\ell}q_u\bar{q}_u$ and its interference with the tree-level and quark-loop $gg$ background contributions in $pp$ collisions at $\sqrt{s} = 13$ TeV. Other details as in table 6.5.

| $gg \to H \to ZZ \to \ell\bar{\ell}q_u\bar{q}_u$<br>$\sigma$ [fb], $pp$, $\sqrt{s} = 13$ TeV | | | interference | | | ratio | | |
|---|---|---|---|---|---|---|---|---|
| $M_H$ [GeV] | cuts | $S$ | $I_{tree}$ | $I_{loop}$ | $I_{full}$ | $R_{tree}$ | $R_{loop}$ | $R_{full}$ |
| 125.5 | min. | 4.79(4) | -0.45(3) | -1.088(2) | -1.54(3) | 0.91(2) | 0.773(9) | 0.68(1) |
| 125.5 | LHC | 0.375(2) | 0.063(7) | -0.612(1) | -0.552(6) | 1.17(2) | -0.633(6) | -0.47(2) |
| 400 | bkg. | 4.043(4) | -0.0027(3) | -0.3569(9) | -0.359(3) | 0.999(2) | 0.912(2) | 0.911(2) |

Table 6.7: Cross sections for the signal process $gg \to H \to ZZ \to \ell\bar{\ell}q_d\bar{q}_d$ and its interference with the tree-level and quark-loop $gg$ background contributions. Other details as in table 6.5.

| $gg \to H \to ZZ \to \ell\bar{\ell}q_d\bar{q}_d$<br>$\sigma$ [fb], $pp$, $\sqrt{s} = 8$ TeV | | | interference | | | ratio | | |
|---|---|---|---|---|---|---|---|---|
| $M_H$ [GeV] | cuts | $S$ | $I_{tree}$ | $I_{loop}$ | $I_{full}$ | $R_{tree}$ | $R_{loop}$ | $R_{full}$ |
| 125.5 | min. | 2.505(4) | -0.244(3) | -0.443(1) | -0.686(6) | 0.903(2) | 0.823(2) | 0.726(3) |
| 125.5 | LHC | 0.1498(4) | 0.022(2) | -0.2493(5) | -0.227(2) | 1.146(9) | -0.664(5) | -0.52(2) |
| 400 | bkg. | 1.611(2) | -0.00110(4) | -0.1167(3) | -0.1176(4) | 0.999(2) | 0.928(2) | 0.927(2) |

Table 6.8: Cross sections for the signal process $gg \to H \to ZZ \to \ell\bar{\ell}q_d\bar{q}_d$ and its interference with the tree-level and quark-loop $gg$ background contributions in $pp$ collisions at $\sqrt{s} = 13$ TeV. Other details as in table 6.5.

| $gg \to H \to ZZ \to \ell\bar{\ell}q_d\bar{q}_d$<br>$\sigma$ [fb], $pp$, $\sqrt{s} = 13$ TeV | | | interference | | | ratio | | |
|---|---|---|---|---|---|---|---|---|
| $M_H$ [GeV] | cuts | $S$ | $I_{tree}$ | $I_{loop}$ | $I_{full}$ | $R_{tree}$ | $R_{loop}$ | $R_{full}$ |
| 125.5 | min. | 6.16(2) | -0.57(3) | -1.396(3) | -1.97(2) | 0.907(5) | 0.773(3) | 0.680(4) |
| 125.5 | LHC | 0.4809(9) | 0.077(8) | -0.786(2) | -0.708(5) | 1.16(2) | -0.635(4) | -0.47(2) |
| 400 | bkg. | 5.185(5) | -0.0038(4) | -0.457(1) | -0.461(2) | 0.999(2) | 0.912(2) | 0.911(2) |

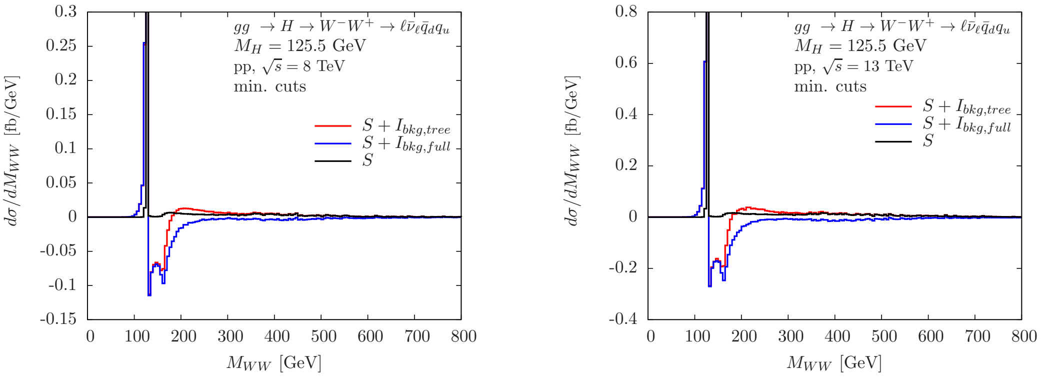

Figure 6.5: Invariant $WW$ mass distributions for the signal process $gg \to H \to W^-W^+ \to \ell\bar{\nu}_\ell q_u\bar{q}_d$ ($S$) and including its interference with the tree-level ($S + I_{bkg,tree}$) and in addition quark-loop ($S + I_{bkg,full}$) $gg$ background contributions in $pp$ collisions at $\sqrt{s} = 8$ TeV (left) and 13 TeV (right) for a 125.5 GeV SM Higgs boson. Minimal cuts are applied (see main text). Other details as in table 6.1.

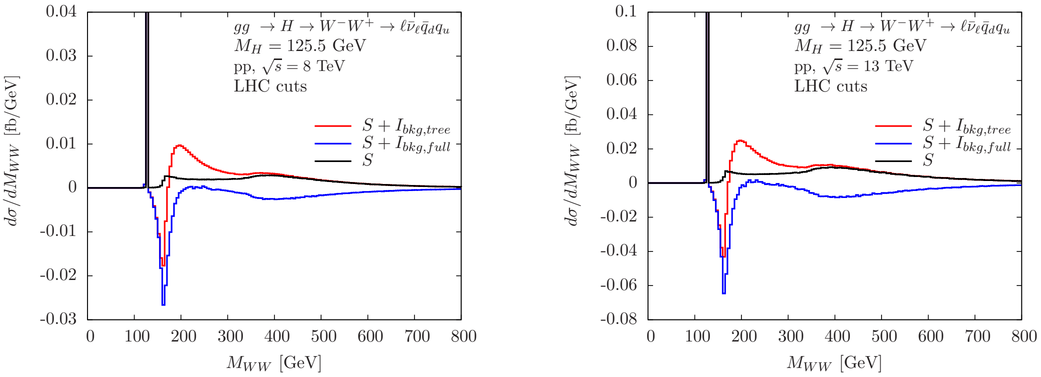

Figure 6.6: Invariant $WW$ mass distributions for the signal process $gg \to H \to W^-W^+ \to \ell\bar{\nu}_\ell q_u\bar{q}_d$ and including its interference with the background. LHC cuts are applied (see main text). Other details as in figure 6.5.

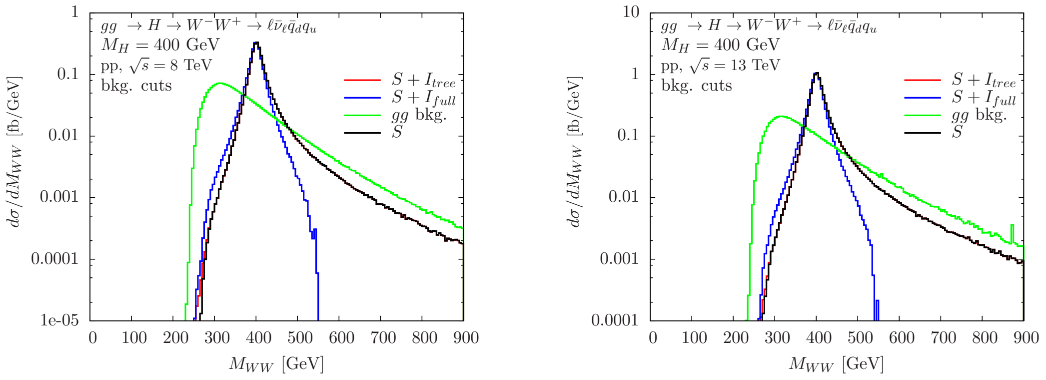

Figure 6.7: Invariant $WW$ mass distributions for the signal process $gg \to H \to W^-W^+ \to \ell\bar{\nu}_\ell q_u\bar{q}_d$ and including its interference with the background with background suppression cuts for a 400 GeV SM Higgs boson (see main text). The $gg$ background is also displayed. Other details as in figure 6.5.

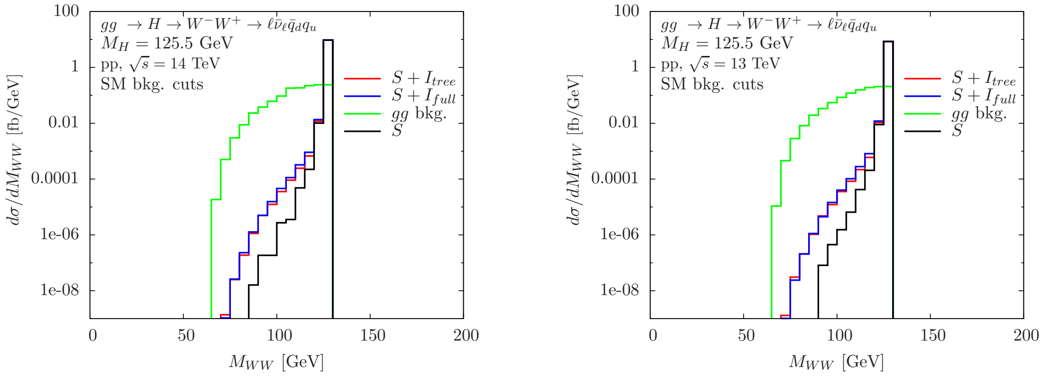

Figure 6.8: Invariant $WW$ mass distributions for the signal process $gg \to H \to W^-W^+ \to \ell\bar{\nu}_\ell q_u\bar{q}_d$ and including its interference with the background with background suppression cuts for a 125.5 GeV Higgs boson at $\sqrt{s} = 14$ TeV (see main text). Other details as in figure 6.7.

The LHC cuts result in a dramatic suppression of the signal cross section for all processes; this is somewhat surprising since they are not particularly stringent cuts. In fact, most of the reduction comes from the $p_T > 20\,\text{GeV}$ cut on all final state particles (or final state observable particles and missing transverse momentum for the $WW$ case). The $WW$ case is considered to illustrate the effect: if the two $W$ bosons are approximately at rest in the parton centre-of-mass frame, it is expected that the sum of their invariant masses should be very close to the Higgs boson mass, by conservation of energy:

$$E_H = E_{W^-} + E_{W^+} = \sqrt{\left(\vec{p}_{W^-}^{\,2} + M_{W^-}^2\right)} + \sqrt{\left(\vec{p}_{W^+}^{\,2} + M_{W^+}^2\right)}. \tag{6.16}$$

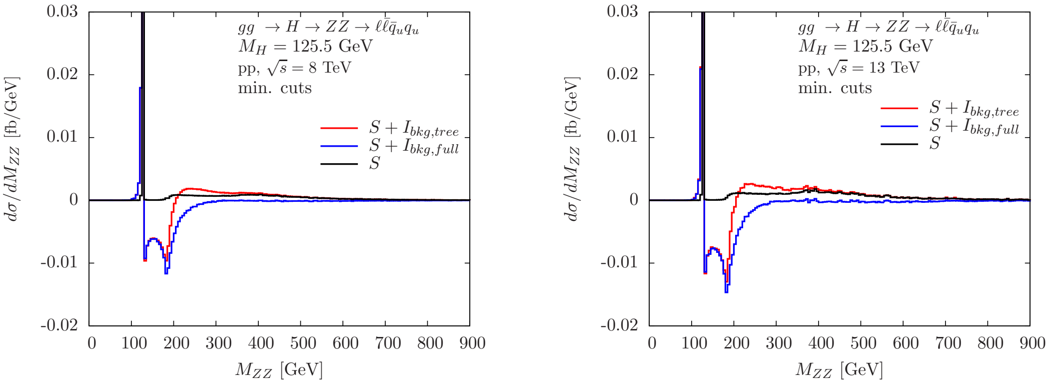

Figure 6.9: Invariant $ZZ$ mass distributions for the signal process $gg \to H \to ZZ \to \ell\bar{\ell}q_u\bar{q}_u$ and including its interference with the tree-level ($S + I_{bkg,tree}$) and in addition quark-loop ($S + I_{bkg,full}$) $gg$ background contributions in $pp$ collisions at $\sqrt{s} = 8$ TeV (left) and 13 TeV (right) for a 125.5 GeV SM Higgs boson. Minimal cuts are applied (see main text).

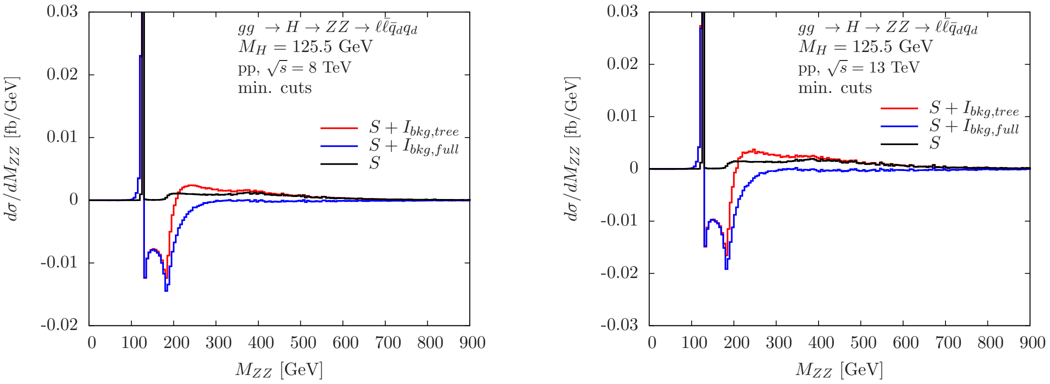

Figure 6.10: Invariant $ZZ$ mass distributions for the signal process $gg \to H \to ZZ \to \ell\bar{\ell}q_d\bar{q}_d$ and including its interference with the background. Minimal cuts are applied (see main text). Other details as in figure 6.9.

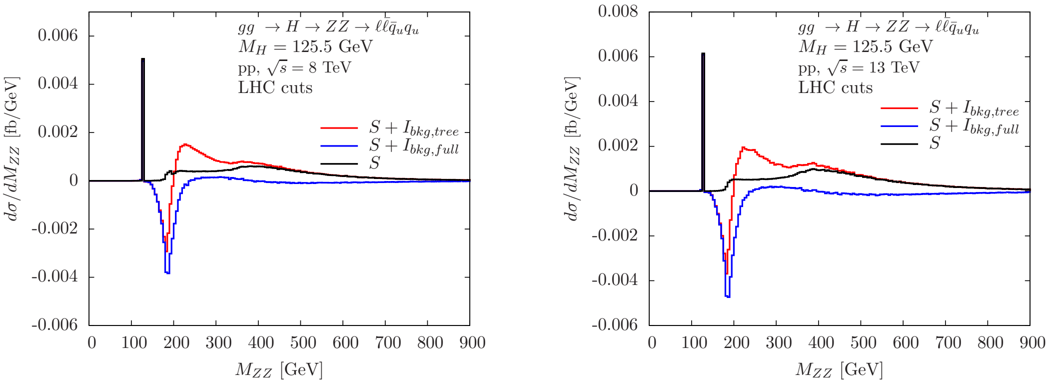

Figure 6.11: Invariant $ZZ$ mass distributions for the signal process $gg \to H \to ZZ \to \ell\bar{\ell}q_u\bar{q}_u$ and including its interference with the background. LHC cuts are applied (see main text). Other details as in figure 6.9.

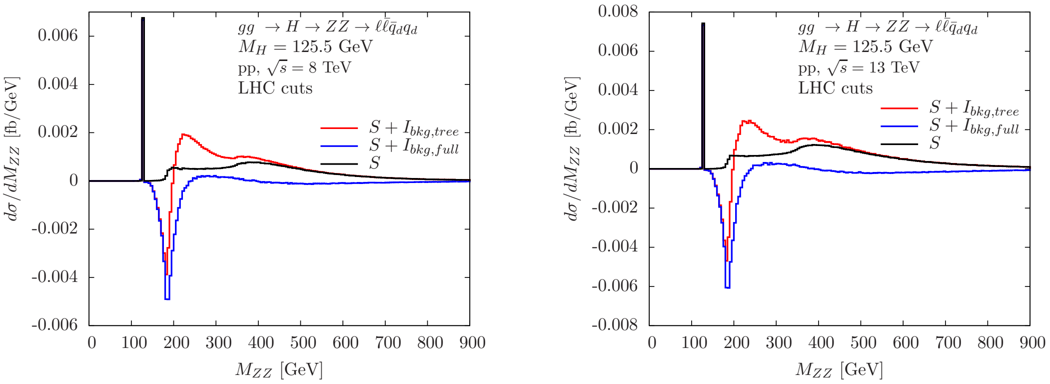

Figure 6.12: Invariant $ZZ$ mass distributions for the signal process $gg \to H \to ZZ \to \ell\bar{\ell}q_d\bar{q}_d$ and including its interference with the background. LHC cuts are applied (see main text). Other details as in figure 6.9.

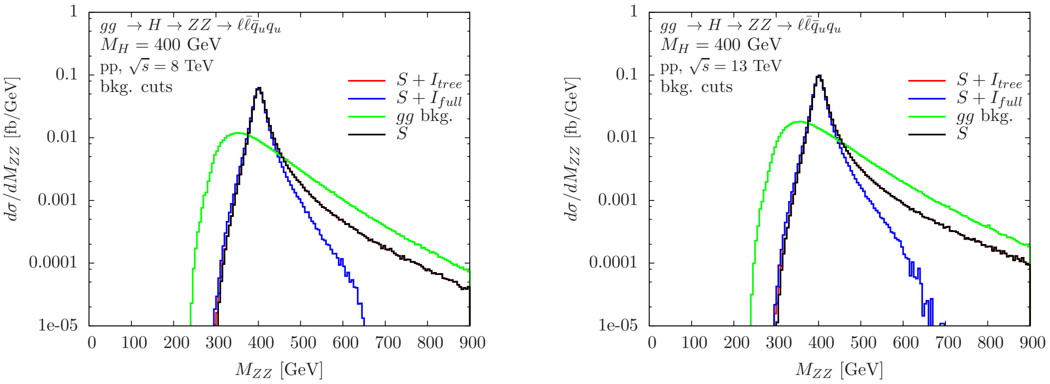

Figure 6.13: Invariant $ZZ$ mass distributions for the signal process $gg \to H \to ZZ \to \ell\bar{\ell}q_u\bar{q}_u$ and including its interference with the background with background suppression cuts for a 400 GeV SM Higgs boson (see main text). The $gg$ background is also displayed. Other details as in figure 6.9.

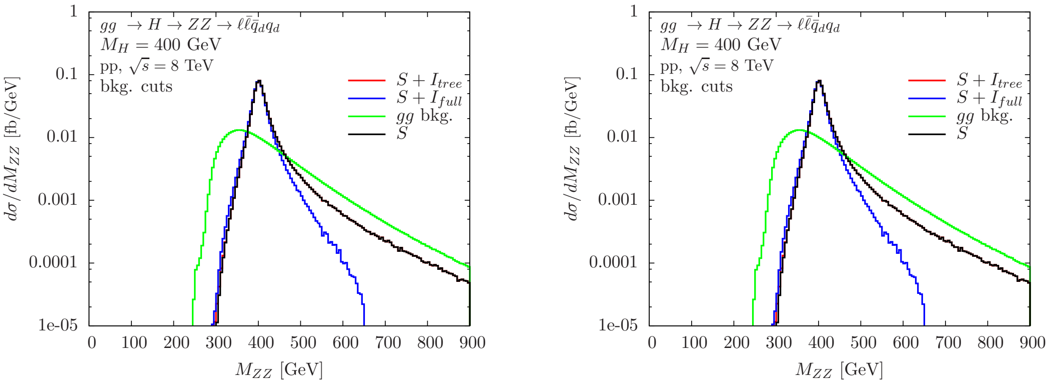

Figure 6.14: Invariant $ZZ$ mass distributions for the signal process $gg \to H \to ZZ \to \ell\bar{\ell}q_d\bar{q}_d$ and including its interference with the background with background suppression cuts for a 400 GeV SM Higgs boson (see main text). The $gg$ background is also displayed. Other details as in figure 6.9.

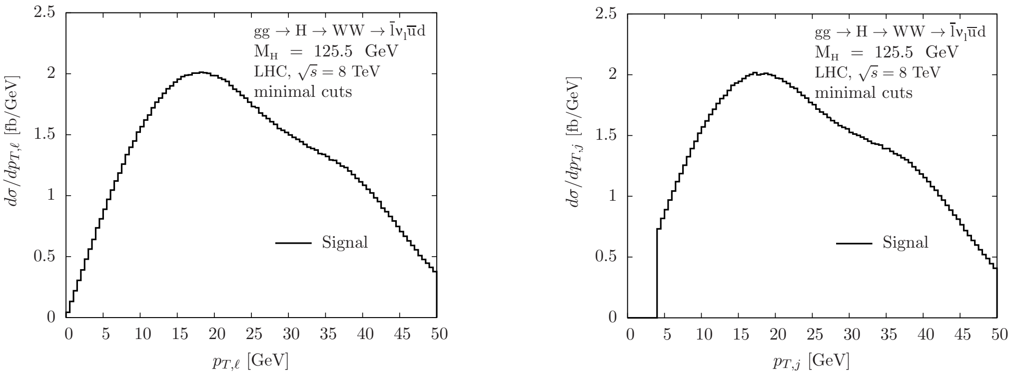

Figure 6.15: Distributions of $p_T$ for final state charged lepton (left) and $\bar{u}$ (right) for the signal process $gg \to H \to W^+W^- \to \bar{\ell}\nu_\ell q_d\,\bar{q}_u$. A $p_T > 4$ GeV is applied to both jets. The $d$ quark and neutrino (missing $p_T$) plots are identical.

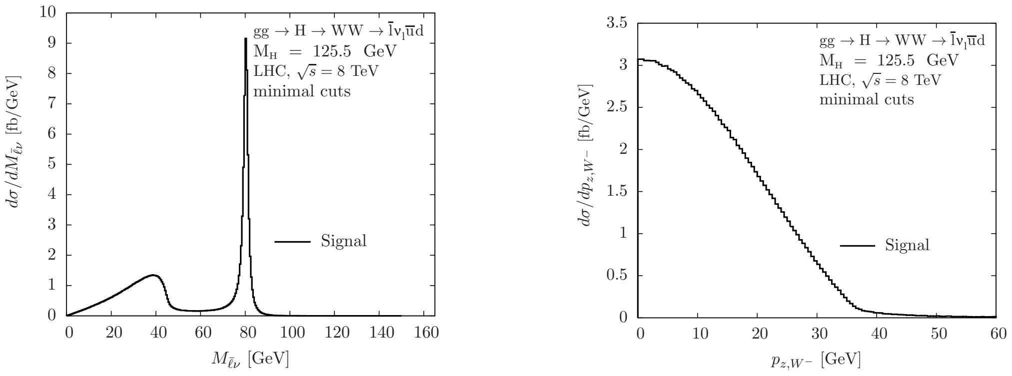

Figure 6.16: Invariant mass (left) and longitudinal momentum (right) of the $W^+$ in the process $gg \to H \to W^+W^- \to \bar{\ell}\nu_\ell q_d\,\bar{q}_u$ with minimal cuts only. The $W^-$ plots are identical.

If this were the case, one vector boson (resonant) would typically have an invariant mass very close to $M_W$ and the other an invariant mass close to $M_H - M_W \sim 44$ GeV. Assuming both $W$ bosons decay roughly isotropically to massless final state particles, one would expect that the final state particles have typical values of $p_T \sim \frac{M_H - M_W}{2} \sim 22$ GeV for the non-resonant boson products, and $p_T \sim \frac{M_W}{2}$ for the resonant boson products. A $p_T > 20$ GeV cut would therefore preserve the majority of the signal if both W bosons were approximately at rest in the parton-center-of-mass frame.

In fact, figure 6.15 shows that with minimal cuts the final state $p_T$ distributions peak at between 18 and 19 GeV. This is a consequence of the fact that the $W$ bosons are *not* approximately at rest in the parton centre-of-mass frame: figure 6.16 (right) shows that approximately 55% of the $W$ bosons have a longitudinal momentum of 10 GeV or greater,

Table 6.9: Cross sections for the signal process $gg \to H \to W^-W^+ \to \ell\bar{\nu}_\ell q_u\bar{q}_d$ $(S)$ as in table 6.1 but with an additional 'on-shell' cut $110\,\mathrm{GeV} < M_{VV} < 140\,\mathrm{GeV}$ to illustrate the effect close to the on-shell region.

| $gg \to H \to W^-W^+ \to \ell\bar{\nu}_\ell q_u\bar{q}_d$ | | | | | | | | |
|---|---|---|---|---|---|---|---|---|
| $\sigma$ [fb], $pp$, $\sqrt{s} = 8\,\mathrm{TeV}$ | | | interference | | | ratio | | |
| $M_H$ [GeV] | cuts | $S$ | $I_{tree}$ | $I_{loop}$ | $I_{full}$ | $R_{tree}$ | $R_{loop}$ | $R_{full}$ |
| 125.5 | min. | 65.69(8) | −1.06(2) | 0.0235(2) | −1.04(2) | 0.984(2) | 1.000(2) | 0.984(2) |
| 125.5 | LHC | 0.933(2) | −0.0196(6) | −0.00040(2) | −0.0200(6) | 0.979(3) | 1.000(3) | 0.979(3) |

Table 6.10: Cross sections for the signal process $gg \to H \to W^-W^+ \to \ell\bar{\nu}_\ell q_u\bar{q}_d$ $(S)$ as in table 6.1 but with an additional 'off-shell' cut $M_{VV} > 140\,\mathrm{GeV}$ to illustrate the effect in the off-shell region.

| $gg \to H \to W^-W^+ \to \ell\bar{\nu}_\ell q_u\bar{q}_d$ | | | | | | | | |
|---|---|---|---|---|---|---|---|---|
| $\sigma$ [fb], $pp$, $\sqrt{s} = 8\,\mathrm{TeV}$ | | | interference | | | ratio | | |
| $M_H$ [GeV] | cuts | $S$ | $I_{tree}$ | $I_{loop}$ | $I_{full}$ | $R_{tree}$ | $R_{loop}$ | $R_{full}$ |
| 125.5 | min. | 1.64(4) | −1.46(5) | −5.01(2) | −6.47(5) | 0.11(4) | −2.06(5) | −2.95(7) |
| 125.5 | LHC | 1.042(2) | 0.29(1) | −2.650(7) | −2.36(2) | 1.28(1) | −1.543(8) | −1.27(2) |

indicating a non-negligible boost along this axis. This is evident in the $W$ invariant-mass plot, figure 6.16 (left), where the secondary peak is just below 40 GeV, and nearly 80% of the off-shell vector bosons have an invariant mass of less than 40 GeV. Each final state $p_T$ cut (i.e. $p_{T,j}$ for two jets, $p_{T,miss}$ and $p_{T,\ell}$) then individually gives a large reduction, although there will be correlations between the cuts so it is not straightforward to estimate the exact value of the total effect. This leads to the very large signal reduction observed in the results.

## 6.3 Discussion

The impact of the full signal-background interference on integrated signal cross sections over the entire phase space can range from $\mathcal{O}(1)$ for typical LHC selection cuts to $\mathcal{O}(0.1\%)$ with appropriate background suppression cuts. The relative importance in the integrated cross section of the different types of interference in the on-shell and off-shell regions is shown in tables 6.9 and 6.10 respectively, for the minimal and LHC cuts.

Aside from the effect on the integrated cross section, it is useful to consider the $M_{VV}$ invariant mass distributions to understand the behaviour of the different types of interferences. With minimal cuts, the tree-level interference is large close to the Higgs on-shell region, but changes sign at $\hat{s} = M_H^2$ so that the effect on the total cross section is largely cancelled out. However, any cuts that suppress the tree-level background dampen this interference, and in all cases it is sub-leading to the destructive continuum interference which dominates away from the peak, and indeed overtakes the signal in size in this region.

For the light SM Higgs with background suppression cuts such as those suggested in ref. [92], the total effect of the signal-background interference on the integrated cross section can be reduced to the per mille level in the $WW$ channel as the invariant mass is forced to remain very close to the mass of the Higgs, removing both the tree- and loop-level backgrounds. In this case the tree-level interference is completely negligible, and the continuum interference tiny. Similar behaviour is expected for the $ZZ$ processes with an appropriate set of cuts. Similarly, background suppression cuts for a heavy SM-like Higgs boson can lower the interference to below the 10% level for the $WW$ and $ZZ$ channel.

The tree and continuum interference-only invariant mass distributions are shown for minimal and LHC cuts in figure 6.17. To better understand the behaviour of the two kinds of interference, it is useful to consider the structure of the amplitudes involved. For two interfering amplitudes, say $\mathcal{A}_{sig} = \mathcal{A}_{gg\to H\to f.s.}$ and $\mathcal{A}_{bkg} = \mathcal{A}_{gg\to f.s.}$, where $\mathcal{A}_{sig}$ includes an $s$-channel Breit-Wigner resonance which can be factored out, the amplitude has the structure:

$$\begin{aligned}\sigma &\sim \left|\mathcal{A}_{gg\to f.s.} + \frac{1}{\hat{s} - M_H^2 + iM_H\Gamma_H}\mathcal{A}_{gg\to H}A_{H\to fs}\right|^2 \\ &= \left|\mathcal{A}_{gg\to f.s.}\right|^2 + \left|\mathcal{A}_{sig}\right|^2 + 2\left(\hat{s} - M_H^2\right)\frac{\mathrm{Re}(\mathcal{A}_{gg\to H}A_{H\to fs}A^*_{gg\to f.s.})}{(\hat{s} - M_H^2)^2 + (M_H\Gamma_H)^2} \\ &- 2M_H\Gamma_H\frac{\mathrm{Im}(\mathcal{A}_{gg\to H}A_{H\to fs}A^*_{gg\to f.s.})}{(\hat{s} - M_H^2)^2 + (M_H\Gamma_H)^2}.\end{aligned} \tag{6.17}$$

It can be seen that there are two types of possible contribution to the interference: the first, proportional to the real part of the amplitude products, changes sign at $\hat{s} = M_H^2$, and is relevant only close to the peak region. The second part requires a relative phase difference between the two types of amplitude, which can arise (apart from Breit-Wigner propagators, which contribute a small imaginary component) in CP-violating effects, which are not considered here, or in loops when particles in the loop can go on-shell (by the optical theorem). It can then be guessed that the real portion gives the dominant

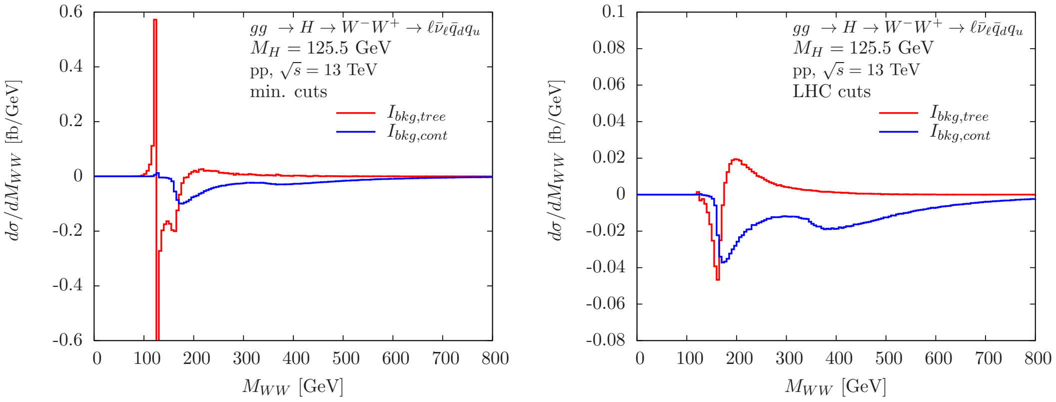

Figure 6.17: As figures 6.5 and 6.6, but with the interference contributions only.

contribution to the tree-level interference, and indeed it can be seen (in the minimal cuts case) that the red line is only significant in a region around the resonance peak and switches sign as it goes through it. There is a bump at approximately $2M_W$, where the signal amplitude is enhanced since the two W bosons can go on-shell. The effect of the real contribution on the total cross section is sub-leading compared to the continuum interference. Any cuts which suppress the tree-level background in the signal region will dampen this interference, as can be seen in the LHC cuts plot.

By contrast, the continuum interference is relevant away from the peak - entirely above it in fact - and has features at the points where it is known that there are enhancements in the imaginary components of the continuum and signal amplitudes. In the Feynman diagrams considered in this study, there are enhancements in the imaginary components both the signal and continuum amplitudes at $2M_V$ and $2M_t$. This interference survives detector selection cuts and gives the dominant effects on the total cross section.

It is noted that the behaviour of the differential distributions is similar for the $WW$ and $ZZ$ cases, and that the two $ZZ$ subprocesses also display the same features.

It should be pointed out that, although large interference in the off-shell region is unsurprising, it emphasises that interference effects must be (and are) included in studies of similar processes that depend on the different amplitude dependence of the on/off-shell regions, notably the limit given on the Higgs width which relies on the ratio of the two regions. Although typical background suppression cuts are effective at suppressing interference, they are not suitable for such studies which require a reasonable number of events away from the signal region, and it is therefore crucial to take the continuum interference effects into account in such a measurement.

In summary, the semi-leptonic processes experience significant destructive continuum interference effects away from the on-peak region, in common with the fully leptonic processes. Although arising from the dominant background, tree-level interference effects are sub-leading and mitigated by cuts. It can then be concluded that higher-order background contributions can induce leading interference effects. Consequently, precision calculations of interference effects are well motivated.

# Chapter 7

# Interference Effects in Fully Leptonic Decays in the Higgs Singlet Model

The Higgs singlet model (1HSM), also known as the electroweak singlet model, is of great interest as a beyond the Standard Model (BSM) benchmark since it is the minimal SM extension that contains an additional Higgs boson. It adds a real singlet field, neutral under all the SM gauge groups, and therefore its effects are only felt through mixing with the SM Higgs boson. The 1-Higgs-singlet extension of the SM has been extensively explored in the literature [70, 98–121]. Higgs singlet models with an additional $Z_2$ symmetry, included in the above references, have generated some interest recently because of the possibility of the additional Higgs boson being a dark matter candidate, but here the most general extension is considered. In particular, references [122, 123] describe the model in detail. A summary is given here.

## 7.1 Model Description

The SM Higgs sector is extended by the addition of a new real scalar field, $S$, which is a singlet under all the gauge groups of the SM and which also gets a vacuum expectation value (VEV) under electroweak symmetry breaking. The most general gauge-invariant potential can be written as [122, 124]

$$\begin{aligned} V(S,\Phi) = \lambda\left(\Phi^\dagger\Phi - \frac{v_{EW}^2}{2}\right)^2 - \mu^2\left(\Phi^\dagger\Phi - \frac{v_{EW}^2}{2}\right) + \frac{1}{2}M^2S^2 + \lambda_1 S^4 \\ + \lambda_2 S^2\left(\Phi^\dagger\Phi - \frac{v_{EW}^2}{2}\right) + \mu_1 S^3 + \mu_2 S\left(\Phi^\dagger\Phi - \frac{v_{EW}^2}{2}\right) + \mu_3 S. \end{aligned} \tag{7.1}$$

A vacuum expectation value can be assigned to the $\Phi$ doublet as usual, and also to the singlet scalar field $s$:

$$\Phi = \begin{pmatrix} 0 \\ (\phi + v)/\sqrt{2} \end{pmatrix} \qquad\qquad S = s + x \tag{7.2}$$

and, as in the SM, the minima of $V(S,\Phi)$ are found by solving:

$$\begin{aligned} \left.\frac{\partial V(S,\Phi)}{\partial \Phi}\right|_{S=x,\Phi=\frac{v}{\sqrt{2}}} &= v\left(-\mu^2 + 2\lambda v^2 + \mu_2 x + \lambda_2 x^2\right) = 0 \\ \left.\frac{\partial V(S,\Phi)}{\partial S}\right|_{S=x,\Phi=\frac{v}{\sqrt{2}}} &= x(M^2 + 4\lambda_1 x^2 + \lambda_2 v^2 + 3\mu_1 x) + \mu_3 = 0 \end{aligned} \tag{7.3}$$

It is possible to choose $x = 0$, since a universal shift in the singlet field simply corresponds to a redefinition of the coefficients in eq. (7.1), leaving the usual electroweak symmetry breaking solution of $v^2 = \frac{\mu^2}{2\lambda}$ and giving $\mu_3 = 0$. Other minima of course exist; a detailed treatment is given in ref. [125] but here it is simply noted that in order to guarantee that the electroweak vacuum solution is still a local minimum and prevent the potential from becoming unbounded from below (i.e. avoiding vacuum instability), the quadratic part of the potential must be positive definite.[1] This gives the restrictions

$$\lambda > 0, \quad \lambda_1 > 0, \quad \lambda_2 > -2\sqrt{\lambda\lambda_1}. \tag{7.4}$$

The trilinear couplings $\mu_1$ and $\mu_2$ can have positive or negative sign.

As an aside, it is noted that the mentioned $Z_2$ symmetry would exclude $\lambda_1$, $\mu_1$ and $\mu_3$ and would also prohibit the shifting of the singlet field to set $x = 0$. The ratio of VEVs, $\tan\beta = \frac{v}{x}$ is then a useful parameter of that model.

---

[1] In the limit of very large field values the quadratic terms will always dominate and so only the $\lambda_i$ terms are relevant.

Expanding about the electroweak minimum and substituting eq. (7.2) into eq. (7.1) gives the potential

$$\begin{aligned} V = &\frac{\lambda}{4}\phi^4 + \lambda v^2\phi^2 + \lambda v\phi^3 + \frac{1}{2}M^2 s^2 + \lambda_1 s^4 + \frac{\lambda_2}{2}\phi^2 s^2 + \lambda_2 v\phi s^2 \\ &+ \mu_1 s^3 + \frac{\mu_2}{2}\phi^2 s + \mu_2 v\phi s. \end{aligned} \tag{7.5}$$

The mass eigenstates can be parametrised in terms of a mixing angle $\theta$ as

$$h_1 = \phi\cos\theta - s\sin\theta\,, \tag{7.6}$$

$$h_2 = \phi\sin\theta + s\cos\theta\,, \tag{7.7}$$

where $h_1$ is assumed to be the lighter Higgs boson with a mass of 125 GeV, and

$$\tan 2\theta = \frac{-\mu_2 v}{\lambda v^2 - \frac{1}{2}M^2} \tag{7.8}$$

with

$$-\frac{\pi}{4} < \theta < \frac{\pi}{4} \tag{7.9}$$

under the condition $M^2 > 2\lambda v^2$. The model has six independent parameters, which we choose to be $M_{h1}, M_{h2}, \theta, \mu_1, \lambda_1$ and $\lambda_2$. The dependent model parameters are:

$$\lambda = \frac{\cos(2\theta)\left(M_{h1}^2 - M_{h2}^2\right) + M_{h1}^2 + M_{h2}^2}{4v^2}\,, \tag{7.10}$$

$$M^2 = \frac{M_{h2}^2 - M_{h1}^2 + \sec(2\theta)\left(M_{h1}^2 + M_{h2}^2\right)}{2\sec(2\theta)}\,, \tag{7.11}$$

$$\mu_2 = -\tan(2\theta)\;\frac{\lambda v^2 - \frac{1}{2}M^2}{v}\,. \tag{7.12}$$

The full list of vertices for the new trilinear and quartic $h_2 - h_1$ interactions is not given here, see for example ref. [123], but it is instructive to show the only new coupling directly relevant to the study performed in this chapter; the Feynman rule for the $h_2 h_1 h_1$ vertex is:

$$-2i\left(3\lambda v\sin\theta\cos\theta - \lambda_2 v\sin\theta\left(3\cos^2\theta - 1\right) + 3\mu_1\cos\theta\sin^2\theta + \frac{\mu_2}{2}\cos\theta\left(3\cos^2\theta - 1\right)\right), \tag{7.13}$$

and is relevant to the leptonic SM-like decays only in the calculation of the width of $h_2$, which is performed using FeynRules [126].

## 7.2 Experimental Limits and Phenomenology

If an extended portal-like Higgs sector is realised in nature, it would be expected that evidence could be seen in the coming runs of the LHC. There are two main signatures: the suppression of the cross sections of the SM processes of the lighter particle [2] by a factor of (in the 1HSM) $\cos^4\theta$, and the presence of a new heavy resonance which would have the same SM decays as the light resonance and (assuming $M_{h2} > 250\,\mathrm{GeV}$) induce the new $h_2 \to h_1 h_1$ decay. These features are common to any extended Higgs sector model where the couplings of the Higgs to bosons and fermions are scaled by a universal factor, and many of their constraints can be formulated in a model independent way with the 'kappa formalism' in section 13.3 of reference [123].

This means that studies of the limits on the $Z_2$ model are broadly applicable, in particular that of [121], on which the following discussion is based. The authors take into account the latest LHC results and perform a comprehensive study of the constraints from electroweak precision tests, Higgs data from the LHC and many other sources, and give limits from the combined ATLAS and CMS Run I data; the observed signal strength for the Higgs boson with a mass of 125.09 GeV of $\mu = 1.09 \pm 0.11$ gives a constraint over the whole range of heavy Higgs masses of:

$$|\sin\theta| \leq 0.36 \tag{7.14}$$

Furthermore, for specific masses above approximately 300 GeV tighter constraints arise from NLO calculations of the W-boson mass. For example for the values chosen in the study presented below, $M_{h2} = 300(600)[900]$ GeV, the maximal value of $\sin\theta$ is reduced to approximately 0.3(0.2)[0.2].

Searches for high mass Higgs-like resonances have been performed by ATLAS and CMS [127–134]. The only significant excess that has been seen so far, in the di-photon

---

[2] In this discussion, $h_1$ is always assumed to be the lighter Higgs-like resonance, consistent with the 125 GeV particle observed at CERN.

channel at 750 GeV [127,135], has not been observed in any other Higgs-decay-like channel and so is not relevant to our discussions. The $h_2 \to h_1 h_1$ channel may be visible as an excess in di-Higgs events at high mass, but in this model is an order of magnitude smaller than the $h_2 \to$ SM decays, and at present the LHC is not very sensitive to such processes and therefore it is difficult to place limits on this channel. There is an overwhelming QCD background for the dominant 4b decay; the $b\bar{b}\gamma\gamma$ channel is considered the most sensitive and so far has seen no excess but more data is required in order to expect a useful number of excess events.

In general, the strongest constraints on high mass decays come from consistency with the Higgs signal strength; for $M_H \lesssim 400\,\text{GeV}$ there are some competing constraints from CMS direct searches [134, 136] on the maximal branching of $h_2 \to$ SM, scaled by the maximal value of $\sin\theta$ at that mass point (i.e. giving then a constraint on the branching fraction with respect to an unscaled SM-like heavy Higgs boson).

Out of the six free parameters then – reduced to five when $M_{h1} = 125\,\text{GeV}$ is fixed – the only one that realistic constraints can currently be applied to is $\sin\theta$; $\mu_1, \lambda_1$ and $\lambda_2$ are inaccessible for the foreseeable future but if the $h_2 \to h_1 h_1$ decay were observed $\mu_1$ and $\lambda_2$ could be constrained. Some limits may be placed on $M_{h2}$, but only in a restricted region of the phase space.

It should be pointed out that all such studies are based on a simple rescaling of the SM cross sections, neglecting the $h_2 - h_1$ interference effects that will be considered in this chapter, however it is unlikely that these could be large enough to significantly affect limits.

In the study described here, model benchmark points with vanishing coupling parameters $\mu_1, \lambda_1$ and $\lambda_2$ are considered. ($\lambda_1 > 0$ is treated as approximately zero.) Reference [122] gives bounds on the $\lambda_1$ and $\mu_1$ parameters for $M_{h2} \lesssim 500$ GeV and a similar $\theta$, which are in agreement with the choice of zero for these parameters. It should be emphasised that the implementation in gg2VV is not restricted to benchmark points with vanishing $\mu_1, \lambda_1$ and $\lambda_2$. Nonzero values of $\mu_1, \lambda_1$ and $\lambda_2$ affect the calculation of the signal-background interference in the vector boson decays only via a change of the heavy Higgs width. In combination with FeynRules, the implementation in gg2VV therefore allows calculation of full signal-background interference effects for arbitrary

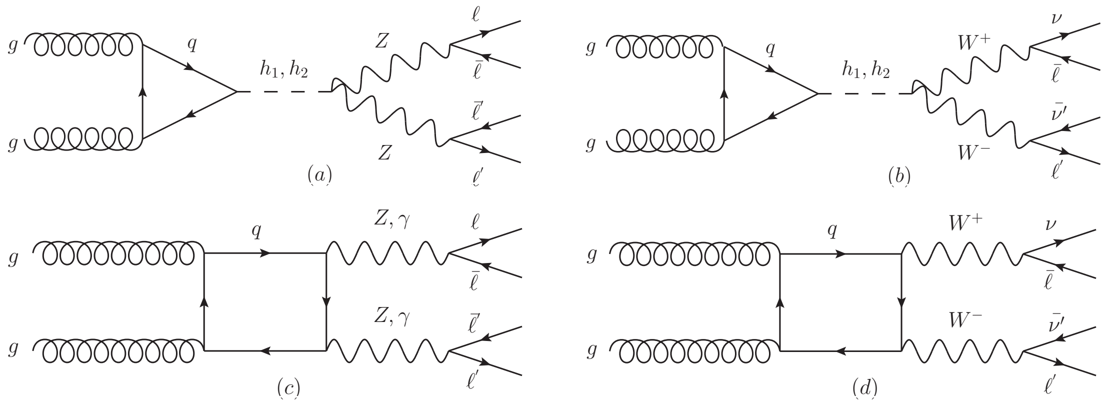

Figure 7.1: Representative Feynman diagrams for $gg\ (\to \{h_1, h_2\}) \to ZZ \to \ell\bar{\ell}\ell'\bar{\ell}'$ and $gg\ (\to \{h_1, h_2\}) \to WW \to \bar{\ell}\nu_\ell\ell'\bar{\nu_{\ell'}}$. The heavy Higgs ($h_2$) diagrams define the signal process, which interferes with the light Higgs ($h_1$) diagrams (a,b). They also interfere with the gluon-induced continuum background diagrams (c,d).

benchmark points of the general 1-Higgs-singlet extension of the SM, provided the user provides their own appropriate values of the $h_1$ and $h_2$ widths. It is noted that there is some tension between limits and the choice of the mixing angle $\theta = \pi/8$ giving a value of $\sin\theta \sim 0.38$, which is used for our three chosen mass points, but results are also given for the more realistic value of $\theta = \pi/15$ and it is illustrative to include the former benchmark mixing angle in order to compare the dependence of $h_2 - h_1$ interference effects on the mixing angle.

## 7.3 The Processes

Integrated and differential cross-section-level results are presented for the $h_2$ signal ($S$) and its interference ($I$) at the LHC for the processes

$$gg\ (\to \{h_1, h_2\}) \to Z(\gamma^*)Z(\gamma^*) \to \ell\bar{\ell}\ell'\bar{\ell}' \tag{7.15}$$

$$gg\ (\to \{h_1, h_2\}) \to W^-W^+ \to \ell\bar{\nu}\bar{\ell}'\nu' \tag{7.16}$$

Representative Feynman diagrams for the light and heavy Higgs and interfering continuum background processes are shown in figure 7.1. The heavy Higgs ($h_2$) diagrams define the signal process. They interfere with the light Higgs ($h_1$) diagrams and with the gluon-induced continuum background diagrams.

Table 7.1: Widths of the physical Higgs bosons $h_1$ and $h_2$ in the 1-Higgs-singlet extension of the SM with mixing angles $\theta = \pi/15$ and $\theta = \pi/8$ as well as $\mu_1 = \lambda_1 = \lambda_2 = 0$.

| | | $h_1$ | $h_2$ | | |
|---|---|---|---|---|---|
| | $M$ [GeV] | 125 | 300 | 600 | 900 |
| $\theta = \pi/15$ | $\Gamma$ [GeV] | $4.77358 \times 10^{-3}$ | 0.5383 | 6.42445 | 21.4215 |
| $\theta = \pi/8$ | $\Gamma$ [GeV] | $4.2577 \times 10^{-3}$ | 1.70204 | 20.7236 | 69.1805 |

A potential limitation of this study is that only leading order effects are considered. For a heavy Higgs boson, NLO corrections are expected to be large as suggested by [137], and it is conceivable that features in the higher order lineshapes will alter the total interference. However considering NLO calculations is beyond the capabilities of gg2VV, and in fact beyond the scope of all current tools, since an exact amplitude level background calculation is not yet available.

The study is presented from the point of view of considering the heavy Higgs-like resonance to be the signal, and deals with interference with the light Higgs and continuum backgrounds. A natural question is whether the existence of the heavier Higgs would cause notable effects on the lineshape or cross section of the *light* Higgs resonance, which may be seen in current studies of the newly discovered particle. However, there is no convincing reason to suppose that this may be the case; the SM predicts extremely large widths for the heavy resonance, which may extend its influence, but in general any extensions reduce this width, and in the case considered here the width even for the 900 GeV resonance is only 26 GeV, compared to the SM-only value of 320 GeV (from private FORTRAN code, HTO [138]). Furthermore, the light Higgs has features in its off-shell tail that lead to interference with overlapping backgrounds, but the cross sections for a high-mass Higgs are tiny in low-mass regions, so there is no real reason for there to be features of interest. Nonetheless some tests were performed in the early stages of this project with gg2VV, and unsurprisingly no deviations from the SM predictions were observed in the low mass region.

The Higgs boson widths are calculated using FeynRules for consistency. The used width values are given in table 7.1. All SM input parameters, PDF and settings choices are the same as those listed in section 6.2.1. A fixed-width Breit-Wigner propagator is employed for the weak bosons and the Higgs boson.

Minimal selection cuts are applied: $M_{\ell\bar{\ell}} > 4$ GeV and $M_{\ell'\bar{\ell}'} > 4$ GeV cuts are applied for the $gg \to Z(\gamma^*)Z(\gamma^*) \to \ell\bar{\ell}\ell'\bar{\ell}'$ process to eliminate the soft photon singularities. The renormalisation and factorisation scales are set to $M_{VV}/2$ and the $pp$ collision energy is $\sqrt{s} = 8$ TeV.

Cross sections for the continuum background and $h_1$-only contributions (without mixing, i.e. $\theta = 0$) to the processes considered here were found to be in agreement with the results of ref. [139], which were calculated using a previous version of gg2VV with a different phase space implementation based on a decomposition into sections. Furthermore, as discussed in Chapter 5, results for similar processes calculated using the same phase space code show excellent agreement with a fully independent implementation [8].

## 7.4 Results

$M_{h1}$ is set to 125 GeV in accordance with the mass of the observed resonance and three values are studied for the mass of the heavy Higgs resonance: $M_{h2} = 300$ GeV, $M_{h2} = 600$ GeV and $M_{h2} = 900$ GeV. The mixing angle $\theta$ is chosen so as not to alter the predicted light Higgs cross section too much.[3] To illustrate how interference effects change with the mixing angle, two values of $\theta$ are considered: $\theta = \pi/15$ and $\theta = \pi/8$.

The following notation is used:

$$S \sim |\mathcal{M}_{h2}|^2 \tag{7.17}$$

$$I_{h1} \sim 2\,\mathrm{Re}(\mathcal{M}_{h2}^*\,\mathcal{M}_{h1}) \tag{7.18}$$

$$I_{bkg} \sim 2\,\mathrm{Re}(\mathcal{M}_{h2}^*\,\mathcal{M}_{bkg}) \tag{7.19}$$

$$I_{full} = I_{h1} + I_{bkg} \tag{7.20}$$

$$R_i = \frac{S + I_i}{S}\,. \tag{7.21}$$

The interference of the heavy Higgs signal with the light Higgs and continuum background is given separately. The combined interference is also shown in order to illustrate the overall effect. The ratios $R_{h1}$, $R_{bkg}$ and $R_{full}$ illustrate the relative change of the heavy Higgs signal due to interference with the light Higgs and continuum background

---

[3] In fact the choice $\theta = \pi/8$ reduces the light Higgs cross section by approximately 30%, but it has already been noted that this shows some tension with limits.

Table 7.2: Cross sections for $gg\ (\to \{h_1, h_2\}) \to ZZ \to \ell\bar{\ell}\ell'\bar{\ell}'$ in $pp$ collisions at $\sqrt{s} = 8$ TeV at loop-induced leading order in the 1-Higgs-singlet extension of the SM with $M_{h1} = 125$ GeV, $M_{h2} = 300, 600, 900$ GeV and mixing angle $\theta = \pi/15$. Results for the heavy Higgs ($h_2$) signal ($S$) and its interference with the light Higgs ($I_{h1}$) and the continuum background ($I_{bkg}$) and the full interference ($I_{full}$) are given. The ratio $R_i = (S + I_i)/S$ illustrates the relative change of the heavy Higgs signal due to interference with the light Higgs and continuum background amplitude contributions. Minimal cuts are applied (see main text). Cross sections are given for a single lepton flavour combination. The integration error is displayed in brackets.

| $gg \to h_2 \to ZZ \to \ell\bar{\ell}\ell'\bar{\ell}'$<br>$\sigma$ [fb], $pp$, $\sqrt{s} = 8$ TeV<br>min. cuts, $\theta = \pi/15$ | | interference | | | ratio | | |
|---|---|---|---|---|---|---|---|
| $M_{h2}$ [GeV] | $S$ | $I_{h1}$ | $I_{bkg}$ | $I_{full}$ | $R_{h1}$ | $R_{bkg}$ | $R_{full}$ |
| 300 | 0.033453(7) | 0.00392(2) | 0.00105(2) | 0.00499(2) | 1.1171(6) | 1.0315(7) | 1.1492(6) |
| 600 | 0.005223(4) | -0.001738(8) | 0.001730(9) | -9(4)e-06 | 0.667(2) | 1.331(2) | 0.998(2) |
| 900 | 0.0005088(4) | -0.001151(2) | 0.001043(3) | -0.0001092(9) | -1.263(5) | 3.049(5) | 0.785(2) |

Table 7.3: Cross sections for $gg\ (\to \{h_1, h_2\}) \to ZZ \to \ell\bar{\ell}\ell'\bar{\ell}'$ in $pp$ collisions in the 1-Higgs-singlet extension of the SM with mixing angle $\theta = \pi/8$. Other details as in table 7.2.

| $gg \to h_2 \to ZZ \to \ell\bar{\ell}\ell'\bar{\ell}'$<br>$\sigma$ [fb], $pp$, $\sqrt{s} = 8$ TeV<br>min. cuts, $\theta = \pi/8$ | | interference | | | ratio | | |
|---|---|---|---|---|---|---|---|
| $M_{h2}$ [GeV] | $S$ | $I_{h1}$ | $I_{bkg}$ | $I_{full}$ | $R_{h1}$ | $R_{bkg}$ | $R_{full}$ |
| 300 | 0.12209(9) | 0.0119(1) | 0.00358(5) | 0.01545(4) | 1.097(2) | 1.029(2) | 1.127(2) |
| 600 | 0.01821(2) | -0.00498(2) | 0.00568(2) | 0.000694(8) | 0.727(2) | 1.312(2) | 1.038(2) |
| 900 | 0.001781(2) | -0.003277(5) | 0.003396(5) | 0.000118(3) | -0.840(3) | 2.906(4) | 1.066(2) |

amplitude contributions.

Integrated results for process (7.15) with minimal cuts are shown in tables 7.2 and 7.3 for mixing angles of $\theta = \frac{\pi}{15}$ and $\frac{\pi}{8}$ respectively and similarly those for process (7.16) are given in tables 7.4 and 7.5. As illustrated by the differential distributions shown below, a $|M_{VV} - M_{h2}| < \Gamma_{h2}$ window cut is an effective means to eliminate or mitigate the interference.[4] Therefore, integrated results with window cut are presented in tables 7.6 and 7.7 for process (7.15) and tables 7.8 and 7.9 for process (7.16). Figures 7.2 to 7.6 show the corresponding invariant mass distributions. Where appropriate, vertical dashed lines at $M_{VV} = M_{h2} \pm \Gamma_{h2}$ are used to visualise the effect of the $|M_{VV} - M_{h2}| < \Gamma_{h2}$ window cut. For invariant $VV$ masses with negative signal plus interference, the linear distributions are shown in figures 7.4 and 7.8 for comparison to the log scale version.

Finally, results are shown for the $4\ell$ final state at 13 TeV, calculated for ref. [9]. All input parameters and settings are given at the beginning of Chapter 8; the mixing angle

---

[4] For process (7.16), an invariant $M_{WW}$ cut cannot be applied experimentally. However, a transverse mass cut is feasible.

Table 7.4: Cross sections for $gg\ (\to \{h_1, h_2\}) \to W^-W^+ \to \ell\bar{\nu}\bar{\ell}'\nu'$ in $pp$ collisions at $\sqrt{s} = 8$ TeV in the 1-Higgs-singlet extension of the SM with $M_{h1} = 125$ GeV, $M_{h2} = 300, 600, 900$ GeV and mixing angle $\theta = \pi/15$. Other details as in table 7.2.

| $gg \to h_2 \to W^-W^+ \to \ell\bar{\nu}\bar{\ell}'\nu'$<br>$\sigma$ [fb], $pp$, $\sqrt{s} = 8$ TeV<br>min. cuts, $\theta = \pi/15$ | | interference | | | ratio | | |
|---|---|---|---|---|---|---|---|
| $M_{h2}$ [GeV] | $S$ | $I_{h1}$ | $I_{bkg}$ | $I_{full}$ | $R_{h1}$ | $R_{bkg}$ | $R_{full}$ |
| 300 | 0.3752(3) | 0.0391(9) | -0.0132(7) | 0.0254(5) | 1.104(3) | 0.965(3) | 1.068(2) |
| 600 | 0.05380(4) | -0.0191(2) | 0.0289(2) | 0.00957(8) | 0.645(3) | 1.536(4) | 1.178(2) |
| 900 | 0.005149(4) | -0.01217(6) | 0.01519(4) | 0.00300(3) | -1.36(2) | 3.950(9) | 1.582(5) |

Table 7.5: Cross sections for $gg\ (\to \{h_1, h_2\}) \to W^-W^+ \to \ell\bar{\nu}\bar{\ell}'\nu'$ in $pp$ collisions in the 1-Higgs-singlet extension of the SM with mixing angle $\theta = \pi/8$. Other details as in table 7.4.

| $gg \to h_2 \to W^-W^+ \to \ell\bar{\nu}\bar{\ell}'\nu'$<br>$\sigma$ [fb], $pp$, $\sqrt{s} = 8$ TeV<br>min. cuts, $\theta = \pi/8$ | | interference | | | ratio | | |
|---|---|---|---|---|---|---|---|
| $M_{h2}$ [GeV] | $S$ | $I_{h1}$ | $I_{bkg}$ | $I_{full}$ | $R_{h1}$ | $R_{bkg}$ | $R_{full}$ |
| 300 | 1.368(2) | 0.118(2) | -0.045(2) | 0.0712(9) | 1.086(2) | 0.967(2) | 1.052(2) |
| 600 | 0.1875(2) | -0.0548(3) | 0.0940(4) | 0.0389(3) | 0.708(2) | 1.501(3) | 1.207(2) |
| 900 | 0.01806(2) | -0.03467(8) | 0.0495(2) | 0.01478(7) | -0.920(5) | 3.742(7) | 1.818(5) |

Table 7.6: Cross sections for $gg\ (\to \{h_1, h_2\}) \to ZZ \to \ell\bar{\ell}\ell'\bar{\ell}'$ in $pp$ collisions at $\sqrt{s} = 8$ TeV in the 1-Higgs-singlet extension of the SM with $M_{h1} = 125$ GeV, $M_{h2} = 300, 600, 900$ GeV and mixing angle $\theta = \pi/15$. An additional window cut $|M_{ZZ} - M_{h2}| < \Gamma_{h2}$ is applied. Other details as in table 7.2.

| $gg \to h_2 \to ZZ \to \ell\bar{\ell}\ell'\bar{\ell}'$<br>$\sigma$ [fb], $pp$, $\sqrt{s} = 8$ TeV<br>min. cuts & $\lvert M_{VV} - M_{h2}\rvert < \Gamma_{h2}$<br>$\theta = \pi/15$ | | interference | | | ratio | | |
|---|---|---|---|---|---|---|---|
| $M_{h2}$ [GeV] | $S$ | $I_{h1}$ | $I_{bkg}$ | $I_{full}$ | $R_{h1}$ | $R_{bkg}$ | $R_{full}$ |
| 300 | 0.02352(2) | 3.8(4)e-06 | 0.001583(3) | 0.001586(3) | 1.000(2) | 1.067(2) | 1.067(2) |
| 600 | 0.003719(4) | -1.7(2)e-05 | 0.000288(2) | 0.000271(2) | 0.995(2) | 1.077(2) | 1.073(2) |
| 900 | 0.0003606(3) | -1.35(2)e-05 | 8.56(3)e-05 | 7.21(4)e-05 | 0.963(2) | 1.237(2) | 1.200(2) |

Table 7.7: Cross sections for $gg\ (\to \{h_1, h_2\}) \to ZZ \to \ell\bar{\ell}\ell'\bar{\ell}'$ in $pp$ collisions in the 1-Higgs-singlet extension of the SM with mixing angle $\theta = \pi/8$. Other details as in table 7.6.

| $gg \to h_2 \to ZZ \to \ell\bar{\ell}\ell'\bar{\ell}'$<br>$\sigma$ [fb], $pp$, $\sqrt{s} = 8$ TeV<br>min. cuts & $\lvert M_{VV} - M_{h2}\rvert < \Gamma_{h2}$<br>$\theta = \pi/8$ | | interference | | | ratio | | |
|---|---|---|---|---|---|---|---|
| $M_{h2}$ [GeV] | $S$ | $I_{h1}$ | $I_{bkg}$ | $I_{full}$ | $R_{h1}$ | $R_{bkg}$ | $R_{full}$ |
| 300 | 0.08537(8) | 3.6(4)e-05 | 0.005371(9) | 0.00541(1) | 1.000(2) | 1.063(2) | 1.063(2) |
| 600 | 0.01323(2) | -0.000174(4) | 0.001058(4) | 0.000884(6) | 0.987(2) | 1.080(2) | 1.067(2) |
| 900 | 0.001283(1) | -0.0001316(9) | 0.000373(1) | 0.000241(2) | 0.897(2) | 1.290(2) | 1.188(2) |

Table 7.8: Cross sections for $gg$ $(\to \{h_1, h_2\}) \to W^-W^+ \to \ell\bar{\nu}\bar{\ell}'\nu'$ in $pp$ collisions at $\sqrt{s} = 8$ TeV in the 1-Higgs-singlet extension of the SM with $M_{h1} = 125$ GeV, $M_{h2} = 300, 600, 900$ GeV and mixing angle $\theta = \pi/15$. An additional window cut $|M_{WW} - M_{h2}| < \Gamma_{h2}$ is applied. Other details as in table 7.4.

| $gg \to h_2 \to W^-W^+ \to \ell\bar{\nu}\bar{\ell}'\nu'$<br>$\sigma$ [fb], $pp$, $\sqrt{s} = 8$ TeV<br>min. cuts & $\|M_{VV} - M_{h2}\| < \Gamma_{h2}$<br>$\theta = \pi/15$ | | interference | | | ratio | | |
|---|---|---|---|---|---|---|---|
| $M_{h2}$ [GeV] | $S$ | $I_{h1}$ | $I_{bkg}$ | $I_{full}$ | $R_{h1}$ | $R_{bkg}$ | $R_{full}$ |
| 300 | 0.3352(3) | 3.8(6)e-05 | 0.00959(6) | 0.00963(7) | 1.000(2) | 1.029(2) | 1.029(2) |
| 600 | 0.04859(5) | -0.000188(4) | 0.00419(3) | 0.00401(3) | 0.996(2) | 1.086(2) | 1.082(2) |
| 900 | 0.004635(5) | -0.000137(3) | 0.000929(5) | 0.000792(5) | 0.970(2) | 1.200(2) | 1.171(2) |

Table 7.9: Cross sections for $gg$ $(\to \{h_1, h_2\}) \to W^-W^+ \to \ell\bar{\nu}\bar{\ell}'\nu'$ in $pp$ collisions in the 1-Higgs-singlet extension of the SM with mixing angle $\theta = \pi/8$. Other details as in table 7.8.

| $gg \to h_2 \to W^-W^+ \to \ell\bar{\nu}\bar{\ell}'\nu'$<br>$\sigma$ [fb], $pp$, $\sqrt{s} = 8$ TeV<br>min. cuts & $\|M_{VV} - M_{h2}\| < \Gamma_{h2}$<br>$\theta = \pi/8$ | | interference | | | ratio | | |
|---|---|---|---|---|---|---|---|
| $M_{h2}$ [GeV] | $S$ | $I_{h1}$ | $I_{bkg}$ | $I_{full}$ | $R_{h1}$ | $R_{bkg}$ | $R_{full}$ |
| 300 | 0.9578(9) | 0.00034(2) | 0.0324(2) | 0.0329(2) | 1.000(2) | 1.034(2) | 1.034(2) |
| 600 | 0.1361(2) | -0.00184(2) | 0.01578(6) | 0.01394(3) | 0.987(2) | 1.116(2) | 1.102(2) |
| 900 | 0.01298(1) | -0.001340(7) | 0.00429(2) | 0.002952(7) | 0.897(2) | 1.331(2) | 1.227(2) |

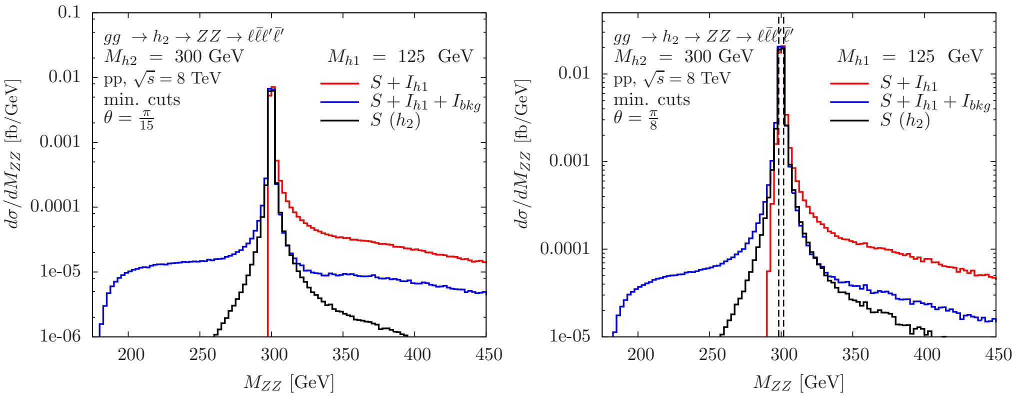

Figure 7.2: Invariant $ZZ$ mass distributions for $gg$ $(\to \{h_1, h_2\}) \to ZZ \to \ell\bar{\ell}\ell'\bar{\ell}'$ in $pp$ collisions at $\sqrt{s} = 8$ TeV at loop-induced leading order in the 1-Higgs-singlet extension of the SM with $M_{h1} = 125$ GeV, $M_{h2} = 300$ GeV and mixing angles $\theta = \pi/15$ and $\pi/8$. Results for the heavy Higgs ($h_2$) signal ($S$) and including interference with the light Higgs ($S + I_{h1}$) and the continuum background ($S + I_{h1} + I_{bkg}$) are shown. Minimal cuts are applied (see main text). Other details as in table 7.2.

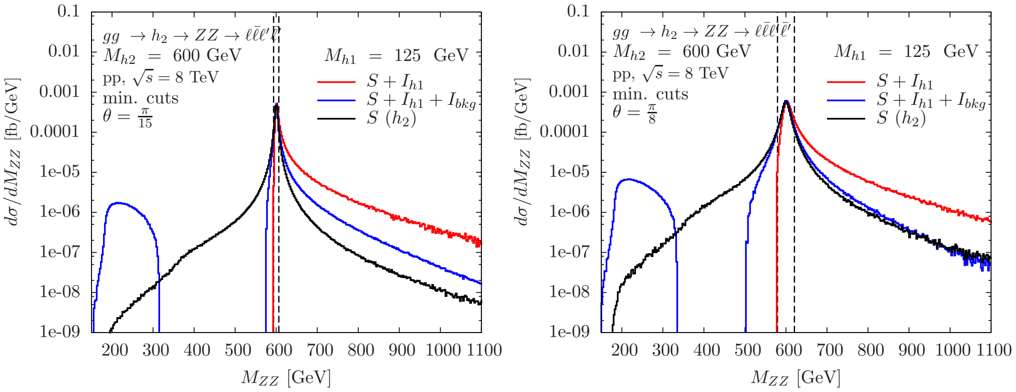

Figure 7.3: Invariant $ZZ$ mass distributions for $gg\ (\to \{h_1, h_2\}) \to ZZ \to \ell\bar{\ell}\ell'\bar{\ell}'$ in $pp$ collisions at $\sqrt{s} = 8$ TeV in the 1-Higgs-singlet extension of the SM with $M_{h1} = 125$ GeV, $M_{h2} = 600$ GeV and mixing angles $\theta = \pi/15$ and $\pi/8$. Other details as in figure 7.2.

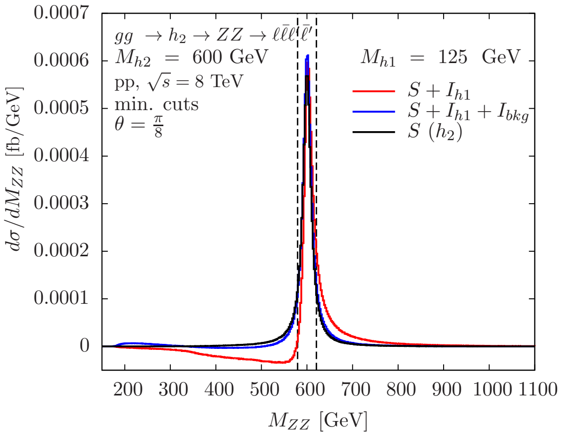

Figure 7.4: Invariant $ZZ$ mass distributions for $gg(\to \{h_1, h_2\}) \to ZZ \to \ell\bar{\ell}\ell'\bar{\ell}'$ in $pp$ collisions in the 1-Higgs-singlet extension of the SM with mixing angle $\theta = \pi/8$. As in figure 7.3, but with linear $d\sigma/dM_{ZZ}$ scale, to illustrate negative $S + I_{h1}$ and $S + I_{h1} + I_{bkg}$.

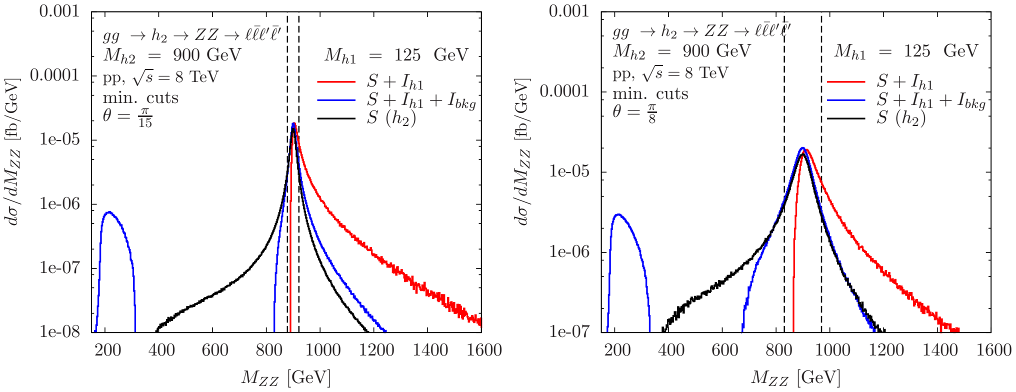

Figure 7.5: Invariant $ZZ$ mass distributions for $gg\ (\to \{h_1, h_2\}) \to ZZ \to \ell\bar{\ell}\ell'\bar{\ell}'$ in $pp$ collisions at $\sqrt{s} = 8$ TeV in the 1-Higgs-singlet extension of the SM with $M_{h1} = 125$ GeV, $M_{h2} = 900$ GeV and mixing angles $\theta = \pi/15$ and $\theta = \pi/8$. Other details as in figure 7.2.

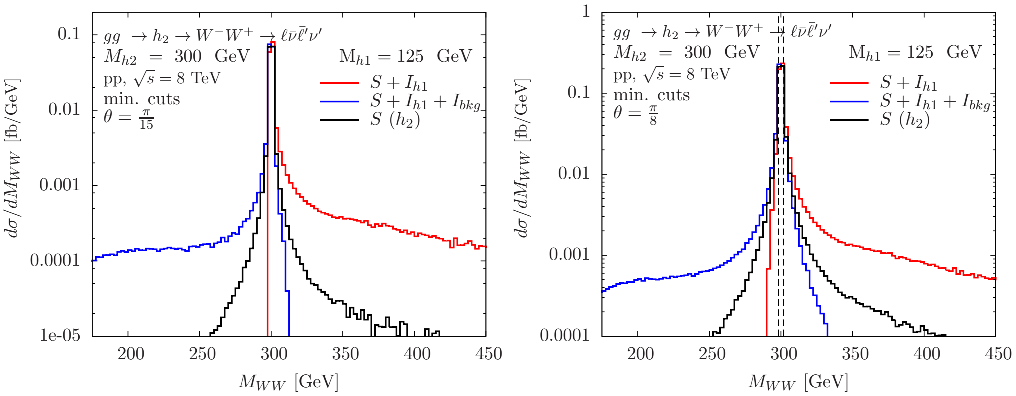

Figure 7.6: Invariant $WW$ mass distributions for $gg(\to \{h_1, h_2\}) \to W^-W^+ \to \ell\bar{\nu}\bar{\ell}'\nu'$ in $pp$ collisions at $\sqrt{s} = 8$ TeV in the 1-Higgs-singlet extension of the SM with $M_{h1} = 125$ GeV, $M_{h2} = 300$ GeV and mixing angles $\theta = \pi/15$ and $\pi/15$. Other details as in table 7.4.

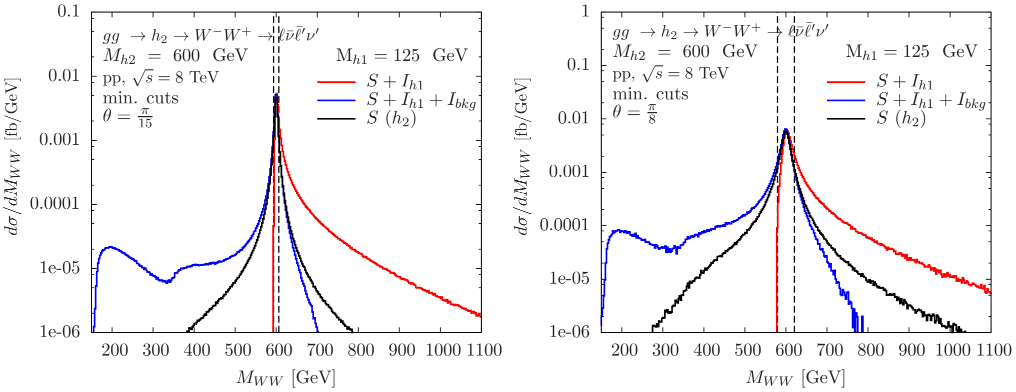

Figure 7.7: Invariant $WW$ mass distributions for $gg$ $(\to \{h_1, h_2\}) \to W^-W^+ \to \ell\bar{\nu}\bar{\ell}'\nu'$ in $pp$ collisions at $\sqrt{s} = 8$ TeV in the 1-Higgs-singlet extension of the SM with $M_{h1} = 125$ GeV, $M_{h2} = 600$ GeV and mixing angles $\theta = \pi/15$ and $\pi/8$. Other details as in figure 7.6.

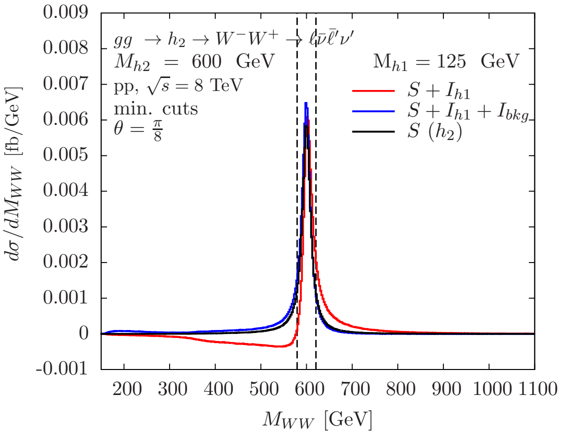

Figure 7.8: Invariant $WW$ mass distributions for $gg$ $(\to \{h_1, h_2\}) \to W^-W^+ \to \ell\bar{\nu}\bar{\ell}'\nu'$ in $pp$ collisions in the 1-Higgs-singlet extension of the SM with mixing angle $\theta = \pi/8$. As in figure 7.7, but with linear $d\sigma/dM_{WW}$ scale, to illustrate negative $S + I_{h1}$.

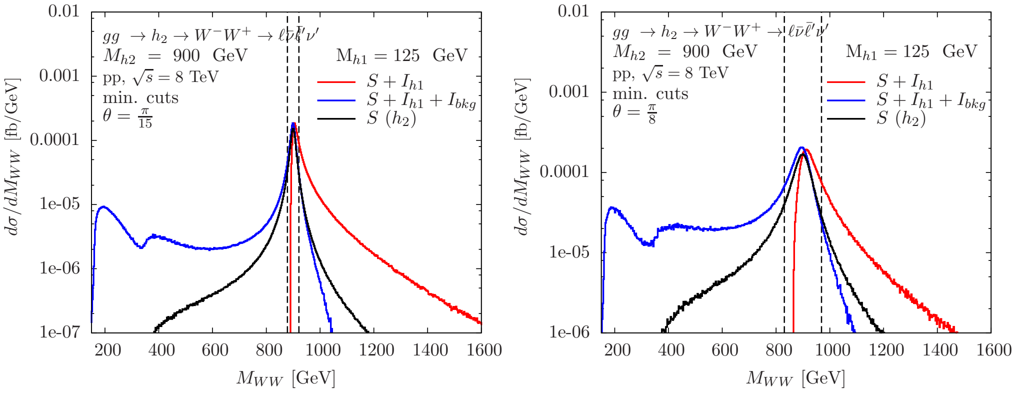

Figure 7.9: Invariant $WW$ mass distributions for $gg\ (\to \{h_1, h_2\}) \to W^-W^+ \to \ell\bar{\nu}\bar{\ell}'\nu'$ in $pp$ collisions at $\sqrt{s} = 8$ TeV in the 1-Higgs-singlet extension of the SM with $M_{h1} = 125$ GeV, $M_{h2} = 900$ GeV and mixing angle $\theta = \pi/15$ and $\pi/8$. Other details as in figure 7.6.

Table 7.10: Widths of the physical Higgs bosons $h_1$ and $h_2$ in the 1-Higgs-singlet extension of the SM with mixing angles $\sin\theta = 0.2$ and $\sin\theta = 0.4$ as well as $\mu_1 = \lambda_1 = \lambda_2 = 0$.

| | | $h_1$ | $h_2$ | | |
|---|---|---|---|---|---|
| $\sin\theta$ | $M$ [GeV] | 125 | 400 | 600 | 900 |
| 0.2 | $\Gamma$ [GeV] | $4.34901 \times 10^{-3}$ | 1.52206 | 5.95419 | 19.8529 |
| 0.4 | $\Gamma$ [GeV] | $3.80539 \times 10^{-3}$ | | 22.5016 | |

is chosen so that $\sin(\theta) = 0.2$ for the majority of results but results are additionally provided for $\sin(\theta) = 0.4$ and $M_H = 600\,\text{GeV}$ in order to quantify the mixing angle dependence. In this case, the minimal cuts are $M_{ZZ} > 10$ GeV, and no cut for $M_{WW}$. The recalculated widths are given in table 7.10. In addition to table 7.11, which displays results in the same format as those above, results including the full gg background are shown in table 7.12. The corresponding invariant mass plots are shown in figure 7.10 and figure 7.11.

## 7.5 Discussion

As seen in the tables and figures, interference effects increase significantly with increasing heavy Higgs mass. They can range from $\mathcal{O}(1)$ to $\mathcal{O}(10\%)$ effects for integrated cross sections. With the window cut, it can be seen that interference effects are mitigated to $\mathcal{O}(10\%)$ or less. It is also noticeable that the heavy Higgs-continuum background interference is negative above $M_{h2}$ and positive below $M_{h2}$, while the heavy Higgs-light Higgs

Table 7.11: Cross sections for $gg\ (\to \{h_1, h_2\}) \to ZZ \to \ell\bar{\ell}\ell'\bar{\ell}'$ in $pp$ collisions at $\sqrt{s} = 13\,\text{TeV}$ at loop-induced leading order in the 1-Higgs-singlet extension of the SM with $M_{h1} = 125\text{GeV}$, $M_{h2} = 400, 600, 900\,\text{GeV}$ and mixing angle $\sin\theta = 0.2$ or $0.4$ as indicated. The ratio $R_i = (S + I_i)/S$ illustrates the relative change of the heavy Higgs signal due to interference with the light Higgs and continuum background amplitude contributions. Cross sections are given for a single lepton flavour combination. The integration error is displayed in brackets.

| $gg(\to \{h_1, h_2\}) \to ZZ \to \ell\bar{\ell}\ell'\bar{\ell}'$ $\sigma$ [fb], $pp$, $\sqrt{s} = 13\,\text{TeV}$ min. cuts | | | interference | | | ratio | | |
|---|---|---|---|---|---|---|---|---|
| $\sin\theta$ | $M_{h2}$ [GeV] | $S(h_2)$ | $I_{h1}$ | $I_{bkg}$ | $I_{full}$ | $R_{h1}$ | $R_{bkg}$ | $R_{full}$ |
| 0.2 | 400 | 0.07412(6) | 0.00682(6) | -0.00171(2) | 0.00511(6) | 1.092(2) | 0.977(1) | 1.069(2) |
| 0.2 | 600 | 0.01710(2) | -0.00369(3) | 0.00384(3) | 0.00015(4) | 0.784(2) | 1.225(2) | 1.009(3) |
| 0.2 | 900 | 0.002219(2) | -0.003369(9) | 0.003058(8) | -0.00031(2) | -0.518(4) | 2.378(4) | 0.860(6) |
| 0.4 | 600 | 0.07065(6) | -0.01191(6) | 0.01465(6) | -0.00274(9) | 0.831(2) | 1.207(2) | 1.039(2) |

Table 7.12: Cross sections for $gg\ (\to \{h_1, h_2\}) \to ZZ \to \ell\bar{\ell}\ell'\bar{\ell}'$ in $pp$ collisions at $\sqrt{s} = 13$ TeV at loop-induced leading order in the 1-Higgs-singlet extension of the SM with $M_{h1} = 125$ GeV, $M_{h2} = 400, 600, 900$ GeV and mixing angle $\sin\theta = 0.2$ or $0.4$ as indicated. Results for the heavy Higgs ($h_2$) signal ($S$), light Higgs background ($h_1$) and continuum background (gg bkg). Where more than one contribution is indicated, all interferences are taken into account. Other details are as in Table 7.11.

| $gg \to h_2 \to ZZ \to \ell\bar{\ell}\ell'\bar{\ell}'$ $\sigma$ [fb], $LHC$, $\sqrt{s} = 13$ TeV min. cuts | | | | | | |
|---|---|---|---|---|---|---|
| $\sin\theta$ | $M_{h2}$ [GeV] | $S(h_2)$ | $h_1$ | gg bkg. | $S(h_2)$ + $h_1$ + $I_{h1}$ | all |
| 0.2 | 400 | 0.07412(6) | 0.854(2) | 21.18(7) | 0.934(2) | 21.86(7) |
| 0.2 | 600 | 0.01710(2) | 0.854(2) | 21.18(7) | 0.867(2) | 21.80(7) |
| 0.2 | 900 | 0.002219(2) | 0.854(2) | 21.18(7) | 0.852(2) | 21.79(7) |
| 0.4 | 600 | 0.07065(6) | 0.734(2) | 21.18(7) | 0.793(2) | 21.77(7) |

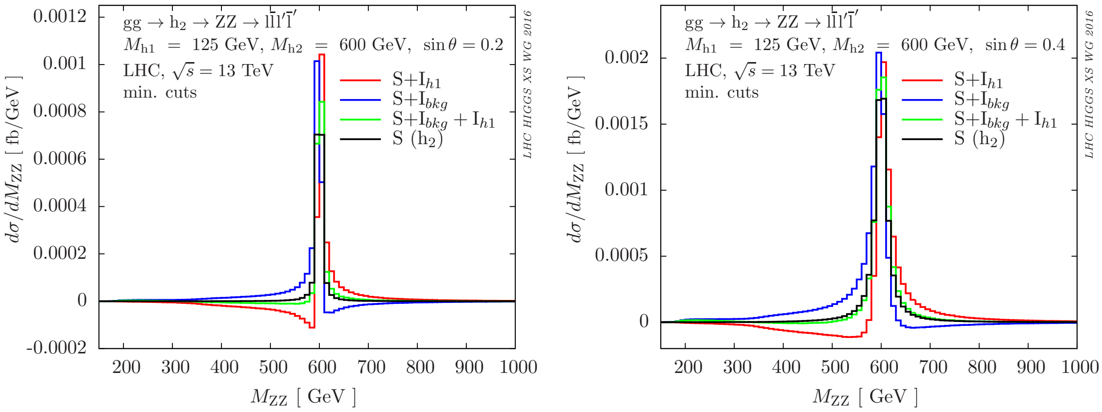

Figure 7.10: Invariant mass distributions for $gg\ (\to \{h_1, h_2\}) \to ZZ \to \ell\bar{\ell}\ell'\bar{\ell}''$, other details as in Table 7.11.

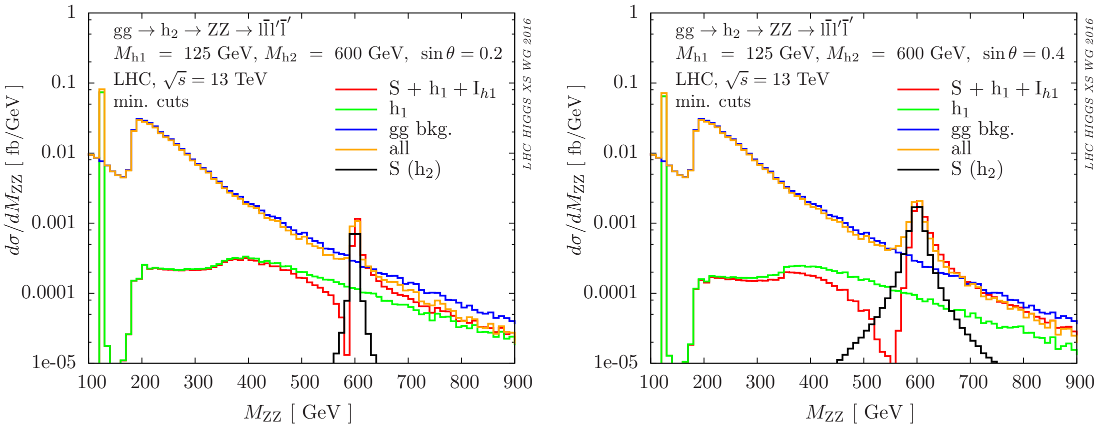

Figure 7.11: Invariant mass distributions for $gg\ (\to \{h_1, h_2\}) \to ZZ \to \ell\bar{\ell}\ell'\bar{\ell}'$, other details as in Table 7.12. Where more than one contribution is included, all interferences are taken into account.

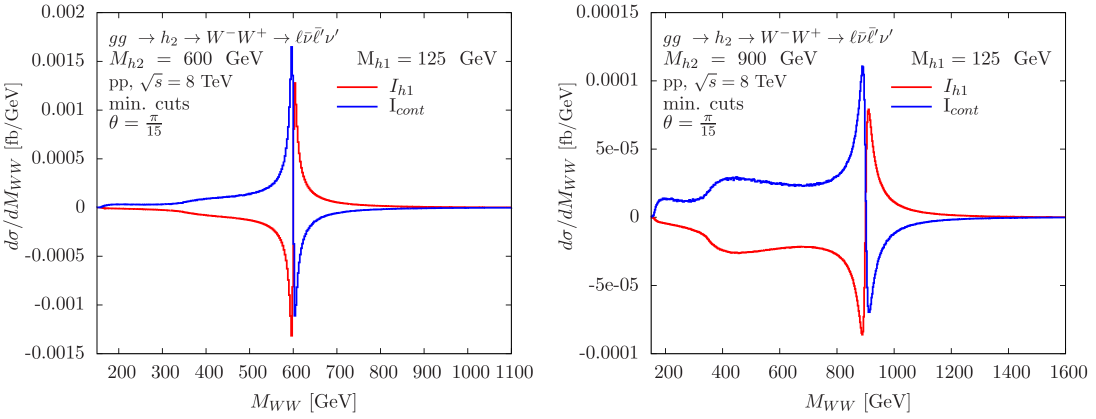

Figure 7.12: As figures 7.7 and 7.9 (left-hand plots), with the interference contributions only on a linear scale.

interference has the opposite behaviour. Consequently, in the heavy Higgs resonance region a strong cancellation occurs when both interference contributions are added. It is therefore essential to take both contributions into account in phenomenological and experimental studies.

Despite the occurring cancellation, the full interference is clearly non-negligible and modifies the heavy Higgs lineshape. Overall effects of $\mathcal{O}(10\%)$ are found for integrated cross sections, even if a window cut is applied. The results for $\theta = \pi/15$ and $\theta = \pi/8$ are in qualitative agreement. Relative interference effects show a mild quantitative dependence on the mixing angle.

The interference contributions for the 600 and 900 GeV Higgs in the $WW$ case are separated in figure 7.12. It is striking that the differing contributions are roughly symmetric in size and shape, so that, as can in the tables, the total effect on the cross section is small. The same features that were visible in the semi-leptonic cases discussed in Chapter 6, enhancements in interference at $2M_t$ and $2M_V$ (although the numerical values at these points are still very small), are again visible here, and above the heavy Higgs peak there are no striking features. The sign flip in both contributions as the interference goes through the peak suggests that the real part of the product (as in eq. (6.17)) dominates in this region. The imaginary component is enhanced by direct proportionality to the larger width of the heavy resonances, and therefore has an impact even so far from the peak. The continuum interference is destructive above the mass peak.

The results presented for heavy Higgs-light Higgs interference are qualitatively in agreement with those given in ref. [69], where this interference is considered for $gg \to \{h_1, h_2\} \to ZZ \to 4\ell$, but in the 1HSM with an extra $Z_2$ symmetry.

From a phenomenological perspective, it is also useful to study figure 7.11, in order to see the change in combined signal and background when interference is or is not included. It was seen when studying interference alone that the combined light and continuum interferences cancel each other out to an extent, so that the overall effect is small: when one includes the full gg background, the effect is rendered even less important since the signal is only distinguishable above the background close to the peak, and it is in this region that the cancellation is strongest. Note also that away from the heavy peak, the $h_1$ only line is indistinguishable form the $S + h_1 + I_{h1}$ line, verifying the earlier assertion that the presence of the heavy resonance has a negligible effect on the lineshape of the light resonance.

# Chapter 8

# Off-shell Comparisons in Leptonic Higgs Decays

Throughout this chapter, all parameters are chosen according to the recommendations of the LHC Higgs Cross Section Working Group for the fourth yellow report [9]: $M_W = 80.35797\,\text{GeV}$, $M_Z = 91.15348\,\text{GeV}$, $\Gamma_W = 2.08430\,\text{GeV}$, $\Gamma_Z = 2.49427\,\text{GeV}$, $M_t = 172.5\,\text{GeV}$, $M_b(M_b) = 4.18\,\text{GeV}$, $G_F = 1.1663787\,.\,10^{-5}\text{GeV}^{-2}$, $V_{CKM} = 1$. Unless otherwise indicated, $\mu_R = \mu_F = \frac{M_{VV}}{2}$ and the PDF set is PDF4LHC15_nlo_100 with the default $\alpha_s$.

## 8.1 Interference Effects in Fully Leptonic Vector Boson Decays of the Higgs Boson

The five fully leptonic decays of the SM Higgs boson produced from gluon fusion are:

$$gg \to H \to W^-W^+ \to \ell\bar{\nu}_\ell\bar{\nu'}_\ell\ell' \tag{8.1}$$

$$gg \to H \to ZZ \to \ell\bar{\ell}\ell'\bar{\ell'} \tag{8.2}$$

$$gg \to H \to ZZ \to \ell\bar{\ell}\ell\bar{\ell} \tag{8.3}$$

$$gg \to H \to ZZ \to \bar{\ell}\ell\bar{\nu'}_\ell\nu'_\ell \tag{8.4}$$

$$gg \to H \to W^+W^-/ZZ \to \bar{\ell}\nu\bar{\nu}\ell \tag{8.5}$$

Table 8.1: Integrated cross section results for gluon fusion leptonic processes. Results are given for signal + interference with gg background, and gg background only.

$gg \to H \to VV \to$ final states
$\sigma$ [fb], $LHC$, $\sqrt{s} = 13\,\text{TeV}$
min. cuts

| Final State | $S$ | S+$I_{ggbkg}$ | gg bkg. |
|---|---|---|---|
| $\ell\nu_\ell\bar{\nu}_\ell{}'\ell'$ | 37.95(4) | 33.60(4) | 45.31(4) |
| $\ell\bar{\ell}\ell'\bar{\ell}'$ | 0.9284(7) | 0.6707(8) | 4.264(2) |
| $\ell\bar{\ell}\ell\bar{\ell}$ | 0.4739(8) | 0.3467(8) | 1.723(3) |
| $\bar{\ell}\ell\bar{\nu}'\nu'$ | 1.896(2) | 1.386(2) | 5.730(5) |
| $\bar{\ell}\nu\bar{\nu}\ell$ | 36.01(3) | 31.19(3) | 50.52(4) |

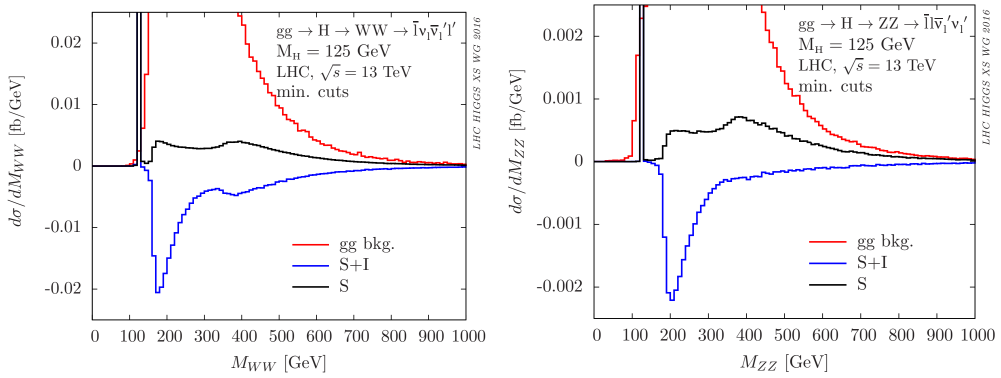

Figure 8.1: Invariant mass distributions for $gg\ (\to H) \to W^+W^- \to \bar{\ell}\nu_\ell\bar{\nu}_\ell'\ell'$ and $gg\ (\to H) \to ZZ \to \bar{\ell}\ell\bar{\nu}_\ell'\nu_\ell'$

A BSM extension of processes (8.1) and (8.2) was studied in Chapter 7.

These processes are well-studied in the literature, as are their interference effects, particularly in refs. [59, 60, 63, 65, 79, 139]. Experimental analyses at the LHC have been performed by ATLAS [140, 141] and CMS [142, 143]. The results included here were calculated using gg2VV for the yellow report that is currently in preparation [9]. Results were compared with VBFNLO and MadGraph5_aMC@NLO. Table 8.1 shows the integrated cross sections for the five processes with parameters as given above and minimal cuts ($M_{\ell\bar{\ell}} > 10\,\text{GeV}$ for all same flavour lepton combinations). Figures 8.1 to 8.3 show the corresponding $M_{VV}$ differential distributions.

While calculating these results, the importance of exactly how the interference results are calculated became apparent. The default set-up of the main gg2VV code is to calculate signal only, background only or signal + background including interference,

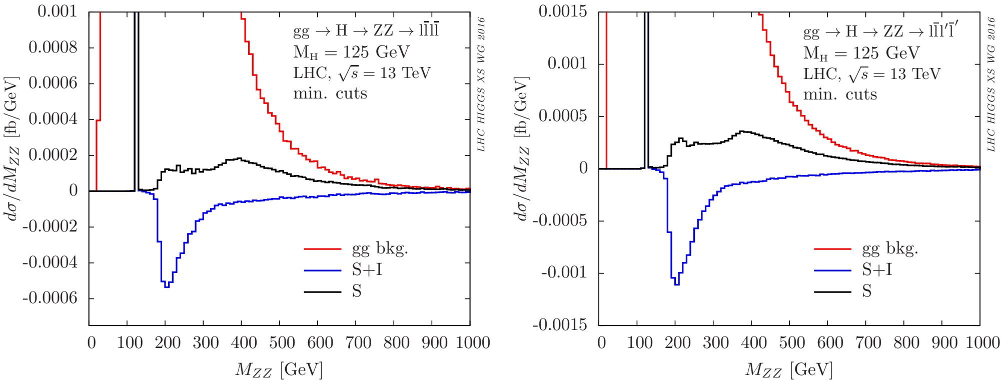

Figure 8.2: Invariant mass distributions for $gg\ (\to H) \to ZZ \to \ell\bar{\ell}\ell\bar{\ell}$ and $gg\ (\to H) \to ZZ \to \ell\bar{\ell}\ell'\bar{\ell}'$.

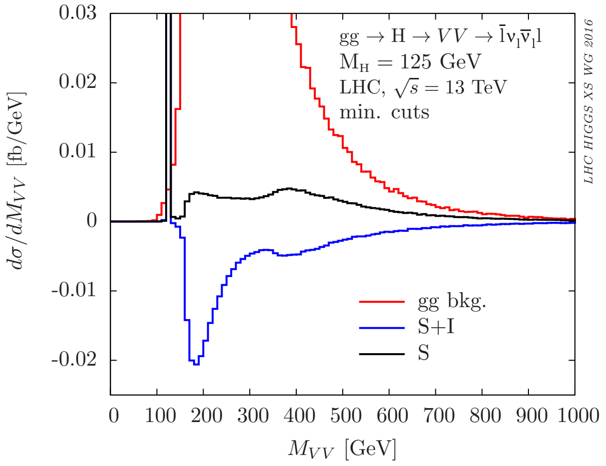

Figure 8.3: Invariant mass distribution for $gg\,(\to H) \to W^+W^-/ZZ \to \bar{\ell}\nu_\ell\bar{\nu}_\ell\ell$.

so the only way to separate the interference contribution is to subtract the signal-only and background-only results from the signal + background + interference result. Alternatively, one can calculate the interference contribution alone. It is to be expected that the second method (which will be referred to as the direct calculation, and the subtraction method as the indirect calculation) will be more accurate, since if the interference contribution is isolated, the grid adaptation focuses on regions of the phase space most relevant to the interference, which is not necessarily the case when the squared signal/background contributions (which will typically be much larger than the interference and therefore drive the adaptation) are included.

In fact, although four out of the five cases showed the expected agreement, with better precision on the direct interference calculation, in one case, process (8.5), it proved difficult to get a sufficiently precise result using the indirect calculation, and comparison of the invariant mass differential distributions (figure 8.4) showed that this method missed a crucial cancellation in the on-peak region in one particular bin, where although the two results to be subtracted individually had a precision of better than 1%, this was not precise enough to include the required cancellation. Error propagation showed that the error on the indirect calculation was greater than 100%, so this issue could not go un-noticed, but it is interesting to note. If higher precision was required on the indirect calculation in this case, it would be necessary to perform runs with a cut around the problematic region to ensure that a large number of phase space points are sampled in that region.

The conclusions to be drawn from these results are those of ref. [139] and the other references cited above: interference effects in the SM fully-leptonic decays are of order 10% and are more important in the off-peak regions. The total signal-background interference with minimal cuts is destructive in all cases.

## 8.2 Comparisons of PDF and Scale Choices

A relevant topic is the optimal renormalisation and factorisation scales, and the choice of PDF. Ideally, the dependence of the cross section on the scale choices should be as small as possible, and it is sensible to choose scales of the order of the energy scale of the

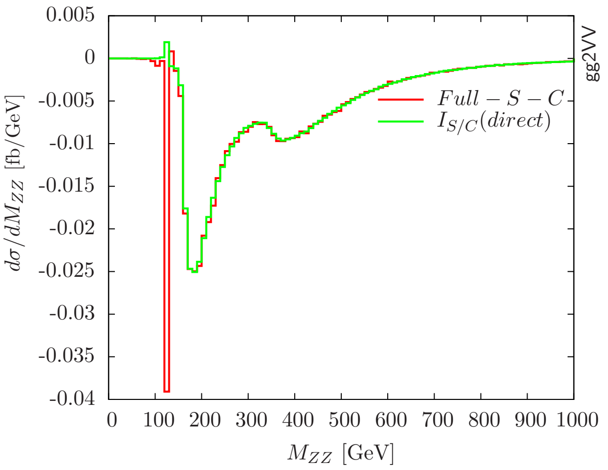

Figure 8.4: Invariant mass distribution for $gg\,(\to H) \to W^+W^-/ZZ \to \bar{\ell}\nu_\ell\bar{\nu}_\ell\ell$ comparing signal + interference calculated directly and indirectly.

process under consideration in order to minimise logarithms of the form $\ln\frac{Q^2}{\mu_f^2}$ and $\ln\frac{\mu_r^2}{Q^2}$ in the structure functions in the DGLAP evolution of the PDF and QCD corrections to the cross section. If these logarithms were allowed to be large, the convergence of the power series would be spoilt. Then, for example, for the $gg \to 4\ell$ process $M_{4\ell}$ is a reasonable choice, although in fact better convergence of the QCD perturbative series is found for $\mu = M_{4\ell}/2$.

A further question is the order of PDF set to use. As discussed in Chapter 3, the DGLAP equations are known to NNLO, and so in principle the evolution used to obtain the requested probability value can be LO, NLO, or NNLO. It is reasonable to ask whether, if the hard process can only be calculated to say leading order, as is the case with many gluon fusion processes, one should convolute this with the best available NNLO PDF or use the lower order set for consistency. If one takes the recommended value of $\alpha_s\,(\mu)$ at the requested factorisation scale, there is further variation in whether $\alpha_s$ is calculated using the best available (NNLO) renormalisation group equation prediction, or whether the order matches that of the DGLAP equation.

Brief investigations into scale dependence (tables 8.4 and 8.5) and PDF set dependence (tables 8.2 and 8.3) are presented for the $gg \to H \to 2\ell2\ell'$ process, considering the effect on signal, signal-plus-interference and background-only in the resonant ($110\,\text{GeV} < M_{VV} < 140\,\text{GeV}$, denoted “RES”) and off-shell ($M_{VV} > 140\,\text{GeV}$) regions,

Table 8.2: PDF dependence of off-shell $gg\ (\to H) \to e^+e^-\mu^+\mu^-$ cross sections at LO in fb. Minimal cuts, described in the text, are applied. $R$ is the ratio of the NNLO or LO result to NLO result. The bottom rows show the ratio of OFS, HM1, HM2 to RES result for $S$ and $S+I$. The MC error is given in brackets. See main text for other details.

| | | PDF set order | | | | | | |
|---|---|---|---|---|---|---|---|---|
| Region | Amp. | **NLO** | NNLO | $R$ | LO(0.118) | $R$ | LO(0.130) | $R$ |
| | $S$ | 0.1266(1) | 0.1255(1) | 0.991(2) | 0.1255(1) | 0.992(2) | 0.1414(2) | 1.116(2) |
| OFS | $S+I$ | −0.1313(2) | −0.1298(2) | 0.988(2) | −0.1307(2) | 0.995(2) | −0.149(1) | 1.138(8) |
| | $B$ | 2.988(4) | 2.945(5) | 0.986(2) | 2.960(4) | 0.991(2) | 3.448(5) | 1.154(3) |
| | $S$ | 0.01933(4) | 0.01906(4) | 0.986(3) | 0.01899(4) | 0.982(3) | 0.02210(5) | 1.143(4) |
| HM1 | $S+I$ | −0.04550(8) | −0.04475(8) | 0.984(3) | −0.04486(7) | 0.986(3) | −0.0516(6) | 1.13(2) |
| | $B$ | 1.182(3) | 1.165(3) | 0.985(3) | 1.166(3) | 0.986(3) | 1.354(3) | 1.145(4) |
| | $S$ | 0.0981(1) | 0.0974(1) | 0.993(2) | 0.0973(1) | 0.992(2) | 0.1084(2) | 1.105(2) |
| HM2 | $S+I$ | −0.0465(1) | −0.04622(9) | 0.994(3) | −0.04637(9) | 0.997(3) | −0.0522(6) | 1.12(2) |
| | $B$ | 0.611(2) | 0.605(2) | 0.990(4) | 0.598(2) | 0.980(4) | 0.676(2) | 1.107(5) |
| | $S$ | 0.800(1) | 0.780(1) | 0.976(2) | 0.843(1) | 1.054(2) | 1.021(2) | 1.276(3) |
| RES | $S+I$ | 0.803(2) | 0.784(2) | 0.976(4) | 0.845(4) | 1.052(6) | 1.023(3) | 1.274(5) |
| | $B$ | 0.1092(2) | 0.1063(2) | 0.974(2) | 0.1150(2) | 1.053(3) | 0.1389(2) | 1.272(3) |
| OFS/ | $S$ | 0.1583(3) | 0.1609(3) | | 0.1490(3) | | 0.1385(3) | |
| RES | $S+I$ | −0.1635(4) | −0.1655(5) | | −0.1547(7) | | −0.146(2) | |
| HM1/ | $S$ | 0.02418(6) | 0.02443(6) | | 0.02253(6) | | 0.02165(5) | |
| RES | $S+I$ | −0.0566(2) | −0.0571(2) | | −0.0531(3) | | −0.0504(6) | |
| HM2/ | $S$ | 0.1227(2) | 0.1249(3) | | 0.1155(2) | | 0.1062(2) | |
| RES | $S+I$ | −0.0579(2) | −0.0589(2) | | −0.0549(3) | | −0.0510(6) | |

with the off-shell region (OFS) further divided into the region with known enhancements such as on-shell top effects (HM1, $140\,\mathrm{GeV} < M_{VV} < 300\,\mathrm{GeV}$), and the remaining high mass region (HM2, $M_{VV} > 300\,\mathrm{GeV}$). Two sets of cuts are considered: minimal cuts ($M_{\ell\bar{\ell}} > 4\,\mathrm{GeV}$ to avoid the photon singularity in the background) and typical CMS cuts for this process: $p_{T1} > 20\,\mathrm{GeV}$, $p_{T2} > 10\,\mathrm{GeV}$, $p_{T3,4} > 5\,\mathrm{GeV}$, $M_{Z1}$, $M_{Z2} > 4\,\mathrm{GeV}$, $|\eta_e| < 2.5$, $|\eta_\mu| < 2.4$. Results are compared for the recommended NLO PDF set [9] to results for the PDF4LHC15 NNLO [2] set and CT14 LO set (included in the PDF4LHC combinations), all with the same recommended value of $\alpha_s = 0.118$, and the CT14 LLO set with $\alpha_s = 0.130$ in tables 8.2 and 8.3.

Table 8.3: PDF dependence of off-shell $gg\ (\to H) \to e^+e^-\mu^+\mu^-$ cross sections at LO in fb. CMS cuts are applied. Other details as in table 8.2.

| | | PDF set order | | | | | | |
|---|---|---|---|---|---|---|---|---|
| Region | Amp. | **NLO** | NNLO | $R$ | LO(0.118) | $R$ | LO(0.130) | $R$ |
| OFS | $S$ | 0.0952(3) | 0.09396(8) | 0.986(3) | 0.09034(7) | 0.949(3) | 0.10191(8) | 1.070(3) |
| | $S+I$ | −0.0893(3) | −0.0883(1) | 0.989(3) | −0.08436(9) | 0.944(3) | −0.0973(1) | 1.089(4) |
| | $B$ | 1.869(3) | 1.841(3) | 0.985(2) | 1.736(2) | 0.928(2) | 2.033(3) | 1.088(2) |
| HM1 | $S$ | 0.01303(9) | 0.01278(3) | 0.981(7) | 0.01200(3) | 0.921(7) | 0.01402(3) | 1.076(8) |
| | $S+I$ | −0.0298(2) | −0.02942(6) | 0.986(6) | −0.02759(5) | 0.925(5) | −0.03227(6) | 1.082(6) |
| | $B$ | 0.738(2) | 0.727(2) | 0.986(3) | 0.679(2) | 0.920(3) | 0.795(2) | 1.079(4) |
| HM2 | $S$ | 0.0761(3) | 0.07531(8) | 0.990(4) | 0.07271(7) | 0.956(3) | 0.08123(8) | 1.067(4) |
| | $S+I$ | −0.0349(2) | −0.03471(7) | 0.994(6) | −0.03376(6) | 0.967(6) | −0.03757(7) | 1.076(7) |
| | $B$ | 0.382(2) | 0.377(2) | 0.987(5) | 0.353(1) | 0.925(5) | 0.403(2) | 1.055(5) |
| RES | $S$ | 0.4392(7) | 0.4284(7) | 0.975(3) | 0.4343(7) | 0.989(3) | 0.5267(8) | 1.199(3) |
| | $S+I$ | 0.439(2) | 0.428(2) | 0.975(4) | 0.433(2) | 0.988(4) | 0.527(2) | 1.200(5) |
| | $B$ | 0.06294(8) | 0.06155(8) | 0.978(2) | 0.06243(9) | 0.992(2) | 0.0755(1) | 1.200(3) |
| OFS/ | $S$ | 0.2169(7) | 0.2193(4) | | 0.2080(4) | | 0.1935(4) | |
| RES | $S+I$ | −0.2036(8) | −0.2065(6) | | −0.1946(6) | | −0.1847(6) | |
| HM1/ | $S$ | 0.0297(2) | 0.02984(8) | | 0.02762(8) | | 0.02662(7) | |
| RES | $S+I$ | −0.0680(4) | −0.0688(3) | | −0.0637(3) | | −0.0613(2) | |
| HM2/ | $S$ | 0.1733(6) | 0.1758(4) | | 0.1674(4) | | 0.1542(3) | |
| RES | $S+I$ | −0.0796(5) | −0.0811(3) | | −0.0779(3) | | −0.0714(3) | |

The differences observed between different sets in tables 8.2 and 8.3 are in line with expectations - the largest variation from the recommended set is for the LO set with $\alpha_s = 0.130$, where the deviation can be up to 28% with minimal cuts. The NNLO and LO with $\alpha_s = 0.118$ sets generally show quite good agreement in all regions of the phase space and with both sets of cuts; some variation is expected and observed.

Tables 8.4 and 8.5 consider the variation of the recommended PDF set with different scale choices. With the recommended scale, variations of double and half the scale typically alter the signal by up to ±25%, dropping to approximately ±15% in the resonant region.

Table 8.4: QCD scale $\mu = \mu_R = \mu_F$ dependence and symmetric scale uncertainty of off-shell $gg\ (\to H) \to e^+e^-\mu^+\mu^-$ cross sections at LO in fb for one lepton-flavour combination. Minimal cuts are applied as described in the text. $R$ is the ratio of the result to the cross section with the recommended scale choice $\mu = M_{VV}/2$. As recommended, the NLO PDF set is used. Other details as in table 8.2.

| | | Dynamic scale | | | Fixed scales | | | |
|---|---|---|---|---|---|---|---|---|
| | | | $\Delta(M_{VV})$ | $R$ | | | | |
| Region | Amp. | $\boldsymbol{M_{VV}/2}$ | $\Delta(M_{VV}/4)$ | $R$ | $M_H/2$ | $R$ | $M_Z$ | $R$ |
| | | | symmetr. $\Delta$ | $R$ | | | | |
| OFS | $S$ | 0.1266(1) | −0.0258(2) | −0.204(2) | 0.2038(2) | 1.610(2) | 0.1760(2) | 1.390(2) |
| | $S$ | | 0.0349(2) | 0.276(2) | | | | |
| | $S$ | | 0.0303(2) | 0.240(1) | | | | |
| | $S+I$ | −0.1313(2) | 0.0251(2) | 0.182(2) | −0.1831(2) | 1.394(2) | −0.1604(2) | 1.221(2) |
| | $S+I$ | | −0.0328(2) | −0.250(2) | | | | |
| | $S+I$ | | ±0.0290(2) | ±0.221(1) | | | | |
| | $B$ | 2.988(4) | −0.545(5) | −0.182(2) | 3.751(4) | 1.255(3) | 3.327(4) | 1.114(2) |
| | $B$ | | 0.699(7) | 0.234(3) | | | | |
| | $B$ | | 0.6225(4) | 0.209(2) | | | | |
| HM1 | $S$ | 0.01928(3) | −0.00355(4) | −0.184(3) | 0.02406(6) | 1.248(4) | 0.02150(5) | 1.115(3) |
| | $S$ | | 0.00455(6) | 0.236(3) | | | | |
| | $S$ | | 0.00405(4) | 0.210(2) | | | | |
| | $S+I$ | −0.04553(8) | 0.0085(1) | 0.187(3) | −0.0561(1) | 1.233(3) | −0.05002(9) | 1.099(3) |
| | $S+I$ | | −0.0106(2) | −0.233(3) | | | | |
| | $S+I$ | | ±0.0096(1) | ±0.2095(2) | | | | |
| | $B$ | 1.186(3) | −0.223(4) | −0.188(3) | 1.462(3) | 1.232(4) | 1.302(3) | 1.098(4) |
| | $B$ | | 0.273(5) | 0.230(4) | | | | |
| | $B$ | | 0.248(2) | 0.209(3) | | | | |
| HM2 | $S$ | 0.0982(2) | −0.0207(2) | −0.211(2) | 0.1693(2) | 1.724(3) | 0.1451(2) | 1.478(3) |
| | $S$ | | 0.0284(2) | 0.289(2) | | | | |
| | $S$ | | 0.0246(2) | 0.250(2) | | | | |
| | $S+I$ | −0.04651(8) | 0.0099(2) | 0.212(3) | −0.0818(2) | 1.760(5) | −0.0700(2) | 1.505(4) |
| | $S+I$ | | −0.0136(2) | −0.293(3) | | | | |
| | $S+I$ | | ±0.0118(1) | ±0.253(2) | | | | |
| | $B$ | 0.610(1) | −0.123(2) | −0.201(3) | 0.929(3) | 1.524(5) | 0.807(2) | 1.323(4) |
| | $B$ | | 0.167(3) | 0.275(5) | | | | |
| | $B$ | | 0.145(2) | 0.238(3) | | | | |
| RES | $S$ | 0.800(1) | −0.115(2) | −0.143(2) | 0.801(2) | 1.001(2) | 0.737(1) | 0.921(2) |
| | $S$ | | 0.131(2) | 0.164(2) | | | | |
| | $S$ | | 0.123(2) | 0.154(2) | | | | |
| | $S+I$ | 0.803(2) | −0.116(3) | −0.145(2) | 0.803(2) | 1.000(3) | 0.739(2) | 0.920(3) |
| | $S+I$ | | 0.130(3) | 0.162(3) | | | | |
| | $S+I$ | | ±0.123(2) | ±0.153(2) | | | | |
| | $B$ | 0.1092(2) | −0.0158(3) | −0.145(3) | 0.1089(2) | 0.998(2) | 0.1002(2) | 0.917(2) |
| | $B$ | | 0.0176(3) | 0.162(3) | | | | |
| | $B$ | | 0.0167(2) | 0.153(2) | | | | |
| OFS/RES | $S$ | 0.1583(3) | | | 0.2545(5) | | 0.2389(4) | |
| | $S+I$ | −0.1635(4) | | | −0.2279(5) | | −0.2172(5) | |
| HM1/RES | $S$ | 0.02411(5) | | | 0.03005(8) | | 0.02918(8) | |
| | $S+I$ | −0.0567(2) | | | −0.0699(2) | | −0.0677(2) | |
| HM2/RES | $S$ | 0.1228(3) | | | 0.2114(4) | | 0.1970(4) | |
| | $S+I$ | −0.0579(2) | | | −0.1019(3) | | −0.0948(3) | |

Table 8.5: QCD scale $\mu = \mu_R = \mu_F$ dependence and symmetric scale uncertainty of off-shell $gg\ (\to H) \to \ell\bar{\ell}\ell'\bar{\ell}'$ cross sections at LO in fb for one lepton-flavour combination. CMS cuts are applied. Other details as in table 8.4.

| | | Dynamic scale | | | Fixed scales | | | |
|---|---|---|---|---|---|---|---|---|
| | | | $\Delta(M_{VV})$ | $R$ | | | | |
| Region | Amp. | $\boldsymbol{M_{VV}/2}$ | $\Delta(M_{VV}/4)$ | $R$ | $M_H/2$ | $R$ | $M_Z$ | $R$ |
| | | | symmetr. $\Delta$ | $R$ | | | | |
| OFS | $S$ | 0.0952(3) | −0.0196(3) | −0.206(4) | 0.1545(4) | 1.622(6) | 0.1338(4) | 1.405(5) |
| | $S$ | | 0.0257(4) | 0.270(4) | | | | |
| | $S$ | | ±0.0227(3) | ±0.238(3) | | | | |
| | $S+I$ | −0.0893(3) | 0.0164(4) | 0.184(4) | −0.1282(4) | 1.435(6) | −0.1119(3) | 1.253(5) |
| | $S+I$ | | −0.0223(4) | −0.250(5) | | | | |
| | $S+I$ | | ±0.0194(3) | ±0.217(3) | | | | |
| | $B$ | 1.869(3) | −0.331(4) | −0.177(2) | 2.341(3) | 1.252(3) | 2.084(3) | 1.115(2) |
| | $B$ | | 0.430(4) | 0.230(2) | | | | |
| | $B$ | | ±0.381(3) | ±0.204(2) | | | | |
| HM1 | $S$ | 0.01302(2) | −0.00235(3) | −0.181(2) | 0.0163(2) | 1.25(1) | 0.0145(1) | 1.115(8) |
| | $S$ | | 0.00303(3) | 0.233(3) | | | | |
| | $S$ | | ±0.00269(2) | ±0.207(2) | | | | |
| | $S+I$ | −0.02986(5) | 0.00536(6) | 0.179(2) | −0.0370(2) | 1.241(7) | −0.0326(2) | 1.092(6) |
| | $S+I$ | | −0.00682(7) | −0.228(3) | | | | |
| | $S+I$ | | ±0.00609(5) | ±0.204(2) | | | | |
| | $B$ | 0.739(1) | −0.132(2) | −0.178(2) | 0.908(2) | 1.229(3) | 0.811(2) | 1.097(3) |
| | $B$ | | 0.168(2) | 0.227(3) | | | | |
| | $B$ | | ±0.150(1) | ±0.203(2) | | | | |
| HM2 | $S$ | 0.0761(1) | −0.0160(2) | −0.210(2) | 0.1315(4) | 1.727(6) | 0.1131(4) | 1.485(5) |
| | $S$ | | 0.0218(2) | 0.286(3) | | | | |
| | $S$ | | ±0.0189(1) | ±0.248(2) | | | | |
| | $S+I$ | −0.03505(6) | 0.00740(7) | 0.211(2) | −0.0630(3) | 1.798(9) | −0.0537(3) | 1.533(8) |
| | $S+I$ | | −0.01006(9) | −0.287(3) | | | | |
| | $S+I$ | | ±0.0088(1) | ±0.249(2) | | | | |
| | $B$ | 0.3822(6) | −0.0768(8) | −0.201(2) | 0.582(2) | 1.522(5) | 0.506(2) | 1.324(4) |
| | $B$ | | 0.1019(9) | 0.267(3) | | | | |
| | $B$ | | ±0.090(1) | ±0.234(2) | | | | |
| RES | $S$ | 0.4392(7) | −0.0603(9) | −0.137(2) | 0.4389(7) | 0.999(3) | 0.4044(6) | 0.921(2) |
| | $S$ | | 0.066(1) | 0.151(3) | | | | |
| | $S$ | | ±0.064(2) | ±0.145(2) | | | | |
| | $S+I$ | 0.439(2) | −0.060(2) | −0.136(4) | 0.438(2) | 0.999(4) | 0.406(2) | 0.925(4) |
| | $S+I$ | | 0.067(2) | 0.154(5) | | | | |
| | $S+I$ | | ±0.064(2) | ±0.145(3) | | | | |
| | $B$ | 0.06294(8) | −0.0086(2) | −0.136(2) | 0.06302(9) | 1.001(2) | 0.05816(8) | 0.924(2) |
| | $B$ | | 0.0097(2) | 0.155(2) | | | | |
| | $B$ | | ±0.0092(1) | ±0.146(2) | | | | |
| OFS/ RES | $S$ | 0.2169(7) | | | 0.352(1) | | 0.331(1) | |
| | $S+I$ | −0.2036(8) | | | −0.292(2) | | −0.276(2) | |
| HM1/ RES | $S$ | 0.02964(6) | | | 0.0371(3) | | 0.0359(3) | |
| | $S+I$ | −0.0681(3) | | | −0.0845(5) | | −0.0804(5) | |
| HM2/ RES | $S$ | 0.1734(4) | | | 0.300(1) | | 0.280(1) | |
| | $S+I$ | −0.0799(3) | | | −0.1437(8) | | −0.1325(7) | |

# Chapter 9

# Conclusions

In this thesis, interference effects have been investigated for several classes of Higgs decays in gluon fusion at the LHC. Firstly, the semi-leptonic $H \to WW$ and $H \to ZZ$ channels provide important additional information in SM Higgs measurements and heavy Higgs searches, and it is important to investigate whether the tree-level background could induce significant interference effects with the loop-induced signal process. Secondly, the Higgs singlet model is the minimal SM Higgs-sector extension containing an additional Higgs-like particle, and is therefore an important benchmark model in heavy Higgs searches. Calculations have been presented for the interference in the fully leptonic decays in this model, namely the $\ell\bar{\ell}\ell'\bar{\ell}'$ and $\ell\bar{\nu}_\ell\bar{\ell}'\nu_{\ell'}$ final states. Finally, a summary has been given of the SM fully leptonic decays, alongside an investigation of the dependence of the cross section on PDF and renormalisation and factorisation scale choices.

With regard to the semi-leptonic processes, both the tree-level and quark-loop $gg$ background contributions to the interference have been computed. The former is enhanced at the amplitude level by $1/e^2$ relative to the latter. The results have been obtained using two independent implementations in the public codes gg2VV and MadGraph5_aMC@NLO, which show excellent agreement. Light and heavy Higgs masses have been considered with minimal and realistic experimental selection cuts. It was found that the interference of the Higgs signal with the tree-level background is suppressed compared to its interference with the loop-induced $VV$ background. This holds for light and heavy Higgs masses as well as minimal, LHC and Higgs search cuts. It can therefore be concluded that higher-order background contributions can induce leading interference effects. With appropriate background suppression cuts, the interference can be reduced to the 10% level for heavy SM Higgs masses, and to the per mille level for the light SM Higgs. Furthermore, it is seen that with the background cuts, the total effect of signal-background interference on the integrated cross section is negligibly small, but important differences are clearly visible in the differential distributions, particularly in the far off-shell region. The dominant interference contribution comes from the continuum background, particularly when selection cuts are implemented. In these off-shell regions interference effects dominate over the signal and therefore should be taken into account for more exclusive selection cuts or analysis methods.

In the Higgs singlet model, the interference of the heavy Higgs signal process with the light Higgs and continuum backgrounds was investigated. It was found that it is crucial to include both types of interference in phenomenological and experimental studies, as with minimal selection cuts both contributions induce relatively strong interference effects close to the heavy Higgs peak, but they are of similar size and opposite sign so that a strong cancellation occurs and the total effect on the cross section is small. Both contributions change sign as they pass through the heavy peak. Three values of heavy Higgs mass and two mixing angles were considered, and this conclusion was found to apply in all cases. It is found that interference effects increase significantly with increasing heavy Higgs mass, ranging from $\mathcal{O}(10\%)$ to $\mathcal{O}(1)$ effects for integrated cross sections. With a $|M_{VV} - M_{h2}| < \Gamma_{h2}$ window cut, it can be seen that overall interference effects are mitigated to $\mathcal{O}(10\%)$. Despite the occurring cancellation, the full interference is clearly non-negligible and modifies the heavy Higgs lineshape.

The final study expands on known results for the fully leptonic decays; in agreement with existing literature, interference effects are found to be of order 10% and have more importance in the off-peak regions. The total signal-background interference with minimal cuts is destructive in all cases. The dependence of the cross section on PDF and scale choice for this class of decays is found to be in line with theoretical expectations, for both minimal and typical experimental cuts. Scale dependence (comparing various fixed scales to the dynamical choice of $M_{VV}/2$) is smallest in the resonant region.

In conclusion, it is evident that interference effects merit careful treatment in precision studies of Higgs boson decays. Even in cases where selection cuts may render the total effect on the integrated cross section small or negligible, effects on the lineshape in differential distributions can be large, particularly in the off-shell region.

All calculations presented in this thesis have been carried out with a parton-level integrator and event generator, `gg2VV`. The modifications to the phase space portion of the code that were necessary for the results of Chapters 6 and 7 were described in detail in this thesis, and the relevant versions have been made publicly available.

# Bibliography

[1] C. Anastasiou, C. Duhr, F. Dulat, F. Herzog, and B. Mistlberger, "Higgs Boson Gluon-Fusion Production in QCD at Three Loops," *Phys. Rev. Lett.* 114, (2015) 212001, `arXiv:1503.06056 [hep-ph]`.

[2] J. Butterworth *et al.*, "PDF4LHC recommendations for LHC Run II," *J. Phys.* G43, (2016) 023001, `arXiv:1510.03865 [hep-ph]`.

[3] ATLAS Collaboration, "Constraints on the off-shell Higgs boson signal strength in the high-mass $ZZ$ and $WW$ final states with the ATLAS detector," *Eur. Phys. J.* C75, no. 7, (2015) 335, `arXiv:1503.01060 [hep-ex]`.

[4] CMS Collaboration, "Constraints on the Higgs boson width from off-shell production and decay to Z-boson pairs," *Phys. Lett.* B736, (2014) 64–85, `arXiv:1405.3455 [hep-ex]`.

[5] F. Caola and K. Melnikov, "Constraining the Higgs boson width with ZZ production at the LHC," *Phys. Rev.* D88, (2013) 054024, `arXiv:1307.4935 [hep-ph]`.

[6] N. Kauer and G. Passarino, "Inadequacy of zero-width approximation for a light Higgs boson signal," *JHEP* 08, (2012) 116, `arXiv:1206.4803 [hep-ph]`.

[7] N. Kauer and C. O'Brien, "Heavy Higgs signal–background interference in $gg \to VV$ in the Standard Model plus real singlet," *Eur. Phys. J.* C75, (2015) 374, `arXiv:1502.04113 [hep-ph]`.

[8] N. Kauer, C. O'Brien, and E. Vryonidou, "Interference effects for $H \to W\,W \to \ell\nu q\overline{q}'$ and $H \to ZZ \to \ell\bar{\ell}q\overline{q}$ searches in gluon fusion at the LHC," *JHEP* 10, (2015) 074, `arXiv:1506.01694 [hep-ph]`.

[9] LHC Higgs Cross Section Working Group Collaboration, "Handbook of LHC Higgs Cross Sections: 4. Deciphering the nature of the Higgs sector." In preparation, 2016.

[10] S. L. Glashow, "Partial Symmetries of Weak Interactions," *Nucl. Phys.* 22, (1961) .

[11] S. Weinberg, "A Model of Leptons," *Phys. Rev. Lett.* 19, (1967) 1264–1266.

[12] A. Salam, "Weak and electromagnetic interactions," in *Elementary Particle Physics: Relativistic Groups and Analyticity*, N. Svartholm, ed. Eighth Nobel Symposium, Lerum, May, 1968.

[13] P. W. Higgs, "Broken Symmetries and the Masses of Gauge Bosons," *Phys. Rev. Lett.* 13, (1964) 508–509.

[14] P. W. Higgs, "Broken symmetries, massless particles and gauge fields," *Phys. Lett.* 12, (1964) 132–133.

[15] P. W. Higgs, "Spontaneous Symmetry Breakdown without Massless Bosons," *Phys. Rev.* 145, (1966) 1156–1163.

[16] F. Englert and R. Brout, "Broken Symmetry and the Mass of Gauge Vector Mesons," *Phys. Rev. Lett.* 13, (1964) 321–323.

[17] G. S. Guralnik, C. R. Hagen, and T. W. B. Kibble, "Global Conservation Laws and Massless Particles," *Phys. Rev. Lett.* 13, (1964) 585–587.

[18] CMS Collaboration, "Observation of a new boson at a mass of 125 GeV with the CMS experiment at the LHC," *Phys. Lett.* B716, (2012) 30–61, `arXiv:1207.7235 [hep-ex]`.

[19] ATLAS Collaboration, "Observation of a new particle in the search for the Standard Model Higgs boson with the ATLAS detector at the LHC," *Phys. Lett.* B716, (2012) 1–29, `arXiv:1207.7214 [hep-ex]`.

[20] ATLAS Collaboration, "Measurement of the $t\bar{t}$ production cross-section using $e\mu$ events with $b$ -tagged jets in $pp$ collisions at $\sqrt{s} = 7$ and 8 TeV with the ATLAS detector," *Eur. Phys. J.* C74, no. 10, (2014) 3109, `arXiv:1406.5375 [hep-ex]`.

[21] CMS Collaboration, "Measurement of the $t\bar{t}$ production cross section in the dilepton channel in $pp$ collisions at $\sqrt{s} = 7$ TeV," *JHEP* 11, (2012) 067, `arXiv:1208.2671 [hep-ex]`.

[22] J. C. Collins, D. E. Soper, and G. F. Sterman, "Factorization of Hard Processes in QCD," *Adv. Ser. Direct. High Energy Phys.* 5, (1989) 1–91, `arXiv:hep-ph/0409313 [hep-ph]`.

[23] P. Z. Skands *et al.*, "SUSY Les Houches accord: Interfacing SUSY spectrum calculators, decay packages, and event generators," *JHEP* 07, (2004) 036, `arXiv:hep-ph/0311123 [hep-ph]`.

[24] R. K. Ellis, W. J. Stirling, and B. R. Webber, "QCD and Collider physics," *Camb. Monogr. Part. Phys. Nucl. Phys. Cosmol.* 8, (1996) 1–435.

[25] G. Altarelli and G. Parisi, "Asymptotic Freedom in Parton Language," *Nucl. Phys.* B126, (1977) 298.

[26] V. N. Gribov and L. N. Lipatov, "Deep inelastic e p scattering in perturbation theory," *Sov. J. Nucl. Phys.* 15, (1972) 438–450. [Yad. Fiz. 15, 781 (1972)].

[27] Y. L. Dokshitzer, "Calculation of the Structure Functions for Deep Inelastic Scattering and e+ e- Annihilation by Perturbation Theory in Quantum Chromodynamics.," *Sov. Phys. JETP* 46, (1977) 641–653. [Zh. Eksp. Teor. Fiz. 73, 1216 (1977)].

[28] A. Vogt, S. Moch, and J. A. M. Vermaseren, "The Three-loop splitting functions in QCD: The Singlet case," *Nucl. Phys.* B691, (2004) 129–181, `arXiv:hep-ph/0404111 [hep-ph]`.

[29] S. Moch, J. A. M. Vermaseren, and A. Vogt, "The Three loop splitting functions in QCD: The Nonsinglet case," *Nucl. Phys.* B688, (2004) 101–134, `arXiv:hep-ph/0403192 [hep-ph]`.

[30] M. Bahr *et al.*, "Herwig++ physics and manual," *Eur. Phys. J.* C58, (2008) 639–707, `arXiv:0803.0883 [hep-ph]`.

[31] L. Lonnblad, "ARIADNE version 4: A Program for simulation of QCD cascades implementing the color dipole model," *Comput. Phys. Commun.* 71, (1992) 15–31.

[32] T. Sjostrand, S. Mrenna, and P. Z. Skands, "PYTHIA 6.4 Physics and Manual," *JHEP* 05, (2006) 026, `arXiv:hep-ph/0603175 [hep-ph]`.

[33] T. Sjostrand, "High-energy physics event generation with PYTHIA 5.7 and JETSET 7.4," *Comput. Phys. Commun.* 82, (1994) 74–90.

[34] Tevatron Electroweak Working Group, CDF, DELPHI, SLD Electroweak and Heavy Flavour Groups, ALEPH, LEP Electroweak Working Group, SLD, OPAL, D0, L3 Collaboration, "Precision Electroweak Measurements and Constraints on the Standard Model," `arXiv:1012.2367 [hep-ex]`.

[35] CDF, D0 Collaboration, "Evidence for a particle produced in association with weak bosons and decaying to a bottom-antibottom quark pair in Higgs boson searches at the Tevatron," *Phys. Rev. Lett.* 109, (2012) 071804, `arXiv:1207.6436 [hep-ex]`.

[36] D0 Collaboration, "Search for the standard model Higgs boson in associated $WH$ production in 9.7 fb$^{-1}$ of $p\bar{p}$ collisions with the D0 detector," *Phys. Rev. Lett.* 109, (2012) 121804, `arXiv:1208.0653 [hep-ex]`.

[37] LHC Higgs Cross Section Working Group Collaboration, "Handbook of LHC Higgs Cross Sections: 1. Inclusive Observables," `arXiv:1101.0593 [hep-ph]`.

[38] D. de Florian and M. Grazzini, "Higgs production through gluon fusion: Updated cross sections at the Tevatron and the LHC," *Phys. Lett.* B674, (2009) 291–294, `arXiv:0901.2427 [hep-ph]`.

[39] C. Anastasiou, R. Boughezal, and F. Petriello, "Mixed QCD-electroweak corrections to Higgs boson production in gluon fusion," *JHEP* 04, (2009) 003, `arXiv:0811.3458 [hep-ph]`.

[40] M. L. Ciccolini, S. Dittmaier, and M. Kramer, "Electroweak radiative corrections to associated WH and ZH production at hadron colliders," *Phys. Rev.* D68, (2003) 073003, `arXiv:hep-ph/0306234 [hep-ph]`.

[41] L. Altenkamp, S. Dittmaier, R. V. Harlander, H. Rzehak, and T. J. E. Zirke, "Gluon-induced Higgs-strahlung at next-to-leading order QCD," *JHEP* 02, (2013) 078, `arXiv:1211.5015 [hep-ph]`.

[42] G. Ferrera, M. Grazzini, and F. Tramontano, "Associated ZH production at hadron colliders: the fully differential NNLO QCD calculation," *Phys. Lett.* B740, (2015) 51–55, `arXiv:1407.4747 [hep-ph]`.

[43] G. Ferrera, M. Grazzini, and F. Tramontano, "Associated WH production at hadron colliders: a fully exclusive QCD calculation at NNLO," *Phys. Rev. Lett.* 107, (2011) 152003, `arXiv:1107.1164 [hep-ph]`.

[44] O. Brein, A. Djouadi, and R. Harlander, "NNLO QCD corrections to the Higgs-strahlung processes at hadron colliders," *Phys. Lett.* B579, (2004) 149–156, `arXiv:hep-ph/0307206 [hep-ph]`.

[45] M. Ciccolini, A. Denner, and S. Dittmaier, "Electroweak and QCD corrections to Higgs production via vector-boson fusion at the LHC," *Phys. Rev.* D77, (2008) 013002, `arXiv:0710.4749 [hep-ph]`.

[46] P. Bolzoni, F. Maltoni, S.-O. Moch, and M. Zaro, "Higgs production via vector-boson fusion at NNLO in QCD," *Phys. Rev. Lett.* 105, (2010) 011801, `arXiv:1003.4451 [hep-ph]`.

[47] P. Bolzoni, F. Maltoni, S.-O. Moch, and M. Zaro, "Vector boson fusion at NNLO in QCD: SM Higgs and beyond," *Phys. Rev.* D85, (2012) 035002, `arXiv:1109.3717 [hep-ph]`.

[48] M. Cacciari, F. A. Dreyer, A. Karlberg, G. P. Salam, and G. Zanderighi, "Fully Differential Vector-Boson-Fusion Higgs Production at Next-to-Next-to-Leading Order," *Phys. Rev. Lett.* 115, no. 8, (2015) 082002, `arXiv:1506.02660 [hep-ph]`.

[49] L. Reina and S. Dawson, "Next-to-leading order results for t anti-t h production at the Tevatron," *Phys. Rev. Lett.* 87, (2001) 201804, `arXiv:hep-ph/0107101 [hep-ph]`.

[50] W. Beenakker, S. Dittmaier, M. Kramer, B. Plumper, M. Spira, and P. M. Zerwas, "NLO QCD corrections to t anti-t H production in hadron collisions," *Nucl. Phys.* B653, (2003) 151–203, `arXiv:hep-ph/0211352 [hep-ph]`.

[51] ATLAS Collaboration, "Measurements of the properties of the Higgs-like boson in the four lepton decay channel with the ATLAS detector using 25 $\text{fb}^{-1}$ of proton-proton collision data," ATLAS-CONF-2013-013, 2013.

[52] ATLAS Collaboration, "Measurement of the Higgs boson mass from the $H \to \gamma\gamma$ and $H \to ZZ^* \to 4\ell$ channels with the ATLAS detector using 25 $\text{fb}^{-1}$ of $pp$ collision data," *Phys. Rev.* D90, no. 5, (2014) 052004, `arXiv:1406.3827 [hep-ex]`.

[53] CMS Collaboration, "Precise determination of the mass of the Higgs boson and tests of compatibility of its couplings with the standard model predictions using proton collisions at 7 and 8 TeV," *Eur. Phys. J.* C75, no. 5, (2015) 212, `arXiv:1412.8662 [hep-ex]`.

[54] ATLAS, CMS Collaboration, "Combined Measurement of the Higgs Boson Mass in $pp$ Collisions at $\sqrt{s} = 7$ and 8 TeV with the ATLAS and CMS Experiments," *Phys. Rev. Lett.* 114, (2015) 191803, `arXiv:1503.07589 [hep-ex]`.

[55] R. Kleiss and R. Pittau, "Weight optimization in multichannel Monte Carlo," *Comput. Phys. Commun.* 83, (1994) 141–146, `arXiv:hep-ph/9405257 [hep-ph]`.

[56] C. Englert and M. Spannowsky, "Limitations and Opportunities of Off-Shell Coupling Measurements," *Phys. Rev.* D90, (2014) 053003, `arXiv:1405.0285 [hep-ph]`.

[57] L. J. Dixon and M. S. Siu, "Resonance continuum interference in the diphoton Higgs signal at the LHC," *Phys. Rev. Lett.* 90, (2003) 252001, `arXiv:hep-ph/0302233 [hep-ph]`.

[58] L. J. Dixon and Y. Li, "Bounding the Higgs Boson Width Through Interferometry," *Phys. Rev. Lett.* 111, (2013) 111802, `arXiv:1305.3854 [hep-ph]`.

[59] E. W. N. Glover and J. J. van der Bij, "Vector Boson Pair Production via Gluon Fusion," *Phys. Lett.* B219, (1989) 488.

[60] E. W. N. Glover and J. J. van der Bij, "Z Boson Pair Production Via Gluon Fusion," *Nucl. Phys.* B321, (1989) 561.

[61] G. Passarino, "Higgs Interference Effects in $gg \to ZZ$ and their Uncertainty," *JHEP* 08, (2012) 146, `arXiv:1206.3824 [hep-ph]`.

[62] J. M. Campbell, R. K. Ellis, E. Furlan, and R. Röntsch, "Interference effects for Higgs boson mediated $Z$-pair plus jet production," *Phys. Rev.* D90, no. 9, (2014) 093008, `arXiv:1409.1897 [hep-ph]`.

[63] J. M. Campbell, R. K. Ellis, and C. Williams, "Gluon-Gluon Contributions to W+ W- Production and Higgs Interference Effects," *JHEP* 10, (2011) 005, `arXiv:1107.5569 [hep-ph]`.

[64] M. Bonvini, F. Caola, S. Forte, K. Melnikov, and G. Ridolfi, "Signal-background interference effects for $gg \to H \to W^+W^-$ beyond leading order," *Phys. Rev.* D88, no. 3, (2013) 034032, `arXiv:1304.3053 [hep-ph]`.

[65] N. Kauer, "Signal-background interference in gg → H → VV," `arXiv:1201.1667 [hep-ph]`. [PoSRADCOR2011,027(2011)].

[66] S. P. Martin, "Shift in the LHC Higgs diphoton mass peak from interference with background," *Phys. Rev.* D86, (2012) 073016, `arXiv:1208.1533 [hep-ph]`.

[67] S. P. Martin, “Interference of Higgs diphoton signal and background in production with a jet at the LHC,” *Phys. Rev.* D88, no. 1, (2013) 013004, `arXiv:1303.3342 [hep-ph]`.

[68] D. de Florian, N. Fidanza, R. J. Hernández-Pinto, J. Mazzitelli, Y. Rotstein Habarnau, and G. F. R. Sborlini, “A complete $O(\alpha_S^2)$ calculation of the signal-background interference for the Higgs diphoton decay channel,” *Eur. Phys. J.* C73, no. 4, (2013) 2387, `arXiv:1303.1397 [hep-ph]`.

[69] E. Maina, “Interference effects in Heavy Higgs production via gluon fusion in the Singlet Extension of the Standard Model,” *JHEP* 06, (2015) 004, `arXiv:1501.02139 [hep-ph]`.

[70] A. Ballestrero and E. Maina, “Interference Effects in Higgs production through Vector Boson Fusion in the Standard Model and its Singlet Extension,” *JHEP* 01, (2016) 045, `arXiv:1506.02257 [hep-ph]`.

[71] J. R. Andersen and J. M. Smillie, “QCD and electroweak interference in Higgs production by gauge boson fusion,” *Phys. Rev.* D75, (2007) 037301, `arXiv:hep-ph/0611281 [hep-ph]`.

[72] A. Buckley, J. Ferrando, S. Lloyd, K. Nordström, B. Page, M. Rüfenacht, M. Schönherr, and G. Watt, “LHAPDF6: parton density access in the LHC precision era,” *Eur. Phys. J.* C75, (2015) 132, `arXiv:1412.7420 [hep-ph]`.

[73] T. Hahn, “Feynman Diagram Calculations with FeynArts, FormCalc, and LoopTools,” *PoS* ACAT2010, (2010) 078, `arXiv:1006.2231 [hep-ph]`.

[74] “omniORB-4.1.6.” `http://omniorb.sourceforge.net/`.

[75] F. Campanario, Q. Li, M. Rauch, and M. Spira, “ZZ+jet production via gluon fusion at the LHC,” *JHEP* 06, (2013) 069, `arXiv:1211.5429 [hep-ph]`.

[76] T. Hahn and M. Perez-Victoria, “Automatized one loop calculations in four-dimensions and D-dimensions,” *Comput. Phys. Commun.* 118, (1999) 153–165, `arXiv:hep-ph/9807565 [hep-ph]`.

[77] T. Gleisberg, S. Hoeche, F. Krauss, M. Schonherr, S. Schumann, F. Siegert, and J. Winter, "Event generation with SHERPA 1.1," *JHEP* 02, (2009) 007, `arXiv:0811.4622 [hep-ph]`.

[78] J. Alwall, R. Frederix, S. Frixione, V. Hirschi, F. Maltoni, O. Mattelaer, H. S. Shao, T. Stelzer, P. Torrielli, and M. Zaro, "The automated computation of tree-level and next-to-leading order differential cross sections, and their matching to parton shower simulations," *JHEP* 07, (2014) 079, `arXiv:1405.0301 [hep-ph]`.

[79] S. Uhlmann, R. Meinel, and A. Wipf, "Ward identities for invariant group integrals," *J. Phys.* A40, (2007) 4367–4390, `arXiv:hep-th/0611170 [hep-th]`.

[80] J. M. Campbell, R. K. Ellis, and C. Williams, "Vector boson pair production at the LHC," *JHEP* 07, (2011) 018, `arXiv:1105.0020 [hep-ph]`.

[81] ATLAS Collaboration, "Search for diboson resonances in the $\ell\bar{\ell}q\bar{q}$ final state in pp collisions at $\sqrt{s} = 13$ TeV with the ATLAS detector," ATLAS-CONF-2015-071, 2015.

[82] ATLAS Collaboration, "Search for $WW/WZ$ resonance production in the $\ell\nu qq$ final state at $\sqrt{s} = 13$ TeV with the ATLAS detector at the LHC," ATLAS-CONF-2015-075, 2015.

[83] ATLAS Collaboration, "Search for a standard model Higgs boson in the mass range 200-600 GeV in the $H \to ZZ \to \ell^+\ell^- q\bar{q}$ decay channel with the ATLAS detector," *Phys. Lett.* B717, (2012) 70–88, `arXiv:1206.2443 [hep-ex]`.

[84] ATLAS Collaboration, "Search for resonant ZZ production in the ZZ $\to \ell\bar{\ell}q\bar{q}$ channel with the ATLAS detector using 7.2 fb$^{-1}$ of $\sqrt{s} = 8$ TeV pp collision data," ATLAS-CONF-2012-150, 2012.

[85] CMS Collaboration, "Search for a Standard Model Like Higgs Boson in the H to ZZ to $\ell^+\ell^-$ $q\bar{q}$ Decay Channel at $\sqrt{s}$=8 TeV," CMS-PAS-HIG-14-007, 2015.

[86] CMS Collaboration, “Search for a Standard Model-like Higgs Boson Decaying into $WW \to \ell\nu q\bar{q}'$ in Exclusive Jet Bins in pp Collisions at $\sqrt{s} = 8$ TeV,” CMS-PAS-HIG-14-008, 2015.

[87] CMS Collaboration, “Search for a Standard Model-like Higgs boson decaying into WW to $\ell\nu\ q\bar{q}$ in pp collisions at $\sqrt{s} = 8$ TeV,” CMS-PAS-HIG-13-008, 2013.

[88] ATLAS Collaboration, “Search for the Higgs boson in the $H \to WW \to l\nu jj$ decay channel at $\sqrt{s} = 7$ TeV with the ATLAS detector,” *Phys. Lett.* B718, (2012) 391–410, `arXiv:1206.6074 [hep-ex]`.

[89] B. A. Dobrescu and J. D. Lykken, “Semileptonic decays of the standard Higgs boson,” *JHEP* 04, (2010) 083, `arXiv:0912.3543 [hep-ph]`.

[90] J. D. Lykken, A. O. Martin, and J.-C. Winter, “Semileptonic Decays of the Higgs Boson at the Tevatron,” *JHEP* 08, (2012) 062, `arXiv:1111.2881 [hep-ph]`.

[91] C. Hackstein and M. Spannowsky, “Boosting Higgs discovery: The Forgotten channel,” *Phys. Rev.* D82, (2010) 113012, `arXiv:1008.2202 [hep-ph]`.

[92] C. Kao and J. Sayre, “Confirming the LHC Higgs Discovery with WW,” *Phys. Lett.* B722, (2013) 324–329, `arXiv:1212.0929 [hep-ph]`.

[93] A. Menon and Z. Sullivan, “Higgs exclusion and the $H \to WW^* \to l\nu cj$ semi-leptonic channel at the Tevatron,” `arXiv:1109.6684 [hep-ph]`.

[94] A. D. Martin, W. J. Stirling, R. S. Thorne, and G. Watt, “Parton distributions for the LHC,” *Eur. Phys. J.* C63, (2009) 189–285, `arXiv:0901.0002 [hep-ph]`.

[95] S. Goria, G. Passarino, and D. Rosco, “The Higgs Boson Lineshape,” *Nucl. Phys.* B864, (2012) 530–579, `arXiv:1112.5517 [hep-ph]`.

[96] C. Englert, I. Low, and M. Spannowsky, “On-shell interference effects in Higgs boson final states,” *Phys. Rev.* D91, no. 7, (2015) 074029, `arXiv:1502.04678 [hep-ph]`.

[97] G. Passarino, “Theoretical uncertainty for the Higgs boson lineshape,” in *Proceedings, 11th DESY Workshop on Elementary Particle Physics: Loops and Legs in Quantum Field Theory*, vol. LL2012, p. 010. 2012.

[98] V. Barger, P. Langacker, M. McCaskey, M. Ramsey-Musolf, and G. Shaughnessy, “Complex Singlet Extension of the Standard Model,” *Phys. Rev.* D79, (2009) 015018, `arXiv:0811.0393 [hep-ph]`.

[99] V. Barger, P. Langacker, M. McCaskey, M. J. Ramsey-Musolf, and G. Shaughnessy, “LHC Phenomenology of an Extended Standard Model with a Real Scalar Singlet,” *Phys. Rev.* D77, (2008) 035005, `arXiv:0706.4311 [hep-ph]`.

[100] B. Batell, D. McKeen, and M. Pospelov, “Singlet Neighbors of the Higgs Boson,” *JHEP* 10, (2012) 104, `arXiv:1207.6252 [hep-ph]`.

[101] B. Batell, S. Gori, and L.-T. Wang, “Exploring the Higgs Portal with 10/fb at the LHC,” *JHEP* 06, (2012) 172, `arXiv:1112.5180 [hep-ph]`.

[102] G. Bhattacharyya, G. C. Branco, and S. Nandi, “Universal Doublet-Singlet Higgs Couplings and phenomenology at the CERN Large Hadron Collider,” *Phys. Rev.* D77, (2008) 117701, `arXiv:0712.2693 [hep-ph]`.

[103] T. Binoth and J. J. van der Bij, “Influence of strongly coupled, hidden scalars on Higgs signals,” *Z. Phys.* C75, (1997) 17–25, `arXiv:hep-ph/9608245 [hep-ph]`.

[104] S. Bock, R. Lafaye, T. Plehn, M. Rauch, D. Zerwas, and P. M. Zerwas, “Measuring Hidden Higgs and Strongly-Interacting Higgs Scenarios,” *Phys. Lett.* B694, (2011) 44–53, `arXiv:1007.2645 [hep-ph]`.

[105] M. Bowen, Y. Cui, and J. D. Wells, “Narrow trans-TeV Higgs bosons and H → hh decays: Two LHC search paths for a hidden sector Higgs boson,” *JHEP* 03, (2007) 036, `arXiv:hep-ph/0701035 [hep-ph]`.

[106] S. Dawson and W. Yan, “Hiding the Higgs Boson with Multiple Scalars,” *Phys. Rev.* D79, (2009) 095002, `arXiv:0904.2005 [hep-ph]`.

[107] M. J. Dolan, C. Englert, and M. Spannowsky, "New Physics in LHC Higgs boson pair production," *Phys. Rev.* D87, no. 5, (2013) 055002, `arXiv:1210.8166 [hep-ph]`.

[108] C. Englert, T. Plehn, M. Rauch, D. Zerwas, and P. M. Zerwas, "LHC: Standard Higgs and Hidden Higgs," *Phys. Lett.* B707, (2012) 512–516, `arXiv:1112.3007 [hep-ph]`.

[109] C. Englert, T. Plehn, D. Zerwas, and P. M. Zerwas, "Exploring the Higgs portal," *Phys. Lett.* B703, (2011) 298–305, `arXiv:1106.3097 [hep-ph]`.

[110] C. Englert, J. Jaeckel, E. Re, and M. Spannowsky, "Evasive Higgs Maneuvers at the LHC," *Phys. Rev.* D85, (2012) 035008, `arXiv:1111.1719 [hep-ph]`.

[111] P. J. Fox, D. Tucker-Smith, and N. Weiner, "Higgs friends and counterfeits at hadron colliders," *JHEP* 06, (2011) 127, `arXiv:1104.5450 [hep-ph]`.

[112] R. S. Gupta and J. D. Wells, "Higgs boson search significance deformations due to mixed-in scalars," *Phys. Lett.* B710, (2012) 154–158, `arXiv:1110.0824 [hep-ph]`.

[113] H. E. Logan, "Hiding a Higgs width enhancement from off-shell $gg(\to h^*) \to ZZ$ measurements," *Phys. Rev.* D92, no. 7, (2015) 075038, `arXiv:1412.7577 [hep-ph]`.

[114] J. M. No and M. Ramsey-Musolf, "Probing the Higgs Portal at the LHC Through Resonant di-Higgs Production," *Phys. Rev.* D89, no. 9, (2014) 095031, `arXiv:1310.6035 [hep-ph]`.

[115] B. Patt and F. Wilczek, "Higgs-field portal into hidden sectors," `arXiv:hep-ph/0605188 [hep-ph]`.

[116] S. Profumo, M. J. Ramsey-Musolf, C. L. Wainwright, and P. Winslow, "Singlet-catalyzed electroweak phase transitions and precision Higgs boson studies," *Phys. Rev.* D91, no. 3, (2015) 035018, `arXiv:1407.5342 [hep-ph]`.

[117] R. Schabinger and J. D. Wells, "A Minimal spontaneously broken hidden sector and its impact on Higgs boson physics at the large hadron collider," *Phys. Rev.* D72, (2005) 093007, `arXiv:hep-ph/0509209 [hep-ph]`.

[118] S. Dawson and I. M. Lewis, "NLO corrections to double Higgs boson production in the Higgs singlet model," *Phys. Rev.* D92, no. 9, (2015) 094023, `arXiv:1508.05397 [hep-ph]`.

[119] F. Bojarski, G. Chalons, D. Lopez-Val, and T. Robens, "Heavy to light Higgs boson decays at NLO in the Singlet Extension of the Standard Model," `arXiv:1511.08120 [hep-ph]`.

[120] K. Cheung, P. Ko, J. S. Lee, J. Park, and P.-Y. Tseng, "A Higgcision study on the 750 GeV Di-photon Resonance and 125 GeV SM Higgs boson with the Higgs-Singlet Mixing," `arXiv:1512.07853 [hep-ph]`.

[121] T. Robens and T. Stefaniak, "LHC Benchmark Scenarios for the Real Higgs Singlet Extension of the Standard Model," `arXiv:1601.07880 [hep-ph]`.

[122] C.-Y. Chen, S. Dawson, and I. M. Lewis, "Exploring resonant di-Higgs boson production in the Higgs singlet model," *Phys. Rev.* D91, no. 3, (2015) 035015, `arXiv:1410.5488 [hep-ph]`.

[123] LHC Higgs Cross Section Working Group Collaboration, "Handbook of LHC Higgs Cross Sections: 3. Higgs Properties," `arXiv:1307.1347 [hep-ph]`.

[124] J. R. Espinosa, T. Konstandin, and F. Riva, "Strong Electroweak Phase Transitions in the Standard Model with a Singlet," *Nucl. Phys.* B854, (2012) 592–630, `arXiv:1107.5441 [hep-ph]`.

[125] S. Ghosh, A. Kundu, and S. Ray, "On the potential of a singlet scalar enhanced Standard Model," `arXiv:1512.05786 [hep-ph]`.

[126] A. Alloul, N. D. Christensen, C. Degrande, C. Duhr, and B. Fuks, "FeynRules 2.0 - A complete toolbox for tree-level phenomenology," *Comput. Phys. Commun.* 185, (2014) 2250–2300, `arXiv:1310.1921 [hep-ph]`.

[127] ATLAS Collaboration, "Search for resonances decaying to photon pairs in 3.2 $\mathrm{fb}^{-1}$ of $pp$ collisions at $\sqrt{s} = 13$ TeV with the ATLAS detector," ATLAS-CONF-2015-081, 2015.

[128] ATLAS Collaboration, "Constraints on New Phenomena via Higgs Coupling Measurements with the ATLAS Detector," ATLAS-CONF-2014-010, 2014.

[129] ATLAS Collaboration, "A search for resonant Higgs-pair production in the $b\bar{b}b\bar{b}$ final state in $pp$ collisions at $\sqrt{s} = 8$ TeV," ATLAS-CONF-2014-005, 2014.

[130] ATLAS Collaboration, "Search for an additional, heavy Higgs boson in the $H \to ZZ$ decay channel at $\sqrt{s} = 8\;$ TeV in $pp$ collision data with the ATLAS detector," *Eur. Phys. J.* C76, no. 1, (2016) 45, `arXiv:1507.05930 [hep-ex]`.

[131] ATLAS Collaboration, "Constraints on new phenomena via Higgs boson couplings and invisible decays with the ATLAS detector," *JHEP* 11, (2015) 206, `arXiv:1509.00672 [hep-ex]`.

[132] ATLAS Collaboration, "Searches for Higgs boson pair production in the $hh \to bb\tau\tau, \gamma\gamma WW^*, \gamma\gamma bb, bbbb$ channels with the ATLAS detector," *Phys. Rev.* D92, (2015) 092004, `arXiv:1509.04670 [hep-ex]`.

[133] ATLAS Collaboration, "Search for Scalar Diphoton Resonances in the Mass Range $65 - 600$ GeV with the ATLAS Detector in $pp$ Collision Data at $\sqrt{s} = 8\ TeV$," *Phys. Rev. Lett.* 113, no. 17, (2014) 171801, `arXiv:1407.6583 [hep-ex]`.

[134] CMS Collaboration, "Search for a Higgs Boson in the Mass Range from 145 to 1000 GeV Decaying to a Pair of W or Z Bosons," *JHEP* 10, (2015) 144, `arXiv:1504.00936 [hep-ex]`.

[135] CMS Collaboration, "Search for new physics in high mass diphoton events in proton-proton collisions at 13 TeV," CMS-PAS-EXO-15-004, 2015.

[136] CMS Collaboration, "Combination of standard model Higgs boson searches and measurements of the properties of the new boson with a mass near 125 GeV," CMS-PAS-HIG-12-045, 2012.

[137] V. Ravindran, J. Smith, and W. L. Van Neerven, "Next-to-leading order QCD corrections to differential distributions of Higgs boson production in hadron hadron collisions," *Nucl. Phys.* B634, (2002) 247–290, `arXiv:hep-ph/0201114 [hep-ph]`.

[138] G. Passarino , unpublished.

[139] N. Kauer, "Interference effects for H → WW/ZZ → $\ell\bar{\nu}_\ell\bar{\ell}\nu_\ell$ searches in gluon fusion at the LHC," *JHEP* 12, (2013) 082, `arXiv:1310.7011 [hep-ph]`.

[140] ATLAS Collaboration, "Measurements of the Total and Differential Higgs Boson Production Cross Sections Combining the H→ $\gamma\gamma$ and $H \to ZZ^* \to 4\ell$ Decay Channels at $\sqrt{s} = 8\,\text{TeV}$ with the ATLAS Detector," *Phys. Rev. Lett.* 115, no. 9, (2015) 091801, `arXiv:1504.05833 [hep-ex]`.

[141] ATLAS Collaboration, "Measurement of fiducial differential cross sections of gluon-fusion production of Higgs bosons decaying to $W^+W^- \to e\nu\mu\nu$ with the ATLAS detector at $\sqrt{s} = 8$ TeV," `arXiv:1604.02997 [hep-ex]`.

[142] CMS Collaboration, "Measurement of differential and integrated fiducial cross sections for Higgs boson production in the four-lepton decay channel in pp collisions at $\sqrt{s} = 7$ and $8\,\text{TeV}$," *JHEP* 04, (2016) 005, `arXiv:1512.08377 [hep-ex]`.

[143] CMS Collaboration, "Measurement of Higgs boson production and properties in the WW decay channel with leptonic final states," *JHEP* 01, (2014) 096, `arXiv:1312.1129 [hep-ex]`.